IMAGING BIOMARKERS OF TISSUE HYPOXIA IN GLIOBLASTOMA

A thesis submitted to The University of Manchester for the degree of

Doctor of Medicine

in the Faculty of Biology, Medicine and Health

2019

Dr Natale Quartuccio

School of Health Sciences

Division of Informatics, Imaging & Data Sciences

List of Contents

Total word count = 37185

List of Figures

List of Tables

List of Abbreviations

([^{11}C]-(R)-PK11195	(11)C](R)-(1-[2-chlorophenyl]-N-methyl-N-[1-methylpropyl]-3-isoquinoline carboxamide)
[^{15}O]H_2O	^{15}O-labelled water
[^{18}F]FAZA	[18F]Fluoroazomycinarabinofuranoside
[^{18}F]FDG	[18F]Fluorodeoxyglucose
[^{18}F]FMISO	[18F]Fluoromisonidazole
[^{18}F]HX4	18F]-3-Fluoro-2-(4-((2-nitro-1H-imidazol-1-yl)methyl)-1H-1,2,3-triazol-1-yl)propan-1-ol
[^{60,61,62,64}CU]ATSM	[60,61,62,64Cu]-labelled methylthiosemicarbazone
a^{-1}	Capillary heterogeneity
ADC	Apparent diffusion coefficient
ADM	Adrenomedullin
ALDA	Aldolase
ALDC	Aldolase-C
AOD	Anaplastic oligodendroglioma
ARCON	Accelerated radiotherapy with carbogen and nicotinamide (ARCON)
ARSAC	Administration of Radioactive Substances Advisory Committee
ATP	Adenosine triphosphate
AUC	Area under the curve
BBB	Blood-brain barrier
BCNU	Carmustine
BOLD-MRI	Blood oxygen level-dependent MRI
CAIX	Carbonic anhydrase IX
CATHD	Cathepsin
CBV	Cerebral blood volume
CCNU	Lomustine
CD	Cluster of differentiation
CE	Contrast-enhanced
cgGBM	Giant cell glioblastoma
CNS	Central Nervous System
CO	Carbon monoxide
CO_2	Carbon dioxide
CoD	Coefficient of determination
CRUK	Cancer Research UK
CSF	Cerebrospinal fluid
DCE-MRI	Dynamic contrast-enhanced MRI
DEG	Degree
DNA	Deoxyribonucleic acid
DO_2	Oxygen delivery
DSC	Dynamic susceptibility contrast
DWI	Diffusion-weighted imaging
EANO	European Association of Neuro-Oncology

ECG	Electrocardiogram
EF5	2-(2-nitro-1H-imidazol-1-yl)-N-(2,2,3,3,3-penta-luoropropyl)-acetamide
EGFR	Epidermal growth factor receptor
EG-VEGF	Endocrine gland-derived
EN	Enhancing region
ENF	Enhancing fraction
ENG	Endoglin
ENO1	Enolase 1
EPO	Erythropoietin
EPR	Electron Paramagnetic Resonance
FFE	Fast Field Echo
FHV	Fractional hypoxic volume
Fig.	Figure
FIH-1	Factor inhibiting HIF-1
FiO_2	Fraction of inspired oxygen
FLAIR	Fluid Attenuated Inversion Recovery
FN1	Fibronectin 1
FOV	Field of view
GABRA 1	Gamma-aminobutyric acid (GABA) A receptor alpha 1
GAPDH	Glyceraldehyde-3-P-dehydrogenase
GBM	Glioblastoma
GBq	Gigabecquerel
G-CIMP	Glioma-CpG island methylator phenotype
Gd	Gadolinium
Gd-DTPA	Gd-diethylenetriaminepentaacetic acid
GLUT	Glucose Transporter
GLUT1	Glucose transporter 1
GLUT3	Glucose transporter 3
GM	Grey matter
GMP	Good Manufacture Practice
GSC	Glioma stem cell
GSM	Gliosarcoma
Gy	Gray
h	Hour
H2O	Water
Hb	Haemoglobin
HIF1- α	Hypoxia-inducible factor 1α
HK1	Hexokinase 1
HK2	Hexokinase 2
HNSCC	Head and neck squamous-cell carcinoma
HREs	HIF-response elements
HV	Hypoxic volume
IAUC	Integrated area under the curve
IAUCGd	Initial area under the contrast agent concentration
ICA	Internal carotid artery
IDH	Isocitrate dehydrogenase

IGF2	Insulin-like growth-factor 2
IGF-BP1-3	IGF-factor-binding-proteins
IHC	Immunohistochemistry
IR	Inversion recovery
kep	Washout rate
K^{trans}	Transfer constant
l	Litre
LDHA	Lactate dehydrogenase A
LEP	Leptine
LRP1	LDL-receptor-related protein 1
max	Maximum
mCRPC	Metastatic castration resistant prostate cancer
MDR1	Multidrug resistance 1
MDT	Multidisciplinary team
med	Median
MGMT	O(6)-methylguanine-DNA-methyltransferase
min	Minimum
min	Minute
miRNA	MicroRNA
mm	Millimetre
mmHg	Millimetre of mercury
MMP2	Matrix metalloproteinase 2
MR	Magnetic resonance
MRI	Magnetic resonance imaging
ms	Millisecond
MVCP	Microvascular cellular proliferation
MVD	Microvascular density
MRS	Magnetic resonance spectroscopy
n.	Number
NE	Non-enhancing
NEFL	Neurofilament, Light Polypeptide
NF1	Neurofibromin 1
NHS	National Health Service
NICE	National Institute for Health and Care Excellence
NIHR	National Institute for Health Research
NOS2	nitric oxide synthase 2
NSF	Nephrogenic systemic fibrosis
O_2	Oxygen
OE-MRI	Oxygen-enhanced MRI
OER	Oxygen enhancement ratio
OPN	Osteopontin
OS	Overall survival
p.i.	Post injection
p53	Tumor protein 53
Pt.	Patient
PAI1	Plasminogen-activator inhibitor 1

PaO_2	Partial Pressure of Oxygen in Arterial Blood
PCA	Phase contrast angiography
PDK1	Pyruvate dehydrogenase kinase 1
PET	Positron emission tomography
PFKBF3	6-phosphofructo-2-kinase/fructose-2,6-biphosphatase-3
PFKL	Phosphofructokinase L
PFS	Progression-free survival
PGK 1	Phosphoglycerate kinase 1
PHD	Prolyl hydroxylase-domain
PKM	Pyruvate kinase M
PO_2	Partial pressure of oxygen
PS	Permeability surface area
PSIC	Percentage of signal intensity change
pVHL	Von Hippel-Lindau protein
QF	Quantitative flow
R&D	Research and development
R1	Longitudinal relaxation rate
R2	Transverse relaxation rate
rCBF	Regional cerebral flow
rCBV	Relative CBV
REC	Research Ethics Committee
RNA	Ribonucleic acid
ROC	Receiver operating curve
ROI	Region of interest
RT	Radiotherapy
sec	Second
SENSE	Sensitivity encoding
SLC12A5	Solute Carrier Family 12 Member 5
SOP	Standard operating procedure
SPECT	Single photon emission computed tomography
SRFT	Salford Royal NHS Foundation Trust
SUV	Standardized uptake value
SYT1	Synaptotagmin I
T/B	Tumor-to-blood
T/Bmax	Maximum tumor-to-blood activity ratio
T1	Longitudinal relaxation time
t1/2	Half-life
T1-w	T1-weighted
T2	Transverse relaxation time
TBR	Tumor-to-background ratio
tc	Capillary transit time
TE	Echo time
TGF-α	Transforming growth factor α
TGF-β	Transforming growth factor β
TI	Inversion time
TMZ	Temozolomide

TNF-α	Tumor necrosis factor alpha
TPI	Triosephosphate isomerase
TR	Repetition time
TTP	Time to progression
UPAR	Urokinase plasminogen activator receptor
Vb	Blood volume
v_e.	Extravascular extracellular volume fraction
VEGF	Vascular endothelial growth factor
VEGFR	Vascular endothelial growth factor receptor
VFA	Variable flip angle
VOI	Volume of interest
Vol.	Volunteer
v_p	Vascular plasma volume
vs.	Versus
WHO	World Health Organization
WM	White matter
WMIC	Wolfson Molecular Imaging Centre

Thesis Abstract

High-grade gliomas are relatively rare and highly aggressive tumors affecting the brain. Despite significant research efforts in the last decades, survival for patients with high-grade gliomas is still poor. A number of research outputs have underlined the role of the hypoxic microenvironment on the aggressiveness and resistance to conventional therapies. Several hypoxia-modifying treatments are now available. However, there is an unmet need to bring a non-invasive imaging technique to the clinical setting in order to quantify tumor hypoxia and stratify patients with brain tumors based on hypoxia imaging findings. Oxygen-enhanced Magnetic Resonance Imaging (OE-MRI) appears as an intriguing and promising method to measure tissue hypoxia.

The main goal of the two first experimental chapters of this thesis was to investigate the measurability and reproducibility of the percentage change of the longitudinal relaxation rate (R1), a commonly used parameter in OE-MRI studies to quantify tissue oxygenation, in normal brain and brain tumors.

In a further study, employing Dynamic contrast-enhanced MRI, we explored the possibility of characterizing different tumor habitat types in patients with high-grade glioma and predict overall survival (OS) by means of the analysis of the histogram of the extravascular extracellular volume fraction (v_e).

Declaration

No portion of the work referred to in the thesis has been submitted in support of an application for another degree or qualification of this or any other university or other institute of learning.

Copyright Statement

Acknowledgements and dedication

I am sincerely grateful to my supervisors for the high scientific support and helpful discussions during the entire course of my studies (Alan, Marie-claude, David and Neil). I would like also to express gratitude to Cancer Research UK (CRUK) for having sponsored my research at a well-recognized institution as the Wolfson Molecular Imaging Centre (WMIC).

I would like also to thank the whole WMIC environment, including colleagues, study participants and administrative and technical staff, for their continuous assistance and clinicians at Salford NHS Foundation Trust (SRFT) for helping with the recruitment of patients who spent a significant amount of time at our institution to undergo the imaging research protocols presented in this thesis.

I finally wish to dedicate this thesis to my parents, my sister, my wife and my son.

About the Author

I received my Bachelor Degree in Medicine in 2009 from the University of Palermo and then a Specialty Certificate in Nuclear Medicine in 2015 from the University of Messina.

Before arriving to the WMIC in 2014 as a Clinical Research Fellow, I shared my time between clinical duties in Sicily and clinical research periods in different Nuclear Medicine Departments in Italy (Turin) and abroad (New York, USA). My research mainly focused on retrospective studies involving the clinical application of scintigraphy studies and [^{18}F]FDG PET scans in different oncological and non-oncological conditions.

I really wanted to move to the WMIC to improve my research skills. Here, I had the opportunity to focus on brain tumors, learn to write research protocols and improve my knowledge on different MRI techniques including Oxygen-enhanced MRI, Dynamic contrast-enhanced MRI, 2D phase contrast angiography and quantitative flow (QF) measurements.

Furthermore, I was also coinvestigator in other research studies using non-conventional PET tracers in patients for the evaluation of hypoxia ([^{18}F]FAZA), flow ([^{15}O]H_2O) in high-grade gliomas and neuroinflammation ([^{11}C]-(R)-PK11195) in brain metastases.

Over the course of the last 4 years, I acquired experience with software for statistical purposes, image analysis and got basic experience with programming.

I contributed to the recruitment of patients, acquisition, analysis and statistical analysis of the imaging studies included in this thesis. In the same time, I improved my clinical skills participating to reporting sessions at the Nuclear Medicine Department of the Central Manchester University Hospital as Honorary Clinical Fellow.

I moved back to my hometown, Palermo, in June 2017, after 10 years spent in different institutions. Now, I hope to have in future the chance to translate my research skills to the clinical setting.

Chapter 1 The Journal Format Thesis

1.1 Preface

The objective of my research is providing validation of a relatively novel imaging technique, Oxygen-enhanced Magnetic Resonance Imaging (OE-MRI), in the quantification of tumor hypoxia in patients with brain tumors, specifically high-grade gliomas. In my thesis I will discuss also MRI techniques and Positron Emission Tomography (PET) imaging in the evaluation of the tumor hypoxic environment.

1.2 Organization and Structure of the Thesis

Chapter 2 Context and Rationale

Chapter 2 will provide an overview of brain tumors, with a focus on high-grade gliomas, tumors arising from the glia, the supporting tissue of the Central Nervous System (CNS). The chapter begins with the presentation of epidemiological information, classification and essential histological information of gliomas. In this section a summary of the available treatments for high-grade gliomas will also be discussed. Then, the biology of hypoxia, a phenomenon characterized by inadequate oxygen concentration to allow the normal execution of biological functions, will be analysed. Hypoxic tumors are commonly known to demonstrate resistance to common treatments. Patients with hypoxic tumors have usually a worse outcome compared to patients with non-hypoxic tumors. In the last decades, new treatments targeting tumor hypoxia have emerged and imaging techniques to evaluate hypoxia are now experiencing a renewed interest by the scientific community. Reliable measurement of tumor hypoxia by means of non-invasive imaging techniques, as PET or MRI, may help defining subclasses of patients who may benefit from the administration of

hypoxia-modifying treatments. In the last section of the 2nd chapter an outline of PET and MRI techniques currently available in this settings will be presented to the readers.

Chapter 3 Effects of High FiO2 Levels on Cerebral Blood Flow and Brain and CSF Signal

Administration of gas mixtures containing high fraction of inspired oxygen (FiO_2), as previously documented in literature, produces predictable positive and fast small signal changes in the cerebrospinal fluid (CSF). Data on measurement of change of the longitudinal relaxation rate (R1) in normal brain of healthy subjects exposed to supraphysiological FiO_2 is still scarce. The relationship between changes of R1 and cerebral blood flow (CBF) under the administration of different FiO_2 also needs to be fully elucidated. Furthermore, clinically translatable image-based approaches for the identification of successful oxygen administration and, consequently, confident quantification of signal change in response to O_2 administration have not yet been described.

The main aim of this study is to document the magnitude, timing and distribution of signal changes in grey, white matter and CSF in a cohort of thirteen normal healthy volunteers undergoing OE-MRI in association with different levels of FiO_2. Secondly, we aimed at identifying optimal analytical approaches for the identification of oxygen induced signal change, evaluating the repeatability of the measurements and developing a simple clinically translatable method for the evaluation of satisfactory oxygen delivery in subjects undergoing OE-MRI.

Chapter 4 Time Course and Reproducibility of R1 in Brain and Tumor Regions of Patients with High-grade Gliomas

The main objective of this experimental chapter is the evaluation of R1 change in normal brain parenchyma and tumor lesions of patients with high-grade glioma in response to a FiO_2 of 100%. In addition, we investigated the reproducibility of the OE-

MRI signal. In this study 12 patients with high-grade gliomas underwent an MRI protocol including OE-MRI twice in the same day.

Chapter 5 Histogram Analysis of Extravascular Extracellular Space Data from DCE-MRI in Glioblastoma Provides a Potential Imaging Biomarker of Micro-necrosis, Related to Survival

Glioblastoma, the most aggressive form of gliomas, is commonly associated with poor prognosis. A number of biomarkers derived from Dynamic contrast-enhanced MRI (DCE-MRI) proved to hold prognostic power. Previous authors demonstrated improved predictive power for DCE-MRI parameters when centile values and the shape of the distribution curve were considered for individual biomarkers. This study was designed to test the hypothesis that histogram analysis of DCE-MRI derived parameters provides additional predictive power for overall survival compared to estimation of median or mean values.

Chapter 2 Context and Rationale

2.1 High-grade gliomas

Epidemiology, classification and histological features

Gliomas are brain tumors that derive from cells of the glial tissue (astrocytes, oligodendrocytes and ependymal cells), which plays a supportive role in the central nervous system (CNS) [1]. Glial cell tumors account for 28% of all primary brain tumors and 80% of the malignant ones [1, 2]. Overall, incidence is approximately 5 per 100,000 persons per year, with an age peak after 60 years (11.9 per 100,000 persons) and the lowest incidence rate in the age range 0-19 years (1.8 per 100,000 people) [2].

The World Health Organization (WHO) classifies gliomas in four grades according to their microscopic features. High-grade gliomas are the most aggressive ones and include anaplastic astrocytoma (grade III) and grade IV glioma, formerly known as glioblastoma multiforme [3]. Glioblastoma (GBM), the highest-grade (IV) form of glioma, represents the most common (incidence: 4.64/100000/year) and aggressive primary malignant brain tumor [4]. Recent progresses in treatment strategies have led to a comparable outcome to other incurable malignancies [5]. However, prognosis still remains dramatically poor, with an overall survival (OS) of 14.6 months for patients receiving maximal treatment [6].

GBMs can be distinguished into primary GBMs, which arise “de novo”, and secondary GBMs, which originate from lower grade gliomas [4, 7]. Although secondary GBMs have less areas of necrosis, they cannot be easily distinguished from primary GBMs based on histology, but carry different genetic mutations [8, 9]. Mutations in isocitrate dehydrogenase-1 (IDH1) and IDH2 are common in low-grade glioma and secondary

GBM and rare in primary GBM (5-10%) [10-12]. Furthermore, secondary GBMs demonstrate a higher frequency of O(6)-methylguanine-DNA methyltransferase (MGMT) methylation than primary GBMs [13]. IDH1/2mutations and MGMT methylation have been demonstrated to be powerful indicators of favourable outcome in patients with glioma [14].

Beyond the classical type of primary GBM, WHO distinguish three main histological variants: epithelioid glioblastoma, gliosarcoma (GSM) and giant cell glioblastoma (cgGBM) [3, 15]. Epithelioid glioblastomas are composed of large epithelioid cells and occur mainly in young patients [3]. GSM is a very rare variant (1-5% of all GBMs), composed of a mixed pattern of glial cells and sarcomatous/mesenchymal cells; this variant shows poor outcome with an average OS of 4-11.5 months [16]. Giant cell glioblastoma presents a preponderance of multinucleated giant cells and is associated with a more favourable outcome than GBM in general [17]. Furthermore, three patterns of differentiation have been recently identified: glioblastoma with primitive neuronal component, small cell glioblastoma and granular cell glioblastoma [3, 15].

GBM is composed of different clones of poorly differentiated astrocytes, areas of stromal cell population and a small fraction of stem cells [18]. In a rapidly proliferating malignancy, such as GBM, tumor mass increases together with the metabolic demand for oxygen and nutrients; tumor mass may develop so fast that the distance between blood vessels and tissue overcome the oxygen diffusion limit, which has been estimated to be approximately 150 μm [19]. This leads to the development of hypoxic viable regions, aberrant vasculature (a phenomenon known as angiogenesis) and regional necrosis [19, 20]. The newly formed vessels are tortuous, dysfunctional and result insufficient to satisfy the metabolic requirements of the tumor [20]. The aberrant and immature vasculature is also highly permeable and, together with the disrupted

blood–brain barrier (BBB), is associated with oedema [21]. Other main histological features of GBM include cellular and nuclear atypia, elevated cellular proliferation, diminished apoptosis and formation of pseudopalisades [22]. These cellular architectures develop in proximity of a hypoxic region, which forces the pseudopalisading cells to move to the periphery due to lack of regional blood supply and nutrients [22]. Pseudopalisading cells and necrosis constitute adverse histological features. In fact, they can be considered as a tumor response to an ischemic insult and have been associated with shorter survival [23, 24].

Genomic heterogeneity

Genetic profiles greatly vary within GBM [25]. Philips and colleagues first described three different subclasses of high-grade glial tumors: proneural, proliferative and mesenchymal [25]. Subsequently, different genetic profiles led to the definition of four distinct molecular subtypes (proneural, neural, classical and mesenchymal) showing different responsiveness to treatment and outcome [26]. The proneural subtype occurs typically in young patients, shows longer survival than the other subtypes and presents point mutations in the isoform 1 and 2 of isocitrate dehydrogenase (IDH 1/2). Neural markers (NEFL, GABRA1, SYT1 and SLC12A5) are the characteristic hallmarks of the neural subtype. Patients with classical subtype demonstrate extensive amplification of the gene encoding the epidermal growth factor receptor (EGFR), an alteration that is sporadic in other subtypes. Mesenchymal subtype presents a microenvironment highly populated by inflammatory cells and shows the highest percentage of necrosis in comparison with the other subtypes; the distinctive genetic alteration is the deletion of the Neurofibromin 1 (NF1) gene [26]. Patients with classical and mesenchymal subtypes show prolonged survival when treated with more aggressive therapeutic regimes (concomitant chemo-radiotherapy or more than three consecutive cycles of

chemotherapy) compared to less aggressive treatments [9, 26]. Noushmehr and collaborators defined a further distinct subgroup within the proneural one, named the "glioma-CpG island methylator phenotype (G-CIMP)", which displays hypermethylation at a large number of loci, occurs more frequently in young people and is associated with a more favourable outcome [27]. Subsequently, Brennan and colleagues defined six classes of GBM on the basis of DNA methylation profiles (M1, M2, M3, M4, M6 and the G-CIMP subtype) [28].

Interestingly, Patel *et al.* used single cell RNA sequencing in 430 cells from five primary GBM and reported the coexistence of different gene expression subtypes within the same tumor [29]; this findings suggest that the present subtype classification is a surrogate of a more complex genetic and epigenetic landscape. Consequently, there is an unmet need to define a diagnostic work-up process, which can reflect the pattern and types of tumor heterogeneity in individual GBMs. Secondly, in order to improve the understanding of the hypoxic microenvironment, there is need to validate non-invasive imaging techniques for the quantification of tumor hypoxia, like Magnetic Resonance Imaging (MRI) and Positron Emission Tomography (PET).

Treatment: overview

Patient management requires a multidisciplinary collaboration involving neurosurgeons, neuropathologists, oncologists, radiotherapist and experts in neuroimaging. The current standard of care for newly diagnosed GBM, according to the European Association of Neuro-Oncology (EANO) guidelines [30], should be based on surgical resection of the mass, followed by radiotherapy and chemotherapy, mainly with temozolomide (TMZ, TEMODAR, Merck). TMZ should be used also as adjuvant treatment for 6 months or until progression [5, 30] (see **Table 2.1**).

Treatment in case of recurrence should be tailored considering previous treatments and clinical features of the patient. Treatment should include, in case of resectable mass, a surgical approach. Medical treatment options comprise retreatment with TMZ and therapeutic regimens based on nitrosourea drugs such as carmustine (BCNU) and lomustine (CCNU) [30, 31]. Finally, another promising drug for recurrence of GBM is the antiangiogenic agent bevacizumab (Avastin, Genentech/Roche), a humanized monoclonal antibody directed against VEGF [30].

	Newly diagnosed	Progression
Age < 65–70 years	Resection or biopsy, followed by radiotherapy plus concurrent temozolomide, followed by adjuvant temozolomide	Re-resection, re-irradiation, rechallenge chemotherapy or bevacizumab
Age > 65–70 years	Resection or biopsy, followed by radiotherapy, or temozolomide with or without radiotherapy based on MGMT and performance status	Resection and chemotherapy or radiotherapy

Table 2.1 Management options for glioblastoma. *Adapted from [30].*

2.2 Biology of hypoxia

Hypoxia is a state characterized by inadequate oxygen concentration to allow the normal execution of biological functions [32]. Hypoxia, together with abnormal vasculature, is a particularly relevant feature in gliomas [33]. An important distinction is between acute and chronic hypoxia. Acute (or "perfusion limited") hypoxia is a transient state caused by a reduction of PO_2 as a consequence of inadequate blood flow. Acute hypoxia may result from a transient vascular occlusion or a transient vascular contraction [34]. Acute hypoxia can be followed by reoxygenation due to dynamic changes in micro-regional tumor perfusion within the aberrant vasculature [35]. Chronic (or "diffusion limited") hypoxia, the predominant type of tumor hypoxia, is a long-lasting state, produced by increase of diffusional distances involved in the oxygen delivery as a result of tumor cell growth and inadequate angiogenic response [20].

Tumor hypoxia plays a central role in GBM with observed O_2 concentrations ranging from 0.1 to 3% (or 1-10 mmHg) in tumor hypoxic regions [36-39]. Hypoxia in GBM presents different levels of heterogeneity: among patients, in severity, space distribution and time variability. The heterogeneous spatial distribution of hypoxia results from the mixture of regions populated by oxic cells and areas with variable degree of hypoxia [22]. It has been shown that the majority of cells in GBM present mild to moderate (PO_2 = 2.5%-0.5%) hypoxia, although regions with severe hypoxia (PO_2 < 0.1%) have also been demonstrated [40]. The degree of hypoxia in GBM seems to correlate with the aggressiveness of the tumor, in terms of shorter time to recurrence [41]. Alongside regional heterogeneity, GBM shows also a temporal variability in oxygen consumption, reflecting the dynamic metabolic needs and the adaptive abilities of GBM cells [22]

HIF-1: the key regulator of the hypoxic response

Hypoxia induces complex downstream changes which help the tumor to survive and even flourish in the hostile microenvironment. Hypoxia-inducible factor 1 (HIF-1) is the main transcriptional regulator of this network of hypoxic responses (**Fig. 2.1**) [42].

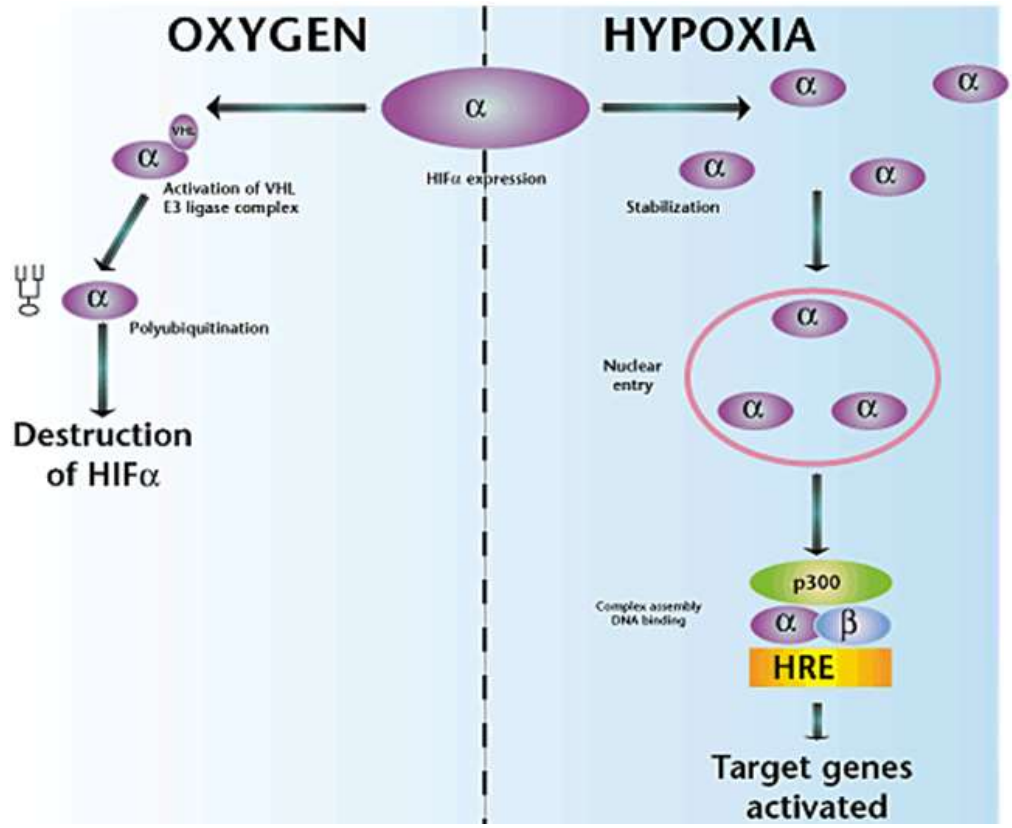

Figure 2.1 Representation of the multiple steps of the HIF transcriptional pathway
In oxygenated cells, HIF-α subunits are destroyed by the ubiquitin-proteasome pathway involving the von Hippel Lindau tumor suppressor protein (pVHL) which interacts with HIF-α. Under hypoxic conditions, this process is suppressed; HIF-α accumulates inside the cells and heterodimerises with the constitutively nuclear HIF-β subunit, binding to hypoxia response elements (HREs), and recruiting co-activators such as p300 [43].

HIF-1 is composed of a variable oxygen-dependant subunit (HIF-1α, HIF-2α or HIF-3α) and the HIF-1β subunit, which is not influenced by the oxygen level [44, 45]. While the oxygen-regulated α isoform (HIF-1α) is ubiquitous, HIF-2α is prevalently expressed in lung endothelium and the carotid bodies [45]; little is known about HIF-3α, which is also commonly expressed in lungs [46, 47]. In normal conditions, the level of HIF-1α remains low, being regulated by two enzymes: the prolyl hydroxylase-domain proteins (PHD) and the factor inhibiting HIF-1 (FIH-1). These enzymes modify specific sites on HIF-1α, allowing interaction with the von Hippel-Lindau protein (pVHL), which is part of an E3 ubiquitin ligase complex, ultimately leading to the proteosomal degradation of the HIF [48]. Under hypoxic conditions, HIF-1α is

stabilized and not degraded, because the activity of PHD and FIH-1 is oxygen-dependant. Hence, HIF-1α can translocate to the cellular nucleus, where it can heterodimerise with the HIF-β subunit and interact with co-activators, such as p300 [43]. Then, HIF-1 binds to specific DNA sites, called HIF-response elements (HREs) and induces the transcription of a broad set of target genes (see **Table 2.2**), leading to a metabolic reprogramming, angiogenic modifications, increased proliferation and enhanced survival [49].

Genes	Function
Cyclin G2, IGF2, IGF-BP1, IGF-BP-2, IGF-BP-3, TGF-α, TGF-β3	Cell proliferation
ADM, EPO, IGF2, IGF-BP1, IGF-BP-2, IGF-BP-3, NOS2, TGF-α, VEGF	Cell survival
NIP3, NIX, RTP801	Apoptosis
c-MET, LRP1, TGF-α	Motility
MIC2	Cell adhesion
EG-VEGF, ENG, LEP, LRP1, TGF-β3, VEGF	Angiogenesis
CAIX	pH regulation
MDR1	Drug resistance
Adenylate kinase 3, Ecto-5'-nucleotidase	Nucleotide metabolism
HK1, HK2, ENO1, GLUT1/3, GAPDH, LDHA, PFKBF3, PFKL, PGK1, PKM, TPI, ALDA, ALDC	Glucose metabolism
Collagen type V (α1), FN1, MMP2, PAI1, Prolyl-4-hydroxylase α (1), UPAR	Extracellular-matrix metabolism

Table 2.2 Genes activated by HIF-1. Adapted from [49]
ADM = adrenomedullin; ALDA = aldolase A; ALDC = aldolase C; CAIX = carbonic anhydrase IX; CATHD = cathepsin D; EG-VEGF = endocrine gland-derived; ENG = endoglin; ENO1 = enolase 1; EPO = erythropoietin; FN1 = fibronectin 1; GLUT1 = c; GLUT3 = glucose transporter 3; GAPDH = glyceraldehyde-3-P-dehydrogenase; HK1 = hexokinase 1; HK2 = hexokinase 2; IGF2 = insulin-like growth-factor 2; IGF-BP1-3 = IGF-factor-binding-proteins; LDHA = lactate dehydrogenase A; LEP = leptin; LRP1 = LDL-receptor-related protein 1; MDR1 = multidrug resistance 1; MMP2 = matrix metalloproteinase 2; NOS2 = nitric oxide synthase 2; PFKBF3 = 6-phosphofructo-2-kinase/fructose-2,6-biphosphatase-3; PFKL = phosphofructokinase L; PGK 1 = phosphoglycerate kinase 1; PAI1 = plasminogen-activator inhibitor 1; PKM = pyruvate kinase M; TGF-α = transforming growth factor-α; TGF-β3 = transforming growth factor-β3; TPI = triosephosphate isomerase; VEGF = vascular endothelial growth factor; UPAR = urokinase plasminogen activator receptor.

One of the most important adaptive changes mediated by the HIF-1 response is the shift from mitochondrial oxidative phosphorylation to aerobic glycolysis, as a preferential metabolic pathway, regardless of the level of available oxygen, a phenomenon called the “Warburg effect” [50]. Aerobic glycolysis requires low oxygen

consumption and yields a lower number of ATP molecules; tumor cells are able to balance the reduced amount of ATP produced by upregulating glucose uptake [19, 51].

Clinical consequences of tumor hypoxia

Hypoxic tumors are known to be associated with amplified resistance to radiotherapy [52]. Indeed, sensitivity of cells to ionizing radiation is highly dependent on the presence of oxygen. When a biological system is irradiated, the formation of free radicals occurs [35]. Free radicals are unstable elements, which derive prevalently from the ionization of H_2O [22]. Free radicals react with oxygen molecules, forming peroxides, which can bind DNA, ultimately causing potentially lethal damage, mainly via DNA single and double-strand breaks [53]. Conversely, when O_2 is low (below at partial pressure of 10 mm Hg), tumour cells acquire radiobiological hypoxia and become up to 3 times more resistant to radiotherapy compared to normoxic cells. In fact, following exposure to irradiation, in presence of low levels of O_2, there is decreased fixation of DNA double-strand breaks, caused by free radicals[35]. Furthermore, in the hypoxic cells, the DNA damage is repaired by donation of hydrogen from donors, such as the sulfhydryl-containing compounds, which restore DNA to its original composition [53, 54].

Tumor hypoxia is also associated to chemo-resistance. The most accepted explanation is that in hypoxic regions the distance between vessels and cells is generally increased, resulting in a lower rate of drug delivery [52]. Furthermore, hypoxia may apply a selective pressure for cells that have lost sensitivity to p53-mediated apoptosis, evading the effects of certain cytotoxic chemotherapeutic agents [55]. Further mechanisms yielding to chemo-resistance include the impaired function of some drugs due to absence of oxygen (such as bleomycin or etoposide) or effects of the acid tumor microenvironment [35].

Similarly, outcome after surgery is less favourable in presence of tumor hypoxia, because hypoxic tumors present augmented tendency to invade normal tissue and develop metastases [55]. Finally, tumor or therapy-related anaemia is an additional issue in oncological patients because the diminished O_2 transport may contribute to worsening of the hypoxic state (see **Fig. 2.2**) [56].

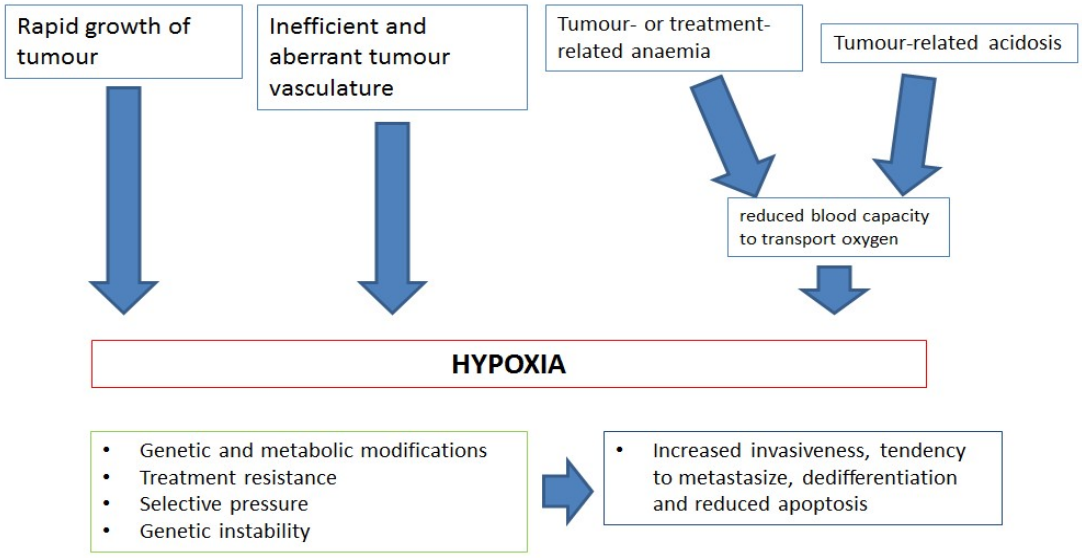

Figure 2.2 Simplified representation of the complex network involving causal factors of hypoxia and relative consequences

Therapeutic implications of tumor hypoxia

Depicting and accurately assessing the distribution of tumor hypoxia may have direct benefit in patient management [32]. Trials employing hypoxia-modifying strategies have demonstrated variable modification of patient outcome (disease-free survival and loco-regional tumor control) in different tumor types; however, these studies lacked accurate assessment of tissue hypoxia, complicating the evaluation of real patient benefit [57-59]. Data regarding the impact of this treatment strategy in brain tumors are scarce. In a metanalysis, including different types of tumors, Overgaard *et al.* did not observe any effect in terms of survival in patients with tumors of CNS, however the authors highlighted the small sample size of the trials included in the analysis [58]. It is conceivable that modern trials should stratify patients according to the level of

hypoxia, identifying subgroups of patients with higher risk of treatment failure, who could theoretically benefit from the introduction of a hypoxia-modifying approach. For example, the assessment of hypoxia by means of non-invasive imaging techniques may help defining personalized RT planning. In this context, encouraging data have been documented by studies reporting the clinical feasibility and improved tumor control in small groups of patients with HNSCC [60, 61].

2.3 Imaging techniques for evaluation of hypoxia (MRI, PET)

Imaging overview

Tumor hypoxia is a significant adverse prognostic factor in GBM, being associated with resistance to treatment and with worse outcome after standard of care therapy [52]. However, despite extensive research, no suitable imaging biomarker for quantifying hypoxic regions has been yet translated to the clinical daily routine. Most clinical trials, in the past, evaluating therapeutic regimens against tumor hypoxia may have failed to replicate the same survival benefit showed in preclinical studies because of unselected patient populations. If we could validate imaging techniques for the evaluation of tissue hypoxia, such as PET or MRI, imaging could help selecting patient, who may benefit from hypoxia-modifying treatments.

At present, most MRI techniques, developed in the effort of quantifying hypoxic regions in GBM, provide indirect measurement of the oxygen level and are influenced by external factors [33]. Recently, a novel MRI method exploiting the week paramagnetic property of oxygen, called oxygen-enhanced MRI (OE-MRI) has been described. Initial results are promising but require further technical and biological validation [62]. In the last decade, the most extensively investigated imaging approach to demonstrate regions of tumor hypoxia has been PET using [^{18}F]Fluoromisonidazole ([^{18}F]FMISO). This radiotracer belongs to the class of nitroimidazoles, compounds

that are selectively retained within hypoxic tumor cells [63]. Only a handful of clinical studies have been performed in cerebral tumors, and, surprisingly, there is no actual biological validation yet of the ability of [^{18}F]FMISO to detect tissue hypoxia in patients with cerebral tumors [64].

Another promising radiotracer is [^{18}F]Fluoroazomycinarabinofuranoside ([^{18}F]FAZA). This second-generation radiolabelled nitroimidazole has recently undergone preliminary assessment in cerebral tumors [65], showing encouraging results in patients with gliomas [65]. Indeed, its lower lipophilicity yields a much higher tumor uptake relative to the background brain tissue, attributable to its faster clearance and, more importantly, to its limited ability to cross the intact blood-brain barrier, resulting in superior contrast to [^{18}F]FMISO. Nevertheless, the breakdown of the blood-brain barrier (BBB) in GBM may confound the interpretation of the radiotracer distribution which can, at any given time following administration, reflect either uptake and retention or simple leakage without complete clearance. Therefore, for validation purposes, it is essential to match information on hypoxia to data on perfusion and permeability of the BBB, derivable from PET with radiolabelled water ([^{15}O]H_2O) and Dynamic contrast-enhanced MRI (DCE-MRI).

Imaging hypoxia with MRI

Despite extensive methodological development, most available non-imaging techniques for the assessment of hypoxia have disadvantages since they are invasive or limited to accessible tumors [52]. Consequently, the development of non-invasive imaging techniques is extremely desirable [52]. At present, a number of MR techniques have been described to investigate hypoxia [36, 52] (**Table 2.3**).

MRI technique	Principles	Limitations
DCE-MRI	Determination of vascular permeability and perfusion by means of an injectable contrast agent.	Indirect measurement of PO_2. Low specificity for hypoxia.
DWI-MRI	Apparent translational diffusion of tissue water.	Indirect measurement of hypoxic cell packing.
BOLD-MRI	Determination of changes in the proportion between paramagnetic deoxyhaemoglobin and diamagnetic haemoglobin.	Many factors affecting the oxygen-haemoglobin dissociation curve (blood flow, haematocrit, CO_2 tension, pH and bisphosphoglycerate concentration) can influence the measurement of hypoxia.
OE-MRI	Increase of the longitudinal relaxation rate (R1) of water due to the paramagnetic property of molecular oxygen.	Need of further validation.
^{19}F MRS/MRI	Perfluorocarbon relaxation properties; direct and quantitative assessment of ptO_2.	No discrimination between necrotic tissue and living cells. Difficulty in clinical translation. Potentially toxicity of the contrast agent.
^{31}P and ^{1}H MRS	Evaluation of metabolite responses related to oxidative metabolism.	Indirect assessment of hypoxia. Limited time and spatial resolution.

Table 2.3 Selected available MRI techniques for the evaluation of hypoxia
DWI**:** diffusion-weighted imaging, BOLD: blood oxygen level dependant; MRS

DCE-MRI

DCE-MRI uses chelates of gadolinium (Gd), such as Gd-diethylenetriaminepentaacetic acid (Gd-DTPA), which diffuse through leaky blood vessels and distribute into the extracellular space [36, 66]. DCE-MRI tracks the passage of an intravenous bolus through the tissue by T1-weighted dynamic MRI sequences, and derives quantitative parameters, with the most utilized parameter being K^{trans}, which reflects both blood flow and capillary endothelial permeability [66]. DCE-MRI signal and oxygen concentration are not directly related, but detection of reduced perfusion shows empirical concordance with tissue hypoxia [33]. Increased vascular permeability can result from angiogenesis and may also be related to hypoxia [66]. More recently specific pharmacokinetic models have been described and appear to allow detection of regional hypoxia by analysis of regional capillary transit time

[66] or by the examination of temporal differences in the arrival time demonstrated on T1 and T2* dynamic acquisitions [67].

DWI-MRI

This MRI technique measures the differences in the motion of water molecules in different tissues. The apparent diffusion coefficient (ADC) is a measure of the magnitude of diffusion of water molecules per unit time [68]. Low ADC has proved as a potentially useful biomarker in cancer, since low ADC is mainly a consequence of high cell density, which can be associated with hypoxia [69]. An inverse correlation between ADCmin and SUVmax ($r = -0.583$, $p < 0.0001$) and between ADCmin and tumor/brain ratio ($r = -0.532$, $p < 0.0001$) seem to exist. These results were reported in a group of patients with low grade glioma (n = 13), glioblastoma (n = 20)and primary central nervous system lymphoma (n = 7) who underwent hypoxia PET imaging with ^{62}Cu-ATSM and DWI-MRI before surgery [70].

BOLD-MRI

Blood-oxygen-level dependent (BOLD)-MRI relies on changes of regional tissue content of deoxyhaemoglobin and oxyhaemoglobin [33] and the ratio between them within vessels. The BOLD effect is related to the amount of paramagnetic deoxyhaemoglobin as it is generated by transfer of molecular oxygen from diamagnetic oxy-haemoglobin. Deoxyhaemoglobin holds a paramagnetic nature and presents higher magnetic susceptibility. An increase of deoxygenated haemoglobin determines an increase of the transverse relaxation rate ($R2^* = 1/T2^*$) of water in blood[33]. Although BOLD-MRI does not need exogenous contrast agents and provides high temporal and spatial resolution images, there are some complicating factors which can make the interpretation difficult. These include the effects of blood

flow, haematocrit, CO_2 tension, pH and bisphosphoglycerate, all of which affect the oxygen-haemoglobin dissociation curve [71]. In order to correctly interpret the R2* images is, therefore, important to determine the distribution of the blood volume, and hence haemoglobin, in the tissue. Knowing the anatomical aspects of the vessel may be not sufficient, because, as assumed by Robinson *et al.*, there could be abundance of vessels in a tumor without corresponding perfusion by red blood cells, and even in presence of vessels, red blood cell transport may not be effective [72].

OE-MRI

Oxygen enhanced magnetic resonance imaging (OE-MRI) exploits the weakly paramagnetic nature of oxygen, which contains two unpaired electrons [73]. Given a source of oxygen (breathing hyperoxic gas), oxygen will not only bind to haemoglobin but also dissolve, as molecular oxygen, in the plasma and causes an increase of the longitudinal relaxation rate (R1) of water [74]. The T1 effect deriving from oxygen-bound haemoglobin during 100% oxygen inhalation is negligible, because the concentration of dissolved oxygen in arterial blood increases much more than the amount of oxygen bound to haemoglobin due to the sigmoid shape of the oxygen-haemoglobin dissociation curve. An increase in oxygen concentration within blood causes also a prolongation of T2*, but the T2* change has a minor impact on signal intensity variation because it is less than 10 milliseconds [75]. Changes in R1, due to hyperoxic breathing, are thought to be proportional to the change in tissue oxygen concentration. Previous studies have demonstrated that these MRI signals in normal tissues are measurable; however, there is lack of experience with solid tumors [62, 74].

Hypoxia PET imaging

An optimal PET radiopharmaceutical to image hypoxia should selectively target clinically relevant hypoxic cells (PO_2 = 0-10 mmHg), be lipophilic to guarantee fast

intracellular transport and sufficiently hydrophilic to allow rapid clearance from normoxic cells in order to provide a high target-to-background ratio (TBR) within a short time from injection [52, 76]. A wide range of PET tracers for imaging hypoxia has been described. These can be broadly divided into two main groups: the 2-nitroimidazole family and non-nitroimidazole compounds (mainly copper-complexed dithiosemicarbazone – [^{60,61,62,64}CU]ATSM – derivatives) [71].

At the present time, the most widely used radiotracer, belonging to the 2-nitroimidazole-based compounds, is [^{18}F]FMISO, which passively diffuses into cells due to its lipophilic nature [71]. Under hypoxic conditions, with $PO_2 \leq 10$ mmHg, the radiocompound undergoes electron reductions and forms reactive radicals. These bind covalently to intracellular macromolecules, so that the tracer is trapped inside hypoxic cells. Conversely, in presence of oxygen, the tracer is reoxygenated and reconverted to the original form, passing out through the cell walls [77].

[^{18}F]FMISO has been assessed and validated in a wide range of human tumors, showing high uptake in hypoxic cells [78]. However, this radiotracer presents some drawbacks including slow clearance kinetics from non-hypoxic tissue resulting in high background in PET images [79]. Early images with [^{18}F]FMISO can be acquired up to 5 minutes after injection to allow estimation of delivery, whereas delayed images, taken about 3 hours after injection, following washout of non-bound tracer, provide estimation of hypoxia. A semi-quantitative analysis is usually performed estimating tumor-to-blood (T/B) and tumor-to-muscle ratios [33, 76, 78]. It is important to select the appropriate time-window for imaging in order to distinguish radiotracer retention from perfusion, which varies between types of tumors and individuals [52]. Some authors found calculation of the tumor hypoxic volume (HV) [80] or of the fractional hypoxic volume (FHV) useful as indicators of the severity and extent of tumor hypoxia

[80, 81]. The measurement of HV, which is the volume of the tumor that is hypoxic, requires the definition of an uptake threshold, while FHV is the percentage of pixels with values greater than a T/B cut-off and requires in addition the estimation of the total tumor volume, most often from anatomical images [33, 52]. According to the available literature, the optimal cut-off of T/B for distinguishing between normoxia and hypoxia ranges between 1.2 and 1.4 at 2-2.5 hours [82, 83]. Some authors have claimed that quantifying hypoxia by simply using semi-quantitative parameters may not be reliable because severely hypoxic areas show low uptake and can be missed by using these approaches. In addition, the spatial disconnection between hypoxic regions and well perfused vessels may cause long diffusion time of the radiotracer [77, 84]. Thus, it has been suggested that a bi-compartmental kinetic model may be necessary to compensate for hypoxic trapping of the tracer together with the effects of perfusion and diffusion in interstitial space [84].

In the attempt to overcome the limitations of [^{18}F]FMISO, new generations of radiolabelled 2-nitroimidazoles for the detection of tumor hypoxia have been developed. Among them, the most promising is probably [^{18}F]FAZA, which is less lipophilic than [^{18}F]FMISO: consequentially non-specific uptake is expected to be washed out more quickly [85, 86]. Additionally, [^{18}F]FAZA exhibits further excellent characteristics such as negligible cell-to-cell line variability and no binding in oxic cells [87]. Peeters and co-workers compared [^{18}F]FAZA with [^{18}F]FMISO and [^{18}F]HX4 (another lipophilic PET radiotracer for the detection of hypoxia) in rhabdomyosarcoma R1-bearing WAG/Rij rats documenting a maximal and stabilized T/B at 3 hours for [^{18}F]HX4 (7.2 ± 0.7) and at 2 hours for [^{18}F]FAZA (4 ± 0.5). Noteworthy, already at 2 hours, [^{18}F]HX4 exhibited a T/B higher or equal to that of the other two radiotracers, whereas TBR for [^{18}F]FMISO was still increasing at 6 hours

(9 ± 0.8) and the tracer did not demonstrate plateau formation at late time-point (6 hours) [88]. PET imaging is able to provide quantitative maps of tumor hypoxia that accurately reflect the hypoxic cell density with a clear spatial link between the radiotracer (e.g. [^{18}F]FAZA) uptake and an immunologically detectable hypoxia marker (e.g. pimonidazole) [89]. Imaging hypoxia with PET may play a role in RT planning, supporting the delivery of higher doses to hypoxic tumors regions [90, 91]. Hypoxia imaging can also predict the success of radio-chemotherapy, as shown by Beck and colleagues, using tumor-bearing mice and the hypoxia-activated chemotherapeutic agent tirapazamine [92].

2.4 Imaging markers of hypoxia, flow and necrosis

Imaging hypoxia in glioblastoma with MRI

T1-weighted oxygen-enhanced MRI (OE-MRI) has been proposed as an alternative imaging technique for the evaluation of hypoxia in the brain. In an animal study, Wu *et al.* [93] used a mechanical ventilation with 100% oxygen at a rate of 8 l/min to investigate hypoxia in brain of rats and found concordance between R2* and R1 changes in white and grey matter in response to oxygen inhalation. T1 values decreased prominently in the cortical grey matter but also, to a lower extent, in the subcortical grey matter and in white matter, where the decrease was the least significant. In contrast, T2 values increased in response to the oxygen inhalation in all the examined regions in the following order: white matter > subcortical grey matter > cortical grey matter. Similarly, the T2* values increased more evidently in the cortical grey matter and white matter and with a less extent in the subcortical grey matter [93]. DCE-MRI parameters have also been investigated for the detection of hypoxia in glioma patients. In particular, Jensen *et al.* demonstrated that capillary transit time (tc) correlates with HIF-1 and VEGF expression in the histopathological examination of

corresponding active tumor regions. Other parameters, blood volume (Vb), capillary heterogeneity (a^{-1}) and k_{ep} (washout rate) also showed a correlation with tissue biomarkers of hypoxia [94]. O'Connor and colleagues, in a study evaluating ten patients with solid tumors, proposed that DCE may provide complementary information to OE-MRI regarding the tumor microenvironment, estimating local perfusion and extravascular volume [74]. Subsequently, Linnik *et al.* investigated a murine glioma xenograft and 5 GBM patients, who underwent the same research protocol as the rats: OE-MRI and DCE-MRI and histological confirmation with reduced pimonidazole adducts and CD31 staining. In addition, the authors calculated the area under the curve (AUC) from the R1 curve and the gadolinium concentration curve. Whereas DCE-MRI did not directly relate to hypoxia in the xenograft model, the authors found a strong correlation between estimation of hypoxia by OE-MRI and histology results, supporting further research to validate also the utility of OE-MRI in the evaluation of response to therapy and prediction of prognosis (**Fig. 2.3**) [62].

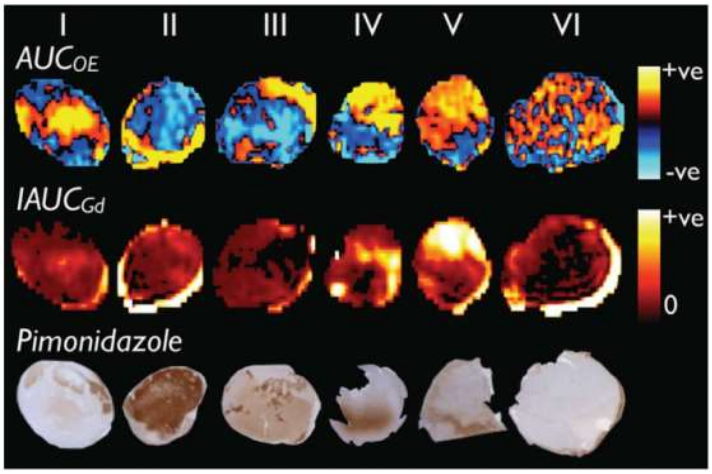

Figure 2.3 Imaging and histology in six U87MG tumors. *Adapted from [62]* Area under the curve for ΔR1 (AUC_{OE}) during 6 min breathing 100% O_2 with positive values displayed using a hot colour scale and negative values using a cool colour scale; IAUCGd: initial area under the contrast agent concentration–time curve at 120 sec post-injection with positive values displayed using a hot colour scale and negative values using a cool colour scale. Bottom row: full field pimonidazole stain images, with brown areas identifying regions of hypoxia. Numerals indicate U87MG tumor index.

MRI: focus on cerebral blood volume and hypoxia

Cerebral blood volume (CBV) has been shown to correlate with histological markers of angiogenesis and tumor aggressiveness [95, 96]. In 2010, Barajas and colleagues demonstrated also that CBV may also indirectly correlate with hypoxia, which was measured qualitatively by a monoclonal antibody targeting CAIX in biopsy samples collected from a total of 16 contrast enhancing (CE) and 14 peritumoral non-enhancing (NE) regions in 13 patients with GBM [95]. The same authors [97] investigated the correlation between histopathological and MRI features using DWI and dynamic susceptibility–weighted contrast-enhanced perfusion imaging (DSC-MRI) in a larger group of GBM patients (n = 51). In each patient, image-guided tissue specimens were obtained from CE and NE regions (93 CE and 26 NE regions from 51 patients with newly diagnosed GBM). In CE regions, CBV was elevated and was associated with increased cellular density, proliferation, microvascular hyperplasia and necrosis [97]. In another study, aiming to investigate the value of DCE derived parameters in distinguishing between high and low-grade gliomas, CBV correlated with HIF-1α and VEGFR-2 expression, which are known to increase under hypoxic conditions [98]. Other further convincing evidence on the existence of a relationship between CBV and hypoxia comes from a study of Jain and co-workers [96]. The authors investigated CBV and PS (permeability surface area) and assessed their correlation with histological hallmarks of hypoxia (microvascular density, microvascular cellular proliferation, VEGFR-2 expression, and tumor cellularity). CBV showed a positive correlation ($p = 0.02$) with microvascular density (MVD). Although not reaching the pre-set statistical significance ($p < 0.05$), CBV seemed to be associated with microvascular cellular proliferation (MVCP, $p = 0.095$), whereas regions with elevated PS demonstrated a significant correlation with MVCP ($p = 0.001$). Furthermore, both parameters showed a positive trend with expression of VEGFR-2. These findings

suggest that high CBV seems to be associated with presence of mature tumor vasculature and high perfusion; in contrast, elevated PS may reflect highly permeable and immature vessels with low blood flow and insufficient oxygen delivery, factors that may contribute to the determination of hypoxia [96].

Li *et al.* also investigated the relationship between lactate, mobile lipids and relative CBV (rCBV) by means of MR spectroscopy and dynamic susceptibility contrast imaging in a mixed group of patients with glioma of different grades, including a subset of patients with grade IV glioma presenting both areas of elevated lipids and areas with elevated lactate. After excluding areas of necrosis from the analysis in this subgroup, because perfusion-time curves are flat in necrotic regions, the authors found a correlation between rCBV and presence of lipids or presence of lactate. However they observed higher rCBV in regions with high lipids and low lactate, compared to regions with high lactate and low lipids in patients with high-grade glioma [99]. Under hypoxic conditions, the HIF-1α pathway leads to the up-regulation of several processes, including angiogenesis and glycolytic metabolism, whose final product is lactate [100]. Furthermore, the heterogeneous vascularisation will be reflected by the inhomogeneous distribution of areas with different grade of perfusion. While some areas will be well perfused, other areas will experience low perfusion, which together with the highly energy consumption of tumor, may result in cell death and regions of necrosis, which can be visible as an elevated lipid peak [99].

Imaging hypoxia in glioblastoma with PET

Hypoxia assessment by PET imaging seems to provide complementary information to MRI within the complex relationship existing between hypoxia and angiogenesis in high-grade gliomas. This was confirmed in a study of Swanson et al, where the authors documented a strong correlation between hypoxic burden, determined with [^{18}F]FMISO,

and altered vasculature, documented on Gd-enhanced T1-weighted MRI sequences [101]. As with other tumors, the prognostic value of [^{18}F]FMISO has been demonstrated in GBM, in a study evaluating the correlation between HV, intensity of hypoxia and survival in 22 patients with GBM who underwent a [^{18}F]FMISO PET scan before biopsy or between resection and RT [102]. Patients with greater hypoxia assessed by maximum tumor-to-blood activity ratio (T/Bmax) and greater HV showed shorter time to progression (TTP) and OS [102].

In contrast, evaluation of hypoxia in GBM with [^{18}F]FAZA has been reported only in one clinical study. This study evaluated the utility of static [^{18}F]FAZA PET scan (started 2-3h p.i.) in 50 patients with different types of tumors and documented increased uptake of the tracer in all gliomas (n = 7), with a TBR range of 1.9-15.6, which is higher than usually reported with [^{18}F]FMISO [65].

Recently, Belloli and colleagues investigated the combined use of [^{18}F]Fluorodeoxyglucose ([^{18}F]FDG) and [^{18}F]FAZA PET with MRI to follow the metabolic, anatomical and hypoxic modifications of specific lines of glioma cells (F98) inoculated (subcortically) in 38 rats. The authors performed weekly dynamic PET animal studies and observed that [^{18}F]FAZA(time: 120-135 min) and [^{18}F]FDG were taken up respectively in the core and in external areas of the tumor. Interestingly, the authors observed a partial overlap of the two tracers in the centre of the Gd-MR positive region. Furthermore the authors found evidence suggesting that necrotic regions, detected as areas with no uptake on the [^{18}F]FDG PET images, may contain hypoxic clusters of tumor cells [103].

The only brain tumor models that have been investigated with both [^{18}F]FAZA and [^{18}F]FMISO are the 9L [104-107] and U251 glioma models [108, 109]. Since these studies have used significantly different methodologies, an accurate comparison is not

feasible. Taking into account the 9L model, Tran and co-workers, using [^{18}F]FAZA, documented a mean TBR of 2.16 ± 0.13 in 10 rats breathing room air on static scan at 3 h p.i.[105].

Static *vs.* dynamic acquisition for the evaluation of hypoxia with PET imaging

Quantification of hypoxia in PET static images can be done by measuring the standardized uptake value (SUV). This is a semi-quantitative parameter reflecting the activity concentration in a region of interest divided by the decay-corrected injected activity normalized by body weight, lean body mass or body surface [110]. SUV should be measured in late imaging in case of static acquisition because hypoxic tissue demonstrates low tracer uptake and can be thus underestimated by a SUV threshold identification method at early time-point [84]. At the moment, the majority of authors, when using static scan, prefer to use a cut-off of tumor-to-blood activity ratio (T/B). For [^{18}F]FMISO, the partition coefficient is 0.44, which results in an almost equal distribution of the tracer between lipophilic tissues and hydrophilic blood and produces normoxic tissues T/B pixel values of almost 1.0. Reasonably, a cut-off of T/B ≥ 1.4 (or even 1.2 at 2-3 hours, according to other authors) may appear acceptable to distinguish hypoxic regions from normal tissue [84].

However the use of T/B may also lead to errors in interpretation because ratios can vary across tumor types and patients [111]. In static acquisitions, the time window has to be selected according to the tumor type and the hypoxic radiotracer [52, 84]. Thus, it is logical to extend the acquisition time in static scans when using lipophilic radiotracers with slow clearance to reach the highest possible T/B for optimal identification of hypoxic regions. Low perfusion, especially at early time-points, is another confounding factor, which may determine slow diffusion into hypoxic cells [52]. Conversely, when hydrophilic tracers are used, acquisition of images can be

performed at shorter interval after injection, due to a faster clearance and maximal T/B occurring in less time [88].

Dynamic acquisition with kinetic modelling enables evaluation of tracer uptake over time and characterisation of both retention and perfusion patterns [52, 84]. Dynamic acquisition takes longer than static acquisition (1-2 h *vs.* 15-30 minutes) but, describing temporal and spatial patterns of the tracers, provides more detailed physiopathological information and a more realistic picture of the hypoxic status. However, accurate kinetic modelling requires arterial sampling for calculation of the input function, which may result in additional discomfort for the patient [112].

Application of kinetic models and calculation of distribution volumes and transport rate constants are important to delineate the characteristics of a tracer. This is extremely important in the evaluation of brain tumors, where the lipophilicity of BBB, although not completely crucial, can play a role in the delineation of hypoxia, at least at early acquisition times [113]. In the study of Bruehlmeier and colleagues, [^{18}F]FMISO showed a higher uptake rate in GBM compared to normal tissue, reflecting slower entrance into normal brain due to an intact BBB, as opposed to the disrupted BBB in GBM. However in the same study, a meningioma (located outside the BBB) with the highest uptake rate constant of all tumors demonstrated only early accumulation of the tracer in comparison to GBM, which showed continuous accumulation on late acquisition, reflecting the existence of an additional tissue compartment governed by a different uptake rate. Thus, late phase of [^{18}F]FMISO uptake reflects more than just a BBB leakage, although there are several factors that can have an impact on [^{18}F]FMISO uptake, including tumor type, cellular density and a nonlinear relationship between retention and PO_2 [113, 114].

The concomitant assessment of hypoxia and perfusion: utility of a dual tracer study ([^{18}F]FAZA/[^{18}F]FMISO and [^{15}O]H_2O) and the issue of heterogeneity in glioblastoma

Tumor hypoxic regions and well-perfused tissue are spatially separated, resulting in long diffusion time for hypoxia tracers [84, 115]. This fact has led to interest in kinetic models taking into account not only tracer uptake but also the diffusion in the interstitial space [84]. Perfusion allows the delivery of nutrient arterial blood to the capillary bed and there is increasing interest in techniques for the evaluation of perfusion and other changes induced by the angiogenic process in the tumor microenvironment [116, 117]. ^{15}O-labelled water ([^{15}O]H_2O) is the PET gold standard for assessing regional cerebral flow (rCBF) in the brain [71, 115]. [^{15}O]H_2O is a freely diffusible tracer, which passes through the vascular walls and diffuses through the interstitial and intracellular spaces [71, 118]. PET scan requires the intravenous injection, as a bolus, of 1 GBq of [^{15}O]H_2O, and dynamic acquisition for 5 minutes [118]. As a freely diffusible PET tracer, however, [^{15}O]H_2O holds some limitations pertaining to the heterogeneous tumor composition. In GBM there are cystic and necrotic regions that are not available for free exchange with [^{15}O]H_2O. This means that a freely diffusible tracer will underestimate perfusion because non-functioning tissues, such as cysts, will be considered as tumor regions; conversely, purely intravascular tracers will overestimate perfusion due to non-functional vascular structures [115]. Despite these limitations, the short half-life (2 minutes) of [^{15}O]H_2O makes it attractive for use in dual-isotope investigations. A dual tracer PET study, utilizing [^{15}O]H_2O and [^{18}F]FMISO in brain tumors, documented no influence of different perfusion patterns in the assessment of hypoxia with the hypoxic radiotracer demonstrating hypoxia in both well and poorly perfused regions of tumors. The unexpected hyperperfused-hypoxic pattern is contrary to the general knowledge that would expect to find hypoxia to occur in poorly perfused regions, as documented in

previous clinical studies and in preclinical studies with mice using tissue derived from primary human glioma or other tumor surgical specimens [119, 120]. The distribution of [^{18}F]FMISO uptake reached the highest value in the tumor margins but not in the central core of the tumor, where perfusion is low. Correlation between pixels in [^{18}F]FMISO and [^{15}O]H_2O images showed correlation at early time points (0-5 minutes after injection) but not at 60-90 minutes or later, suggesting that distribution of [^{18}F]FMISO may be spatially independent of perfusion at a regional level (**Fig. 2.4**) [113].

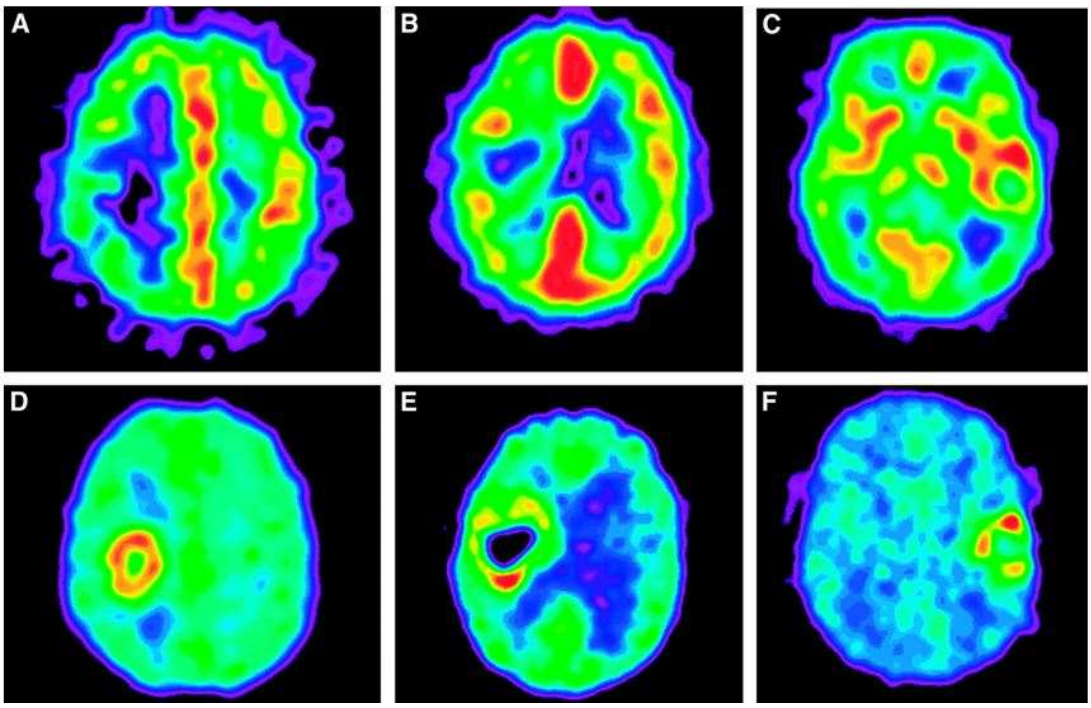

Figure 2.4 Different perfusion-oxygenation patterns. *Adapted from [113].*
(A–C) [^{15}O]H_2O PET perfusion images and corresponding late (150-170 min p.i.) [^{18}F]FMISO PET images (D–F) in 3 patients with GBM (patient n.1: A, D; patient n.2: B, E; patient n. 3: C, F) show tumor hypoxia in low perfusion (A, D), in intermediate perfusion with an inverse pattern compared with hypoxia (B, E), and in high perfusion (C, F). PET images are normalized to their own maximum.

The concomitant evaluation of perfusion and tumor hypoxia by means of [^{15}O]H_2O and [^{18}F]-FAZA has instead been documented by Shi and colleagues [118], who investigated 5 patients with head and neck cancers. In this study the patients underwent

dynamic PET acquisition with [^{15}O]H_2O for 5 minutes and [^{18}F]FAZA for 60 minutes. Assuming an inverse correlation between hypoxia and perfusion and positive correlation between tracer delivery and perfusion, different kinetic models were applied to [^{18}F]FAZA: the 2-tissue-compartment model, the Thorwarth model, the graphical model and the Cho model. The authors found that the 2-tissue-compartment (reversible) model demonstrated the strongest correlation with their expectations [118]. Further studies should explore the exact relationship between perfusion and hypoxia within brain tumors, how the patterns relate to prognosis and how features associated with unfavourable prognosis can be influenced by therapeutic agents or RT [22]. Based on the evidence present in literature, an effective option would be to add molecular imaging studies aiming to evaluate hypoxia and perfusion to multiparametric MRI approach in the clinical work-up of patients with GBM. Multimodality imaging biomarker data could be used to identify potential tissue signatures to be validated by targeted biopsy samples. Collecting imaging information, together with histological data could be exploited in future to create databases designed to provide to the oncologists useful information in order to support management of patients with high-grade glioma [121].

Chapter 3 Effects of High FiO_2 Levels on Cerebral Blood Flow and Brain and CSF Signal

This chapter describes a prospective MRI study. This research material has not yet been submitted for publication but has been presented in the alternative thesis format.

The study design was by Prof Jackson, Dr. Coope and the candidate. Ethical application was by Professor Jackson. The candidate has been involved with the recruitment, data acquisition, data processing, image analysis and statistical analysis. MRI sequence development was by Dr Morris. Interpretation of the results was carried out by Prof Jackson, Dr. Coope and the candidate. Literature review was by the candidate and Prof. Jackson.

Dr Coope has also been involved in the development of the analytical techniques.

The candidate gave his contribution in writing the first draft of the manuscript. Prof Jackson helped in the revision of the manuscript. All authors have provided input into helpful discussions. This study was jointly funded by Cancer Research UK and the Engineering and Physical Sciences Research Council (Grant reference C8742/A 18097).

Abstract

Background: Oxygen-enhanced MRI (OE-MRI) has proved able to quantify tumor hypoxia in patients with a range of tumor types. Clinically translatable image-based approaches for the identification of correct oxygen administration and, consequently, confident quantification of signal change in response to O_2 administration have not yet been described in the head. The main aim of this study was to document the magnitude, timing and distribution of signal changes in grey matter (GM), white matter (WM) and CSF in response to varying levels of administered FiO_2 in healthy normal volunteers and to establish the reproducibility of the changes.

Methods: Ten volunteers were connected though a mouthpiece to a modified "Mapleson A" semi-open anaesthetic circuit and underwent whole-brain OE-MRI

sequences at baseline (FiO_2 = 21%) and under different O_2 concentrations (FiO_2 = 21%,28%, 40%, 60% and 100%). Three subjects underwent the same OE-MRI protocol breathing room air and constituted the control group. Maps for longitudinal relaxation rate (R1) were generated and sampled using a spherical volume of interest (VOI) placed in the suprasellar cistern and masks for grey matter (GM) and white matte (WM). Percentage change in mean R1 from baseline at different FiO_2 was calculated for suprasellar cistern CSF, GM and WM. The significance of the %change from baseline in mean R1 with varying FiO_2 (21%, 28%/40%, 60% and 100%) was assessed using a 2-tailed one samples t-test ($p \leq 0.05$). Reproducibility of magnitude of change and time course for mean R1 in volunteers undergoing the OE-MRI twice (visit 1 and 2) under a FiO_2 of 100% were evaluated, respectively, using 2-tailed one samples t-test ($p \leq 0.05$) and calculating coefficients of correlation for the dynamic course (ascending portion, 100% O_2 portion and descending segment). Mean flow velocities were used to calculate the total flow in the internal carotid arteries and the mean %change for varying FiO_2 levels.

Results: Significant %change in mean R1 was measured only under the administration of a FiO_2 of 100% in suprasellar cistern CSF (4.83%) and GM (0.44%). The summed ICA flow showed significant progressive decrease with increasing values of FiO_2 (Pseudo R-Square = 0.938, p = 0.011). Pre-exposure to high supraphysiological FiO_2 (60%) determined higher increase of mean R1 in response to 100% oxygen in suprasellar cistern CSF compared to pre-exposure to air (7.46% *vs.* 3.49%; p = 0.027) and larger decrease of ICA flow (-45.6% *vs.* -25.7%, respectively; p=0.018). The rise of the dynamic course of mean R1 in suprasellar cistern CSF and GM occurred within 120 sec in most subjects. The average percentage change in mean R1 in response to 100% FiO_2 did not differ significantly between visit 1 and visit 2 for suprasellar cistern

CSF (5.02% and 4.04%, respectively); a low significant difference was found between visit 1 and 2 in GM (0.142% vs. 0.792%; p=0.043). Overall, the slopes of the dynamic course of mean R1 for suprasellar cistern CSF and GM in visit 1 and 2 presented significant correlation.

Conclusions: Mean R1 in suprasellar cistern CSF and GM shows significant increases at a FiO_2 of 100% and demonstrate sufficient reproducibility. Administration of increasing FiO_2 results in significant proportional decreases in CBF in young healthy subjects. We recommend that studies using oxygen challenge in patients with cerebral tumors should confirm O_2 delivery by measurement of signal change in the suprasellar cistern CSF and should characterise the status of the autoregulatory response by measurement of major arterial flow.

Introduction

Hypoxia has a major impact on treatment response and patient outcome in several cancers, including high-grade gliomas [52]. Non-invasive imaging techniques, providing a reliable evaluation of the extent and degree of hypoxia, would be useful to tailor personalised treatment strategies involving hypoxia-modifying treatments [32, 122]. For this reason a number of MRI methods, exploiting the correlation of the tissue relaxation properties to oxygenation, have been investigated in preclinical and clinical studies [36].

Gradient echo sequences, sensitive to changes in the transverse relaxation time T2 have been used for Blood Oxygen Level Dependant imaging (BOLD-MRI) to evaluate the regional tissue content of deoxyhaemoglobin [33]. The paramagnetic nature of deoxyhaemoglobin alters the local field strength and consequently changes the magnetic spin properties of vascular and perivascular water, and decreases the signal

intensity on T2* weighted images [36]. Thus, an increase in deoxyhaemoglobin results in a faster transverse relaxation rate (R2* = 1/T2*). Conversely, a decrease of deoxyhaemoglobin produces a reduction of R2* reflecting a decrease of deoxyhaemoglobin. BOLD-MRI does not directly measure PO_2 since R2* and tissue pO_2 are not directly correlated but it can be used to study acute changes in oxygen delivery [33]. From a physiological perspective, BOLD-MRI is more likely to demonstrate acute tissue hypoxia, due to transient occlusions of small blood vessels rather than chronic hypoxia (related to the development of an increasing distance between hypoxic areas and red blood cells which is beyond the distance over which diffusion of oxygen can provide adequate oxygen delivery)[36]. Furthermore, BOLD-MRI is affected by other factors including blood flow, haematocrit, CO_2 tension, pH and bisphosphoglycerate concentration, all of which affect the oxygen-haemoglobin dissociation curve [71, 72]. BOLD-MRI also requires sequences sensitive to susceptibility change, making image artefacts problematic in some settings. Some authors have attempted to demonstrate correlation of the frequency distribution of DCE-MRI–derived pharmacokinetic parameters (especially, K^{trans} and v_e) with the extent of hypoxic fraction in tumor tissue [33]. However, these parameters are indicative of vascular flow and permeability and do not correlate directly with tissue oxygenation [36]. Other described MRI techniques which offer indirect indications of hypoxia include MR diffusion weighted imaging (DWI) and magnetic resonance spectroscopy (MRS) [33].

More recently, oxygen-enhanced MRI (OE-MRI) has proved able to quantify tumor hypoxia in patients with a range of tumor types [62, 122]. There is evidence that, given a source of high-concentration of inspired oxygen (usually inhalation of 100% O_2), a shortening of the longitudinal relaxation time (T1) results from increased dissolved

oxygen concentration [74]. These changes have been described in normal brain tissue in animal models and in a number of other clinical settings [93]. In areas where oxygen delivery is adequate, administration of 100% O_2 will result in an increase in R1. Conversely, where oxygen delivery is inadequate, additional oxygen delivered to tissue will be rapidly consumed so that no corresponding signal change will be identified. It follows that the T1 shortening effect could be used to potentially evaluate oxygen delivery and detect hypoxaemia in tissue [62].

Since areas of tissue hypoxia will be identified because they fail to show signal change, effective O_2 delivery must be ensured. High FIO_2 has been shown to produce predictable, rapid positive signal changes in sulcal CSF [123]. These changes are small and require optimised image analysis for confident identification but may be used as an indicator of successful administration of high concentrations of oxygen. Clinically translatable image-based approaches for the identification of correct oxygen administration and, consequently, confident quantification of signal change in response to O_2 administration have not yet been described in the head.

The main aim of this study was to document the magnitude, timing and distribution of signal changes in grey matter (GM), white matter (WM) and CSF (suprasellar cistern) in response to varying levels of administered FiO_2 in healthy normal volunteers and to establish the reproducibility of the changes.

Methods

1. Normal volunteers

The local ethical committee approved the study and all the subjects provided informed consent after receiving a brief explanation of the experiment by the investigators. The local institutional review board approved the study. Due to a known progressive decline of cerebral blood flow (CBF) and brain oxygen utilisation with ageing [124],

an age restriction (age range: 20-40 years) was adopted for the recruitment. Further exclusion criteria included: 1) inability to lie still for up to 1 hour comfortably; 2) history of heavy smoking; 3) common contraindications for MRI scanning (pacemaker, history of working with metal at high speed, programmable shunts, metal implants, etc.).

Thirteen normal healthy volunteers (4 females, 9 males; mean age: 30.5 ± 4.03 years; age range: 26-38 years) were recruited at the University of Manchester and were instructed to avoid smoking and substances, such as caffeinated beverages, which may affect brain blood flow, on the day of scanning.

Ten out of 13 volunteers received modified FiO_2 and constituted the "experimental cohort" (3 females, 7 males; mean age: 30.3 ± 4.16 years; age range: 26-38 years). Three out of the 13 volunteers breathed room air over the duration of the scans, these constituted the "control cohort" (1 female, 2 males; mean age: 31 ± 4.36 years; age range: 26-34 years); these subjects breathed room air over the whole duration of the MRI scanning.

2. OE-experimental protocol

Experimental subjects were connected though a mouthpiece to a modified "Mapleson A" semi-open anaesthetic circuit (**Fig. 3.1**) in the MR scanner [125] The anaesthetic circuit was used to provide gas mixtures containing different levels of fraction of inspired oxygen (FiO_2: 21%, 28%, 40%, 60%, 100%) at a rate of 15 litres/min during the OE-MRI experiments (**Table 3.1**).

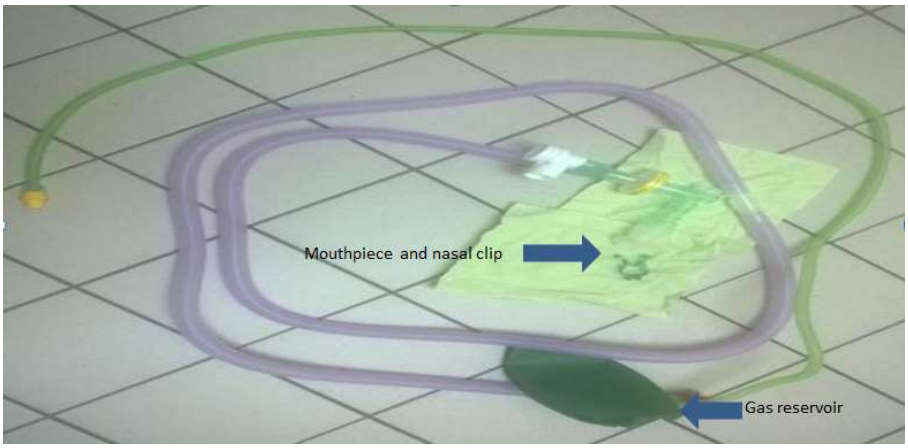

Figure 3.1 Mapleson A semi-open anaesthetic circuit used to deliver different FiO_2 during the OE-MRI experiments.

The PO_2 and PCO_2 levels within the system were constantly sampled using a tubular probe positioned at the level of the mouthpiece. The corresponding gas traces were displayed on a computer monitored by means of a commercial gas sampling unit (ML206 Gas Analyser and Powerlab 8/35; ADInstruments, Oxford, UK) and analysed (Labchart v. 7.3.4, ADInstruments, Oxford, UK).

Three out of the ten subjects of in the gas experimental cohort were scanned on one occasion, 6/10 volunteers underwent two MRI scans and one volunteer underwent three MRI experiments (18 scan sessions in all). The MRI scans included two, four, or five variable flip angle (VFA) dynamic sequences (sequence duration = 40 time-points; frame = 12 sec), acquired in association with different levels of oxygen challenges (FiO_2 = 21%, 28%, 40%, 60% or 100%).

The three subjects forming the control cohort were scanned with the same MRI scan protocol but without any oxygen administration (breathing room air). The oxygen administration paradigms in the experimental and control groups are shown in **Table. 3.1**.

Group	Volunteer	FiO_2 (%)	FiO_2 (%)	FiO_2 (%)	FiO_2 (%)	FiO_2 (%)	Sex	Age
Exp	1 - scan 1	21	40	60	21	N/A	F	26
	2 - scan 1	21	28	100	21	N/A	M	38
	2 - scan 2	21	40	100	21	N/A		
	3 - scan 1	21	100	21	21	N/A	M	28
	3 - scan 2	21	100	21	21	N/A		
	4 - scan 1	21	28	40	21	N/A	M	32
	5 - scan 1	21	60	100	21	N/A	M	27
	5 - scan 2	21	100	40	21	N/A		
	6 - scan 1	21	60	100	21	N/A	M	31
	6 - scan 2	21	100	21	21	N/A		
	7 - scan 1	21	60	100	21	N/A	M	26
	7 - scan 2	21	100	21	21	N/A		
	8 - scan 1	21	100	N/A	N/A	N/A	F	35
	8 - scan 2	21	100	N/A	N/A	N/A		
	9 - scan 1	21	40	60	100	21	M	33
	9 - scan 2	21	28	40	21	N/A		
	9 - scan 3	21	100	21	21	N/A		
	10 - scan 1	21	60	100	21	N/A	F	27
Control	11 - scan 1	room air	room air	room air	room air	N/A	M	33
	12 - scan 1	room air	room air	N/A	N/A	N/A	F	26
	13 - scan 1	room air	room air	N/A	N/A	N/A	M	34

Table 3.1 Summary of all the volunteer scans. Each cell corresponds to a VFA dynamic sequence with specific oxygen challenge (FiO_2 (%)). Volunteers 1-10 = experimental cohort; volunteers 11-13 = control cohort. Exp = experimental.

The OE-MRI experiments were designed to provide a minimum of four measurements of the longitudinal relation rate (R1) for each change in FiO_2. In the experimental cohort all subjects initially received medical air (FiO_2 = 21%) for a period of 8 mins. The 8-minute dynamic scan was then repeated with a change in FiO_2 to a different level (28%, 40%, 60% and 100%) after 2 minutes. FiO_2 variation were made in a randomised order to generate:

1) a group of MRI scans (scans = 8, volunteers = 5) where the subjects were exposed to 100% FiO_2 immediately following baseline FiO_2 (21%);

2) a group of MRI scans (scans = 3, volunteers = 3) in which the volunteers received only low FiO_2 challenges (28%, 40% 60%) after baseline (21%);

3) a group of MRI scans, which started with the baseline FiO_2 (21%), proceeded through intermediate FiO_2 levels (28%, 40% and 60%) and finished with 100% FiO_2 (scans = 7, volunteers = 6).

A phase contrast quantitative flow acquisition (QF) was acquired to measure blood flow through the internal carotid arteries before and after each hyperoxic challenge. In 9/10 volunteers, FiO_2 was returned to baseline (FiO_2 = 21%) on the 10^{th} frame of the last dynamic sequence to evaluate whether the MRI signal had returned to the baseline level after the intermediate supraphysiological oxygen challenges.

3. MRI protocol

The subjects were scanned on a 1.5 T Achieva scanner (Philips Healthcare, Eindhoven, The Netherlands) using a using an eight-channel SENSE head coil.

The MRI protocol included:

1) Survey acquisitions on three planes (TE: 5 ms, TR:15 ms, α: 20°, FOV: 250x250 mm, matrix: 256x256; voxel size: 1x1x10mm; imaging duration: 2 min);

2) T1-w axial structure SENSE acquisition (TE: 4ms, TR 9 ms, α: 8°, FOV 230x230, matrix: 256x256, reconstructed voxel size: 0.9x0.9x1.25 mm; imaging duration: 7 min);

3) three selective high resolution variable flip angle (VFA) whole brain maps (α = 3°, 13° and 18°, TE: 1 ms, TR: 12 ms, matrix: 128x128, FOV 230x230 mm, voxel size: 1.8x1.8x5 mm; imaging duration: 58 sec);

4) 2D phase contrast angiography (PCA) surveys (TE: 5 ms, TR: 20 ms, α = 15°, matrix: 256x256; FOV: 230x230 mm; PC velocity:15 cm/sec, imaging duration: 1 min and 14 sec) in sagittal plane (slice thickness: 80 mm) and in coronal plane (slice thickness: 30 mm) to identify the internal carotid arteries;

5) quantitative flow (QF) measurement by using 2D phase contrast angiography in an axial plane (TE: 6 ms, TR: 10 ms, α = 15°, Velocity encoding = 120 cm/sec, matrix: 80x80, FOV: 160x160 mm, voxel size: 2x2x5 mm;

imaging duration: 1 min and 24sec). ECG gating was performed to cover the whole cardiac cycle and the ECG trigger signals were used to create flow velocity and magnitude images;

6) VFA dynamic sequences (n = 2, 4 or 5 depending on the volunteer scan, as outlined in Table 3.1).

Each VFA dynamic acquisition comprised 40 frames (frame duration = 12 sec), lasting in total approximately 8 min (TE: 1 ms, TR: 12 ms, matrix: 128x128, FOV: 230x230 mm, voxel size: 1.8x1.8x5 mm). The first dynamic sequence was acquired for each subject with a FiO_2 of 21%. The FiO_2 level was changed according to the scheme outlined in Table 3.1 at the 10th frame of the subsequent dynamic sequence. Each VFA dynamic sequence was separated from the following VFA dynamic sequence by a QF measurement (5, vide supra; **Fig. 3.2**). In in 9/10 subjects the last dynamic sequence was obtained with a FiO_2 returned to baseline (FiO_2 = 21%).

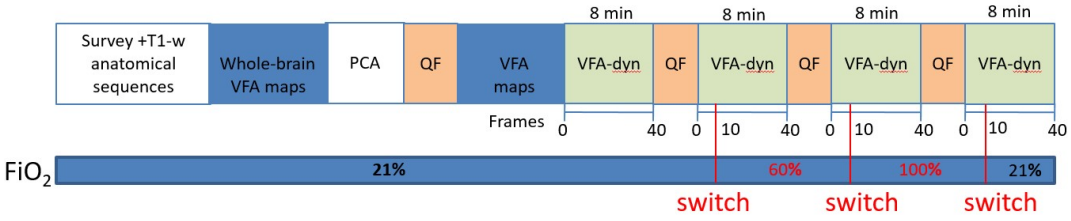

Figure 3.2 Schematic presentation of the OE-MRI protocol with corresponding FiO_2 for volunteer n.6 – scan 1.

In summary, the FiO_2 administration scheme was designed to evaluate:

- the magnitude of signal change in the brain (specifically, GM, WM and suprasellar cistern CSF) in response to varying values of administered FiO_2;
- the time scale of signal changes on initiation and cessation of increased O_2 concentration;
- the impact of a previously administered high O_2 concentrations (e.g. FiO_2 =

60%) on the measurement of the OE-MRI signal change;

- the reproducibility of the signal change in the brain of subjects undergoing the MRI protocol more than once;
- the influence of the administered high FiO_2 on cerebral carotid blood flow.

4. Data processing and analysis

a. Motion correction of the VFA data

For each individual subject scan, motion correction was performed after merging the baseline VFA maps (voxel size: 1.8x1.8x5 mm, 3 frames x 3 repetitions = 9 images) and the 40-frames of each VFA dynamic sequences together, using the mean volume of the concatenated sequence as reference volume for the registration. All these processing steps were performed using FSL (FMRIB Software Library v 5.0).

b. Generation of R1 values and maps

R1 values were calculated from the concatenated motion corrected variable flip angle dynamic series using an in-house R script (R-Project, Levallois Perret, France; library: www.dcemri.com). A flowchart of the processing steps is presented in **Fig. 3.3**.

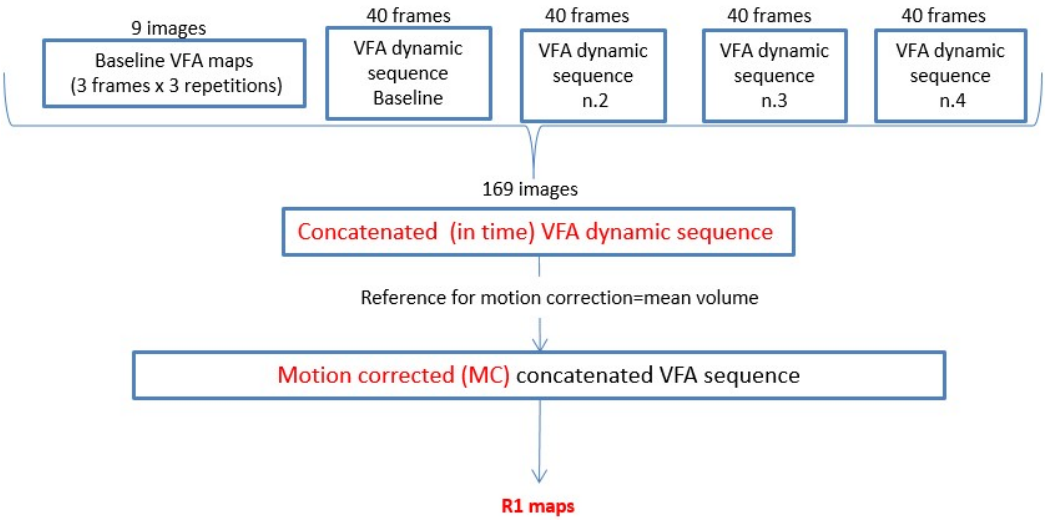

Figure 3.3 Flowchart of the processing steps of the VFA dynamic imaging

c. Tissue-type segmentation and definition of volumes of interest for the R1 maps

Previous studies identified a large change in the suprasellar cistern CSF in response to 100% FiO_2 (17). Accordingly, a spherical VOI (radius: 10 mm) was generated and centred in this region (**Fig. 3.4**). The spherical VOI was created in fslmaths (FMRIB Software Library v5.0) defining the centre of the suprasellar cistern on the mean volume of the concatenated VFA datasets (VFA maps + VFA baseline dynamic sequence + VFA dynamic sequences acquired under different FiO_2).

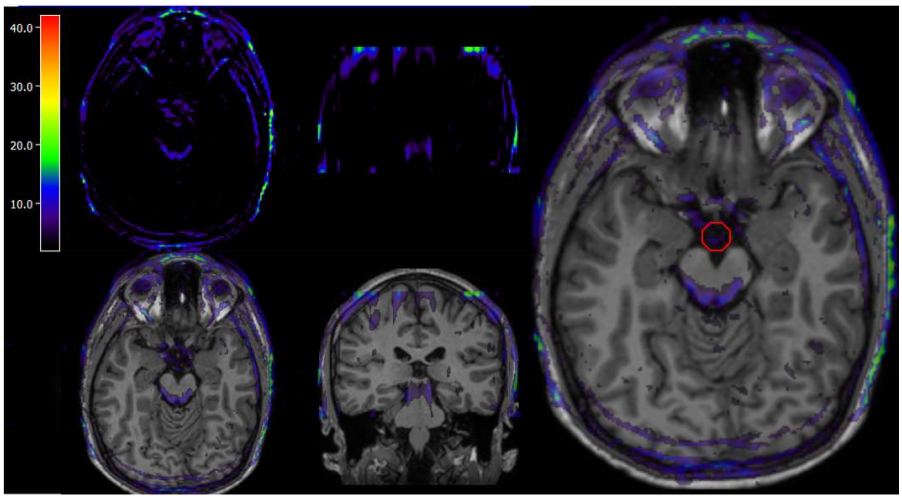

Figure 3.4 Representative Z-score maps (scale: 1.96-40) and corresponding T1w-structural images in a normal volunteer exposed to 100% FiO_2. Higher Z scores are displayed on the suprasellar (red circle) and quadrigeminal cistern CSF.

Volumes of interest (VOI) including GM and WM were defined on the T1-weighted axial images after segmenting the brain from the skull using BET (Brain Extraction Tool) implemented in FSL [126]. This software allows the separation of brain and non-brain tissue based on an intensity threshold (fractional intensity threshold, "f" parameter) in the head images [127]. Furthermore, this tool permits the application of a vertical gradient ("g") to "f", with the purpose of reducing the effect of intensity changes in inhomogeneous images along the vertical direction [128]. The brain extraction was performed using a fractional intensity threshold at of f = 0.4 and a

threshold gradient set at g = 0.2 [129]. These parameters were chosen based on local validation and previous literature [128]. In order to generate masks for GM and WM the high resolution T1-weighted images of each individual MRI scan were automatically segmented using FAST (FSL, FMRIB Software Library v 5.0). The GM and WM masks were systematically visually checked and manually edited using Analyze 11.0 (AnalyzeDirect, Overland Park, KS). The GM and WM masks were subsequently registered to the low-resolution space of the VFA dynamic sequences, to match the spatial resolution of the R1 maps. The masks were then re-sliced using the mean volume of the motion-corrected concatenated VFA dynamic sequence as a reference.

d. Measurement of R1 change

For each FiO_2 challenge, R1 was sampled from every scan using the GM, WM and suprasellar cistern CSF VOIs. Data beyond 3 standard deviations from the mean were excluded to remove outliers. The mean R1 baseline value was obtained by averaging values from frames acquired breathing air (45 frames, n.5-50); the initial 4 frames were excluded from the calculation due to image noise. The mean experimental R1 value for each FiO_2 challenge was calculated from frames acquired during oxygen administration. The first 4 frames were excluded to account for delay in dispensing oxygen inherent in the breathing circuit. Finally, the %change of mean R1 was calculated as:

$$\%\text{changeof mean R1} = \frac{\text{mean R1(challenge)} - \text{mean R1(baseline)}}{\text{mean R1(baseline)}} * 100.$$

e. Reproducibility of changes

The time course of R1 change in suprasellar cistern CSF, GM and WM were represented

by line plots. Frames were also binned (1 bin = 5 frames; duration = 60 sec: 2 sec x 5) in separate plots. An upper boundary consisting of the mean value of R1 + 1 standard deviation was established as a threshold for signal change. The histogram bins in which 1) the threshold was exceeded; 2) peak signal change was reached and 3) signal fell below the threshold following return to medical air were recorded.

Reproducibility of the signal change time course was assessed using repeated scans in seven volunteers. In these subjects, %change of mean R1 in response to 100% FiO_2 in visit 1 was compared to %change of mean R1 under 100% FiO_2 in visit 2 by means of 2-tailed independent samples t-test (p = 0.05). The reproducibility of the histogram bins in which: 1) peak signal change was reached and 2) signal fell below the threshold following return to medical air was examined. The reproducibility of the ascending (FiO_2 switched from 21% to 100%) and descending (FiO_2 switched from 100% to 21%) parts of the R1 time course curve were compared by measurement of the coefficient of determination:

$$r = \frac{1}{n}\sum \frac{(x_{exp}-\overline{x_{exp}})\cdot(x_{mod}-\overline{x_{mod}})}{s_{exp}\cdot s_{mod}}.$$

A further analysis was carried out for each individual undergoing OE-MRI twice to assess the equality of the binned R1 time curves in the two experiements under a 100% FiO_2. Therefore, it was investigated the null hypothesis that the slopes were identical (parallel) considering significant differences only for p values < 0.05.

The segments of the R1 time courses for which reproducibility was investigated are presented in **Fig. 3.5**.

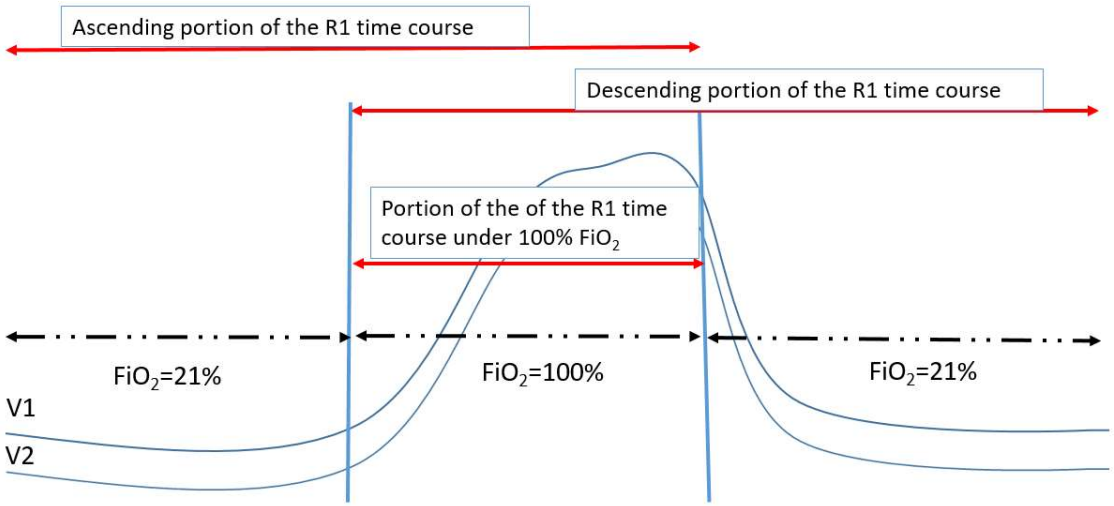

Figure 3.5 Scheme of the reproducibility analysis

f. Measurement of Internal Carotid Blood Flow

Quantitative PCA data were analysed using the open source software Segment version 2.1 (http://segment.heiberg.se) [130]. Two circular region of interest (ROIs) were drawn to delineate the lumen of the internal carotid arteries (ICA) using the magnitude images as reference (**Fig. 3.6**) [131]. Mean flow velocities were used to calculate total ICA flow (right + left ICA) and the mean %change calculated for varying FiO_2 (21%, 28%/40%, 60% and 100%).

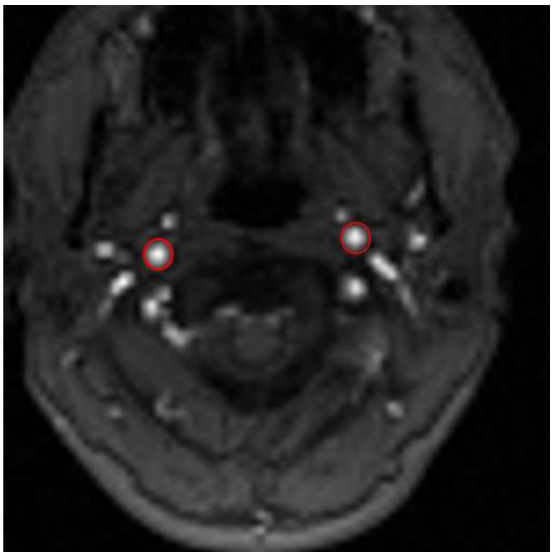

Figure 3.6 Measurement of ICA flow in quantitative PCA imaging in transaxial view.

5. Statistics

Almost all statistics were performed in IBM SPSS v.22 (IBM Corp. Released 2013. IBM SPSS Statistics for Windows, Version 22.0. Armonk, NY: IBM Corp.); GraphPad Prism version 7.04 (GraphPad Software, La Jolla California USA, www.graphpad.com) was used exclusively to compare the regression lines under 100% FiO_2 [132]. Normality of data distributions was evaluated examining the normal quantile-quantile (Q-Q) plots. In the control group, the first dynamic sequence of the OE-MRI scan was treated as the "baseline sequence"; in the suprasellar cistern CSF, mean R1, measured at baseline (n = 3), was compared to mean R1 measured in the challenge sequences (all acquired under room air, n = 5) by means of 2-tailed independent sample t-test, based on literature evidence that this statistical test has the highest power for such small samples [133]. In the experimental group, comparisons were performed for suprasellar cistern CSF, GM and WM. The significance of the %change in mean R1 with varying FiO_2 (21%, 28%/40%, 60% and 100%) was first assessed using a 2-tailed one samples t-test ($p \leq 0.05$) [134]. Subsequently, p values were subsequently calculated for individual %changes by means of 2-tailed independent samples t-test ($p \leq 0.05$), comparing mean R1 in the frames of the "challenge sequence" with mean R1 in the frames of the corresponding baseline sequence. The correlation between the discrete (FiO_2) and continuous (mean R1) variables was calculated as described using the method described by Cox *et al.* [135]. In addition, it was assessed whether pre-exposure to different FiO_2 (low *vs.* high levels) could influence the magnitude of %change in mean R1 triggered by the administration of a specific FiO_2, by means of 2-tailed independent samples t-test.

The significance of percentage changes in total ICA flow, measured from quantitative PCA images, was assessed by 2-tailed one-sample t-test ($p. < 0.05$). The correlation between change in ICA flow and FiO_2 was measured by Cox-Snell R^2. The impact of

pre-exposure to different FiO_2 levels on the measurement of flow at 21% and 100% FiO_2 was assessed using the same methodology described for %change in mean R1.

The hypotheses tested were that:

1) exposure to 100% FiO_2 produces significant changes in mean R1 in CSF, GM and WM;

2) exposure to submaximal FiO_2 (60%, 40%, 28%, 21%) produces signal change in CSF, GM and WM;

3) signal changes in CSF, GM and WM are correlated to FiO_2;

4) previously administered high levels of FiO_2 will not affect subsequent measurements of response to 100% FiO_2 or recovery to baseline levels;

5) administration of high FiO_2 will produce reduction in overall internal carotid blood flow;

6) the magnitude of reduction in internal carotid blood flow correlate with FiO_2.

Results

1) The effect of high FiO_2 on R1 in CSF, GM and WM.

In the control group, no significant signal change was detected in the suprasellar cistern CSF.

In the experimental group, when 100% oxygen was administered following air (15 scans), a significant positive signal change was detected in the suprasellar cistern CSF in almost all cases (significant positive change in 14/15 scans; the non-significant case, patient 3 – scan 1, presented a p value of 0.09). The mean percentage change was 4.83% (C.I.:3.059-6.560; **Table 3.2** and **3.3**; **Fig. 3.7**). Administration of lower FiO_2 following air also produced positive, but not statistically significant %changes in mean R1 in suprasellar cistern CSF, reaching near-significance level (0.061) at 60% FiO_2.

Challenge FiO_2	n.	Average mean R1 at baseline FiO_2	Average mean R1 at challenge FiO_2	%change in mean R1	St. dev of %change	Lower CI (95%) of %change	Upper CI (95%) of %change	Sig. of %change (2-tailed)
21%	21	0.669	0.674	0.413	2.553	-0.798	1.523	0.522
28%/40%	9	0.692	0.694	0.327	1.17	-0.624	1.177	0.499
60%	6	0.620	0.635	2.227	2.217	-0.149	4.503	0.061
100%	15	0.650	0.676	4.83	3.11	3.059	6.560	**< 0.0001**

Table 3.2 Percentage changes in mean R1 of the suprasellar cistern CSF in the experimental cohort at varying levels of FiO_2, assessed by one samples t-test.

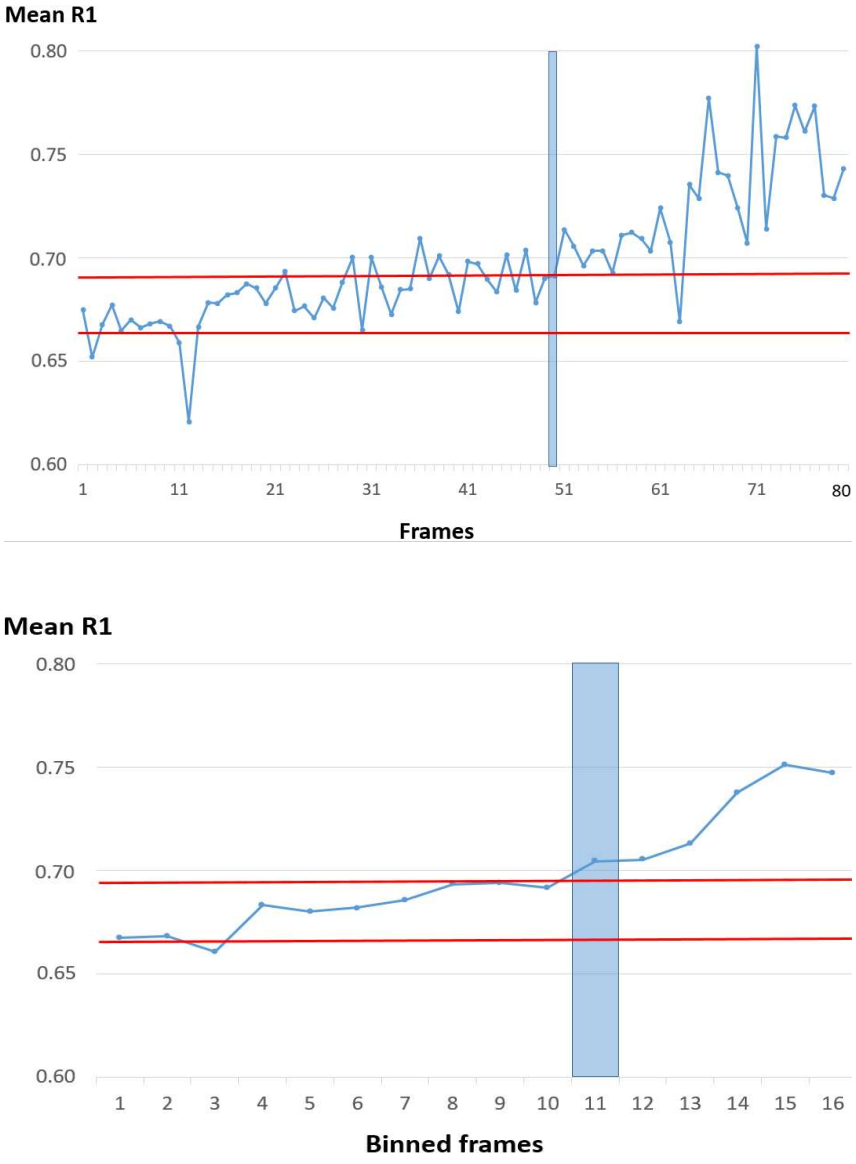

Figure 3.7 Mean R1 dynamic course in the suprasellar cistern CSF. The top graph shows the typical time course of mean R1 in the suprasellar cistern CSF in a normal volunteer (frames 1-50 are acquired under a FiO_2 of 21%); the switch to the FiO_2 = 100% occurs at the 50th frame (vertical light blue bar; frames 51-80 are acquired at a FiO_2 = 100%). The reference lines (red) correspond to baseline mean R1 ± 1 SD. The bottom graph demonstrates the same data using binned frames (1 bin = 5 frames; bin duration = 60 sec) for easier visualization.

Volunteer	FiO_2	%change in mean R1	p value of %change	FiO_2	%change in mean R1	p value of %change	FiO_2	%change in mean R1	p value of %change	FiO_2	%change in mean R1	p value of %change
1 - scan 1	40	-0.969	0.0441	60	-1.697	**0.0006**	21	-3.080	0.000000	N/A	N/A	N/A
2 - scan 1	28	0.173	0.6458	100	1.834	**0.01**	21	-1.994	0.000000	N/A	N/A	N/A
2 - scan 2	40	1.037	0.0038	100	4.807	**< 0.0001**	21	2.341	0.000045	N/A	N/A	N/A
3 - scan 1	100	0.621	0.0987	21	-0.152	0.7085	21	0.138	0.767368	N/A	N/A	N/A
3 - scan 2	100	1.666	**0.003**	21	0.146	0.7359	21	1.532	0.006641	N/A	N/A	N/A
4 - scan 1	28	-0.228	0.6381	40	-0.659	0.1587	21	-1.608	0.004610	N/A	N/A	N/A
5 - scan 1	60	1.756	**0.0071**	100	6.254	**< 0.0001**	21	0.224	0.758922	N/A	N/A	N/A
5 - scan 2	100	1.605	**< 0.0001**	40	-0.935	**0.0198**	21	-2.406	0.000000	N/A	N/A	N/A
6 - scan 1	60	3.077	**< 0.0001**	100	7.400	**0.0198**	21	1.005	0.112925	N/A	N/A	N/A
6 - scan 2	100	3.856	**< 0.0001**	21	-0.776	0.3360	21	-2.381	0.002269	N/A	N/A	N/A
7 - scan 1	60	4.667	**< 0.0001**	100	11.968	**< 0.0001**	21	9.005	0.000000	N/A	N/A	N/A
7 - scan 2	100	6.096	**< 0.0001**	21	2.432	**< 0.0001**	21	1.031	0.047617	N/A	N/A	N/A
8 - scan 1	100	4.186	**< 0.0001**	N/A	N/A	N/A	N/A	N/A	N/A	N/A	N/A	N/A
8 - scan 2	100	6.988	**< 0.0001**	N/A	N/A	N/A	N/A	N/A	N/A	N/A	N/A	N/A
9 - scan 1	40	0.476	0.4633	60	1.865	**0.0163**	100	2.906	**< 0.0001**	21	0.07	0.898
9 - scan 2	28	2.280	**< 0.0001**	40	1.764	**0.0109**	21	0.989	0.089274	N/A	N/A	N/A
9 - scan 3	100	3.503	**< 0.0001**	21	0.450	0.3525	21	-0.458	0.375362	N/A	N/A	N/A
10 - scan 1	60	3.693	**< 0.0001**	100	8.802	**< 0.0001**	21	2.819	0.000030	N/A	N/A	N/A

Table 3.3 Individual percentage changes in mean R1 in suprasellar cistern CSF. Individual percentage changes in mean R1 in suprasellar cistern CSF (from baseline average mean R1: frames 5-50) at different FiO_2 (excluding the initial four frames of the "challenge FiO_2" to account for delay in oxygen dispensing) and corresponding p values, assessed by 2-tailed independent samples t-test.

Percentage changes in mean R1 showed moderate correlation with FiO_2 levels (Pseudo R-Square = 0.428, $p < 0.01$; **Fig. 3.8**). Furthermore, receiver operator curve (ROC) analysis showed that, in the suprasellar cistern CSF, a change in mean R1 > 1.40% from the baseline mean R1, would have distinguished the administration of a FiO_2 of 100% from lower FiO_2 levels with a sensitivity and specificity of 69.44% and 93.33%, respectively (**Fig. 3.9**). When limiting the analysis to dynamic sequences acquired under FiO_2 of 21% and 100%, the same threshold value resulted the best predictor of the administration of 100% FiO_2 with a sensitivity of 93.3% and a specificity of 81%.

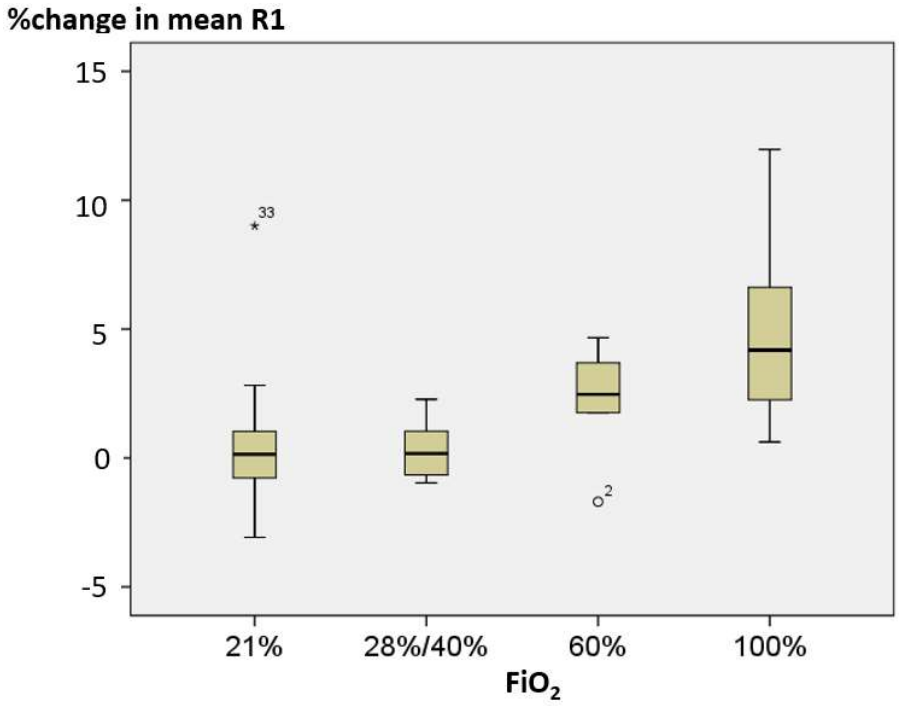

Figure 3.8 Whisker-plot of %changes in mean R1 at varying levels of FiO_2 in the suprasellar cistern CSF

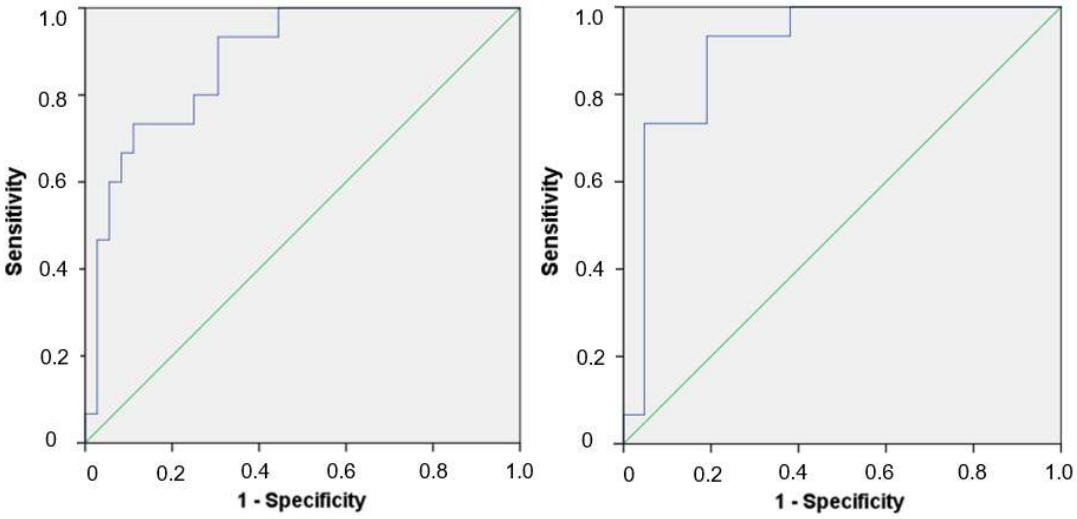

Figure 3.9 ROC curves for prediction of FiO2 administration. Left: ROC curve for prediction of administration of 100% FiO_2 *vs.* lower FiO_2 (21%, 28%, 40% and 60%) in normal volunteers based on percentage change in mean R1 in the suprasellar cistern CSF. Right: ROC curve for prediction of administration of 100% FiO_2 *vs.* 21% FiO_2 in normal volunteers based on percentage change in mean R1 in the suprasellar cistern CSF.

In GM, exposure to a FiO_2 of 100% produced a significant positive change in R1 of 0.438%, (C.I.:0.054-0.721; p = 0.026; **Table 3.4** and **3.5**). However, exposure to FiO_2 values from 21% to 60% produced no significant change in GM-R1. No significant

change in WM-R1 was seen at any level of FiO_2 (**Table 3.6**). Interestingly, a very strong correlation ($R^2 = 0.910$, $p < 0.001$) was found between percentage changes of mean R1 of GM and WM in volunteers scans acquired under a FiO_2 of 100%.

Challenge FiO_2	n.	Average mean R1 at baseline FiO_2	Average mean R1 at challenge FiO_2	%change in mean R1	St. dev of %change	Lower CI (95%) of %change	Upper CI (95%) of %change	Sig. of %change (2-tailed)
21%	21	0.889	0.889	-0.121	0.676	-0.477	0.133	0.254
28%/40%	9	0.847	0.852	0.311	0.411	-0.055	0.576	0.093
60%	6	0.861	0.865	0.020	0.261	-0.304	0.244	0.790
100%	15	0.906	0.909	0.438	0.602	0.054	0.721	**0.026**

Table 3.4 Percentage changes in mean R1 in GM in the experimental cohort at varying levels of FiO_2, assessed by one samples t-test

VOLUNTEER	FiO_2 = 100%	
	%change in mean R1	p value of %change (from baseline average)
2 - scan 1	0.061	0.521053
2 - scan 2	2.150	**< 0.0001**
3 - scan 1	-0.065	0.4160
3 - scan 2	0.108	0.102
5 - scan 1	0.089	0.069
5 - scan 2	0.261	**0.0169**
6 - scan 1	-0.158	0.1912
6 - scan 2	1.152	**< 0.0001**
7 - scan 1	0.771	**< 0.0001**
7 - scan 2	0.410	**< 0.0001**
8 - scan 1	0.056	0.4314
8 - scan 2	0.750	**0.0005**
9 - scan 1	0.244	0.0570
9 - scan 3	0.709	**< 0.0001**
10 - scan 1	0.035	0.6719

Table 3.5 Individual percentage changes in mean R1 in GM. Individual percentage changes in mean R1 in GM (from baseline average mean R1: frames 5-50) at 100% FiO_2 (excluding the initial four frames of the "challenge FiO_2" to account for delay in oxygen dispensing) and corresponding p values, assessed by 2-tailed independent samples t-test.

Challenge FiO_2	n.	Average mean R1 at baseline FiO_2	Average mean R1 at challenge FiO_2	%change in mean R1	St. dev of %change	Lower CI (95%) of %change	Upper CI (95%) of %change	Sig. of %change (2-tailed)
21%	21	1.187	1.186	-0.153	0.675	-0.510	0.104	0.183
28%/40%	9	1.115	1.117	0.182	0.396	-0.172	0.436	0.347
60%	6	1.133	1.132	-0.073	0.198	-0.330	0.085	0.190
100%	15	1.1195	1.1196	0.154	0.579	-0.216	0.425	0.497

Table 3.6 Percentage changes in mean R1 in WM. Percentage changes in mean R1 in WM in the experimental cohort at varying levels of FiO_2, assessed by one samples t-test.

2) Does pre-exposure to high FiO_2 affect observed change in R1?

In experiments, where exposure to a FiO_2 of 100% was immediately preceded by a "preload" FiO_2 of 60%, the resulting %changes in mean R1 measured in GM and WM were unchanged compared to pre-exposure to 21% FiO_2 . Conversely, percentage change of mean R1 in the suprasellar cistern CSF was significantly higher (p = 0.027) in experiments where exposure to a FiO_2 of 100% was preceded by a FiO_2 of 60% rather than air: 7.46% (C.I: 3.33-11.60) *vs.* 3.49% (C.I.:1.70 - 5.43) (**Fig. 3.10**). Under the administration of air, %change in mean R1, was not influenced by preliminary exposure to different FiO_2 levels (100% vs. 28%/40%/60%, **Fig. 3.10**), neither in suprasellar cistern CSF (%change in mean R1 = 1.27% *vs.* -1.53%; p = 0.086) nor GM (%change in mean R1 = -0.12% *vs.* 0.007%; p = 0.79) nor WM (%change in mean R1 = -0.10% *vs.* -0.01%; p = 0.82).

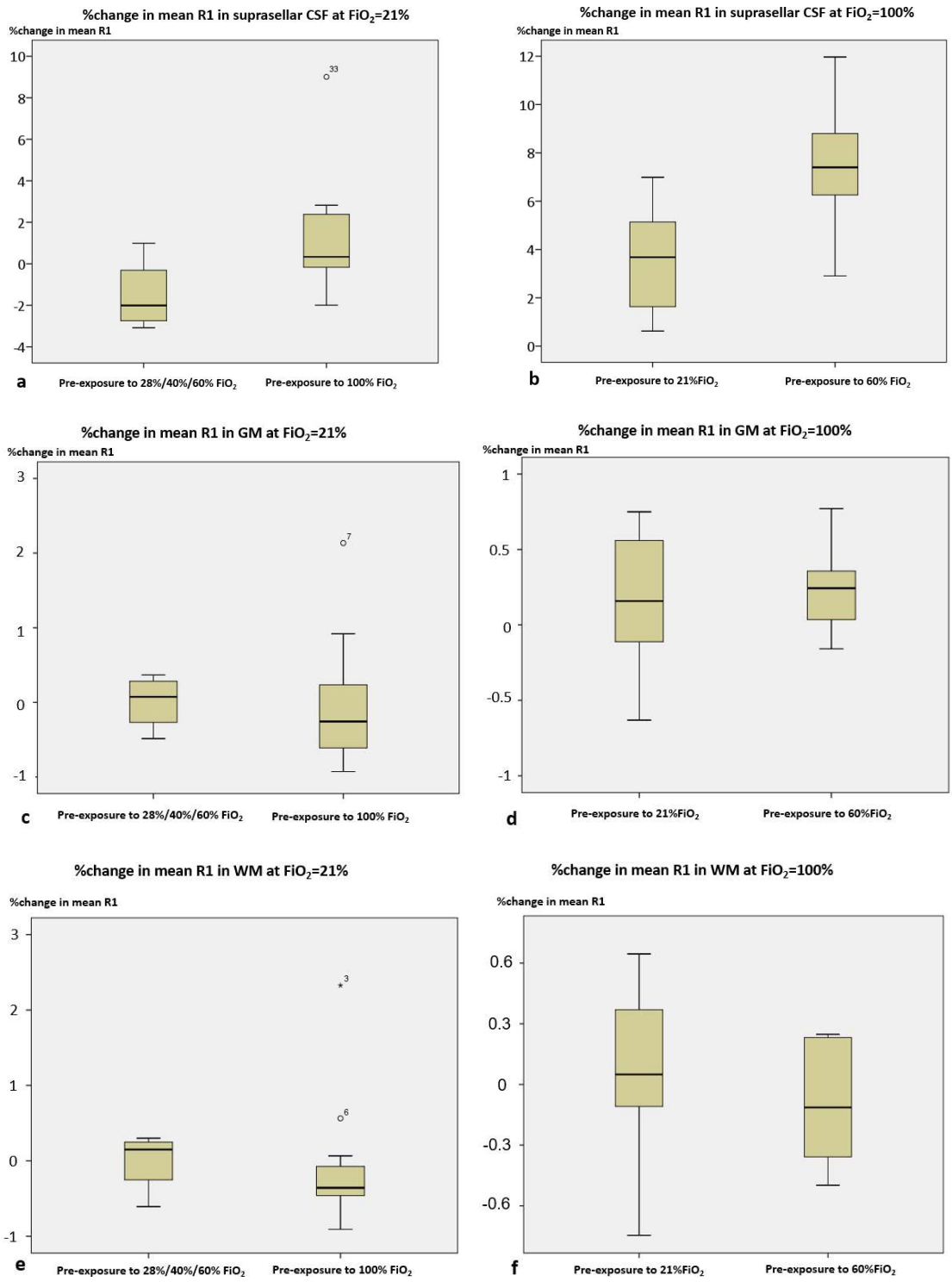

Figure 3.10 Effect of pre-exposure to high FiO_2 on %change of mean R1 in suprasellar cistern CSF, GM and WM. Left column: %changes in mean R1 from baseline level at return to air preceded by submaximal (60% or less) or maximal (100%) FiO_2 levels in suprasellar cistern CSF (**a**), GM (**c**) and WM (**e**). Right column: %change in mean R1 at 100% FiO_2 from the baseline, with pre-exposure to a FiO_2 of 60% or direct switch from baseline FiO_2 (21%) in suprasellar cistern CSF (**b**), GM (**d**) and WM (**f**).

3) Time course of signal change in CSF, GM, and WM

In the suprasellar cistern CSF, the rate of rise in mean R1 was variable. Most cases exceeded the threshold in the bin 1 (11/15; within 60 sec), whereas four subjects exceeded the threshold in bin 2 (60-120 sec). The peak R1 was reached in in the last three frame bins in 11/15 cases. After switching from 100% FiO_2 to 21% FiO_2 the mean R1 dropped below the threshold within 120 sec in 8/13 subjects. In four subjects, where the exposure to 100% FiO_2 was preceded by 60% FiO_2, the drop below the threshold value was slower (180 sec, 240 sec, 360 sec and not reached in one case). The time course of mean R1 in suprasellar cistern CSF was also evaluated at submaximal levels of FiO_2; examination of the plots revealed a relationship between the amplitude of signal change and FiO_2 (**Figure 3.11**).

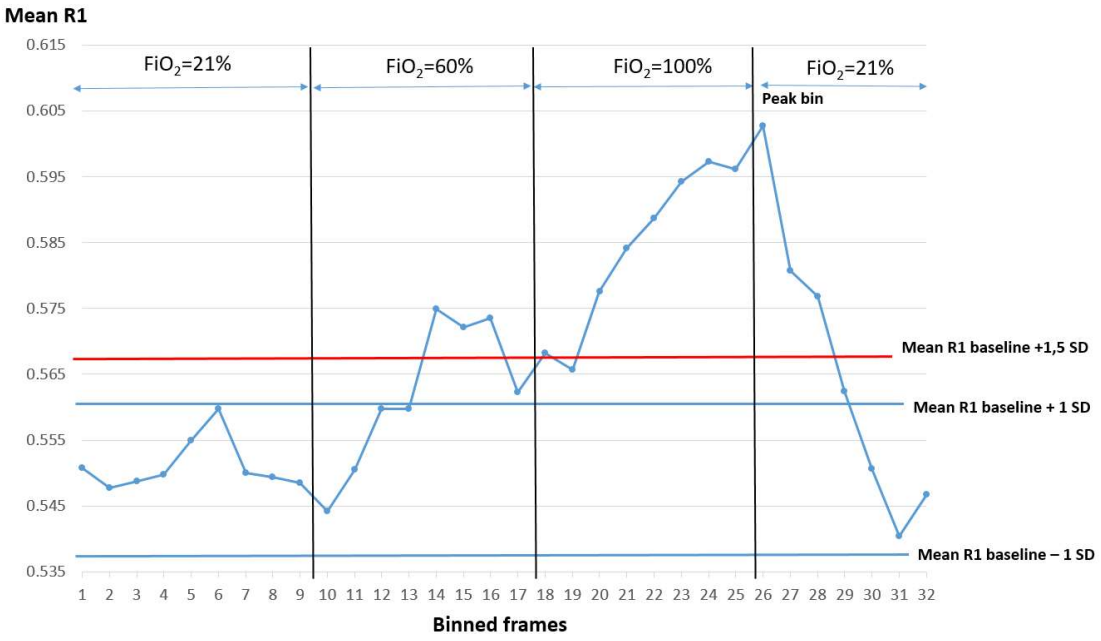

Figure 3.11 Dynamic course of mean R1 in suprasellar cistern CSF. Dynamic course of mean R1 in suprasellar cistern CSF (volunteer 6, scan 1); frames are binned (1 bin = 5 frames; bin duration = 60 sec).

The time course of change of mean R1 in GM, at least in some patients, was similar to the time course in CSF although the magnitude of change was smaller. Following the

administration of 100% FiO_2, the threshold was surpassed in the first 2 bins in 10/15 scans and the peak value occurred in the last three bins of the dynamic sequence, corresponding to the peak bin in CSF in 6/15 volunteers. The R1 time course curve in WM was difficult to evaluate with low magnitude change (see **Fig. 3.12**); peak values were reached within the last three bins in 8/15 cases.

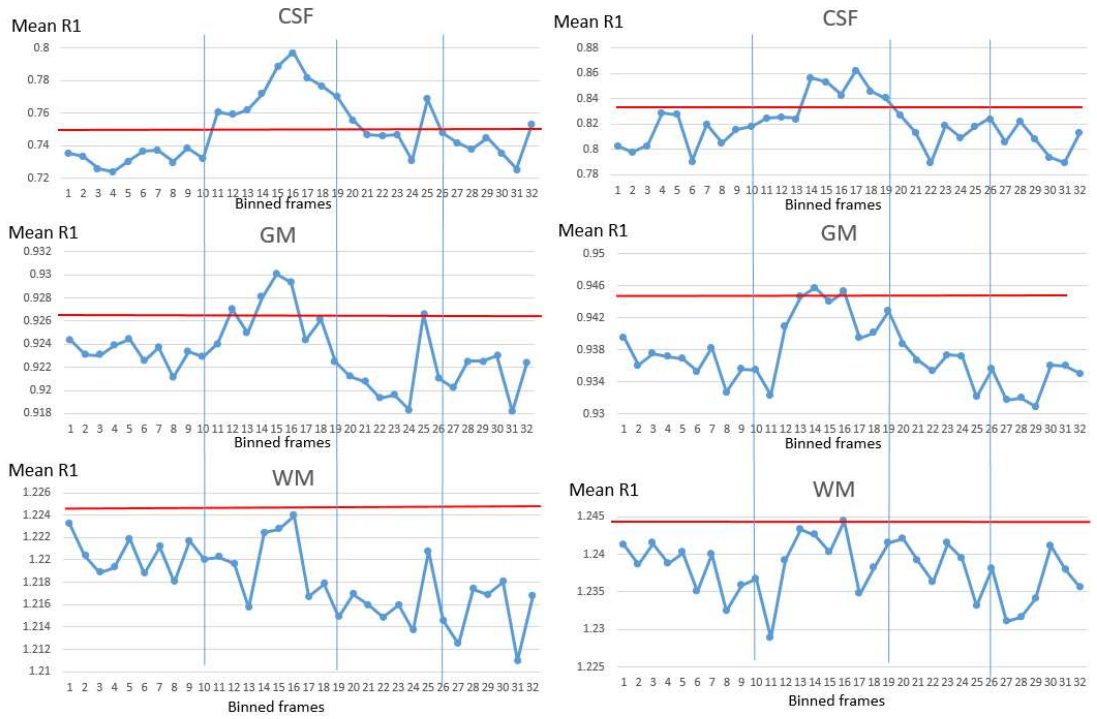

Figure 3.12 Time course of mean R1 in the CSF, GM and WM. Time course of mean R1 in the CSF, GM and in two volunteers undergoing the OE-MRI experiment under the following FiO_2 sequences: 21%, 100%, 21%, 21%; red lines correspond to baseline mean R1 + 1 SD. Vertical blue line corresponds to the switch of FiO_2.

4) Reproducibility of time course in CSF, GM, WM in normal volunteers.

The reproducibility of the dynamic curves was assessed using the binned data (excluding the first bins of the sequences to account for the noise and oxygen delay) and converting for each bin the absolute mean R1 value to %change from baseline mean R1. The baseline mean R1 was calculated averaging the mean R1 in the bins of the baseline sequences.

Since significant changes in mean R1 were not seen in WM in response to 100% FiO_2

coefficients of determination (CoD) were derived only for suprasellar cistern CSF and GM. In suprasellar cistern CSF, the average percentage change in mean R1 in response to 100% FiO_2 did not differ significantly between visit 1 and visit 2 (5.02% vs. 4.04, respectively; $p = 0.577$). For suprasellar cistern CSF, calculated CoDs demonstrated significant correlation between the rates of change in the ascending portion of the R1 time courses of visit 1 and 2 in 6 out of 7 subjects (FiO_2 switched from 21% to 100%; $R^2 = 0.546$, CoD = 0.739 ± 0.172). Significant CoDs were also found for the descending segments of the R1 mean time courses in 4/6 subjects (FiO_2 switched from 100% to 21%; $R^2 = 0.448$, CoD = 0.669 ± 0.225) (see **Table 3.7**).

	Coeff. Det. (challenge)	Coeff. Det. (back to baseline)
Volunteer 2	**0.819**	0.280
Volunteer 3	0.401	0.556
Volunteer 5	**0.690**	**0.932**
Volunteer 6	**0.816**	**0.759**
Volunteer 7	**0.929**	**0.743**
Volunteer 8	**0.836**	N/A
Volunteer 9	**0.684**	**0.745**
Mean	0.739	0.669
SD	0.172	0.225

Table 3.7 Coefficient of determination for the ascending portion (challenge) and descending (back to baseline) portion of the mean R1 dynamic course in suprasellar cistern CSF of normal volunteers undergoing the OE-MRI experiment twice. FiO_2 order: (21%, 100%, 21%). Significant correlation ($p < 0.01$) are presented in bold.

The slopes of %change in mean "R1 in suprasellar cistern CSF in visit 1 and 2, in response to 100% FiO_2, did not present significant differences in 6/7 cases (**Table 3.8** and **Fig. 3.13**).

	Vol. 2	Vol. 3	Vol. 5	Vol. 6	Vol. 7	Vol. 8	Vol. 9
p values	**0.208**	**0.939**	**0.885**	**0.054**	**0.067**	0.007	**0.79**

Table 3.8 Comparison of slopes under the administration of 100% FiO_2 in the suprasellar cistern CSF in normal volunteers undergoing OE-MRI twice. P values > 0.05 indicate absence of significant differences between the two visits.

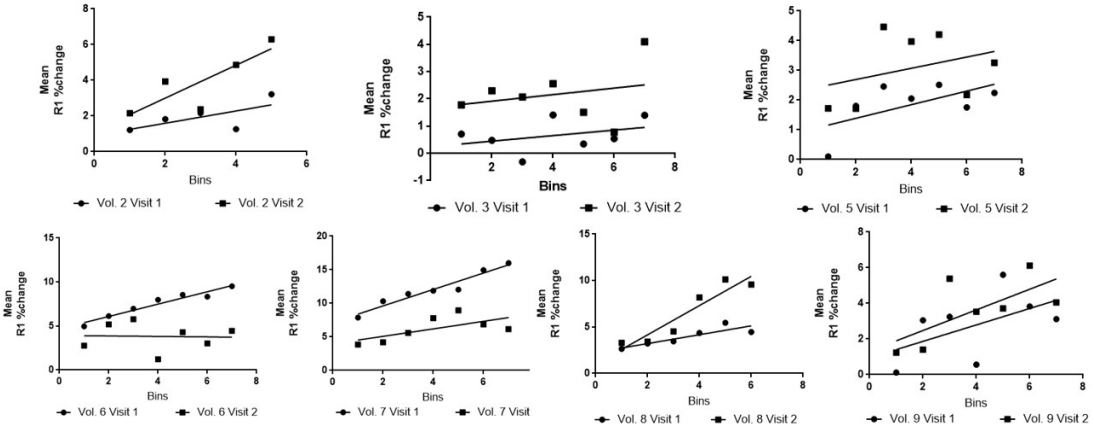

Figure 3.13 Linear regression plots (binned data) of mean R1 %change (FiO_2 = 100) from baseline in suprasellar cistern CSF (visit 1 and 2).

Differently, in GM a significant difference in mean R1 change at a FiO_2 of 100% was documented between the two visits (0.142% vs. 0.792%; p = 0.043). Responses to switch from 21% FiO_2 to 100% FiO_2 demonstrated low reproducibility, whereas the R1 mean dynamic courses demonstrated moderate reproducibility (R^2 = 0.270, CoD = 0.520 ± 0.552) in response to the return to baseline conditions (from 100% FiO_2 to air; **Table 9**). The slopes of %change in mean R1 in GM in visit 1 and 2, in response to 100% FiO_2, did not present significant differences in 6/7 cases (**Table 3.10**; **Fig. 3.14**).

	Coeff. Det. (challenge)	Coeff. Det. (back to baseline)
Volunteer 2	0.053	-0.578
Volunteer 3	0.397	0.561
Volunteer 5	0.037	**0.640**
Volunteer 6	-0.280	**0.817**
Volunteer 7	**0.693**	**0.775**
Volunteer 8	-0.044	N/A
Volunteer 9	0.488	**0.904**
Mean	0.192	0.520
SD	0.342	0.552

Table 3.9 Coefficient of determination for the ascending portion (challenge) and descending (back to baseline) portion of the mean R1 dynamic course in GM of normal volunteers undergoing the OE-MRI experiment twice. FiO_2 order: (21%, 100%, 21%). Significant correlations ($p < 0.01$) are presented in bold.

	Vol. 2	Vol. 3	Vol. 5	Vol. 6	Vol. 7	Vol. 8	Vol. 9
p values	**0.208**	**0.161**	**0.260**	**0.853**	**0.367**	0.0003	**0.89**

Table 3.10 Comparison of slopes under the administration of 100% FiO_2 in GM in normal volunteers undergoing OE-MRI twice. P values > 0.05 indicate absence of significant differences between the two visits**.**

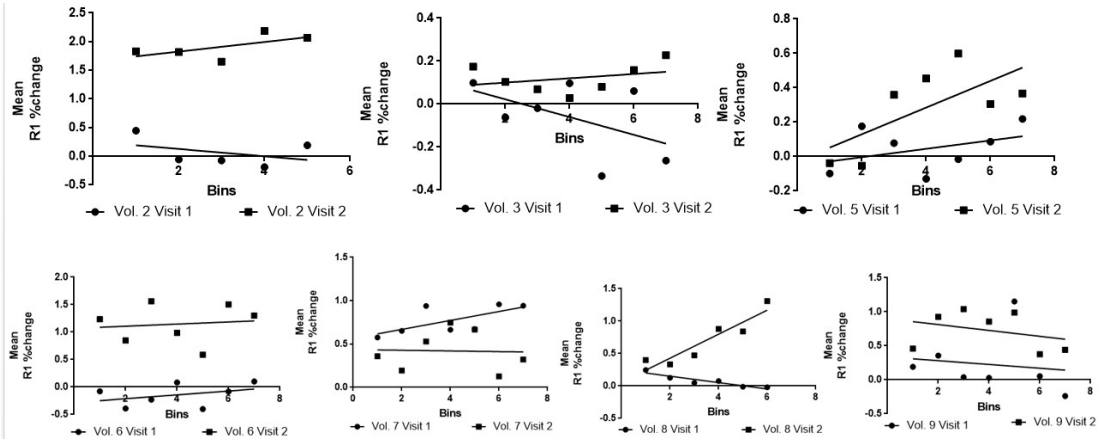

Figure 3.14 Linear regression plots of binned data of mean R1 %changes (FiO_2 = 100) from baseline in GM (visit 1 and 2).

5) Impact of FiO_2 on ICA flow

ICA flow data was available for analysis in 14 out of 18 MRI experiments. The summed ICA flow showed significant progressive decrease with increasing values of FiO_2. The percentage change in total ICA flow from baseline showed significant

correlation with the increase in FiO_2 (Pseudo R-Square = 0.938, p = 0.011; **Table 3.11** and **Fig. 3.15**).

Challenge FiO_2	n.	Average flow at baseline FiO_2 (mL min^{-1})	Average flow at challenge FiO_2 (mL min^{-1})	%change	St. dev of %change	Lower CI (95%) of %change	Upper CI (95%) of %change	Sig. of %change (2-tailed)
21%	31	0.493	0.490	-0.674	9.84	-4.284	-2.935	0.705
28%/40%	9	0.466	0.442	-11.613	13.405	-22.120	-1.106	**0.039**
60%	6	0.504	0.453	-20.241	13.827	-34.751	-5.731	**0.016**
100%	11	0.497	0.410	-34.429	13.707	-46.63	-25.22	**< 0.0001**

Table 3.11 %change of ICA flow from baseline flow (baseline FiO_2 = 21%) at different FiO_2 levels

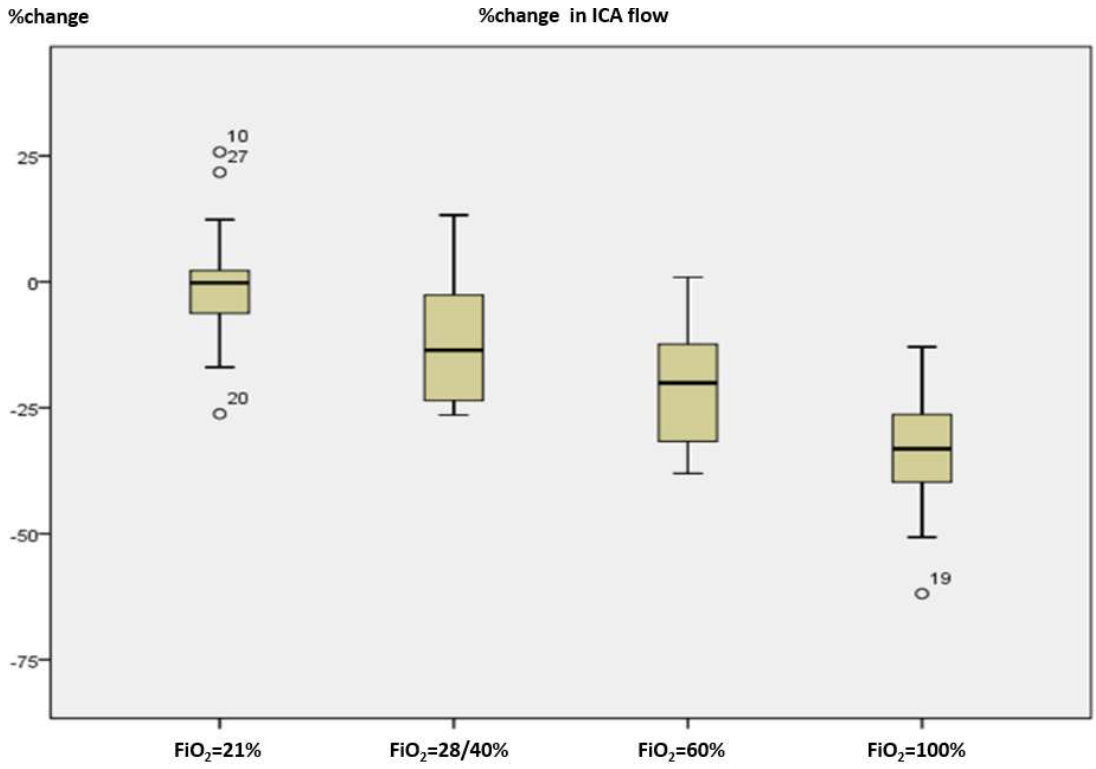

Figure 3.15 Whisker-plot of %change of ICA flow at different FiO_2

The reduction in ICA flow at 100% FiO_2 was significantly greater when the subject had been immediately previously exposed to 60% FiO_2 (-45.6%) rather than air (-25.7%; p = 0.018). The ICA flow at a FiO_2 of 21% was not affected by previous

exposure to a FiO_2 of 100% rather than lower FiO_2 levels (**Fig. 3.16**).

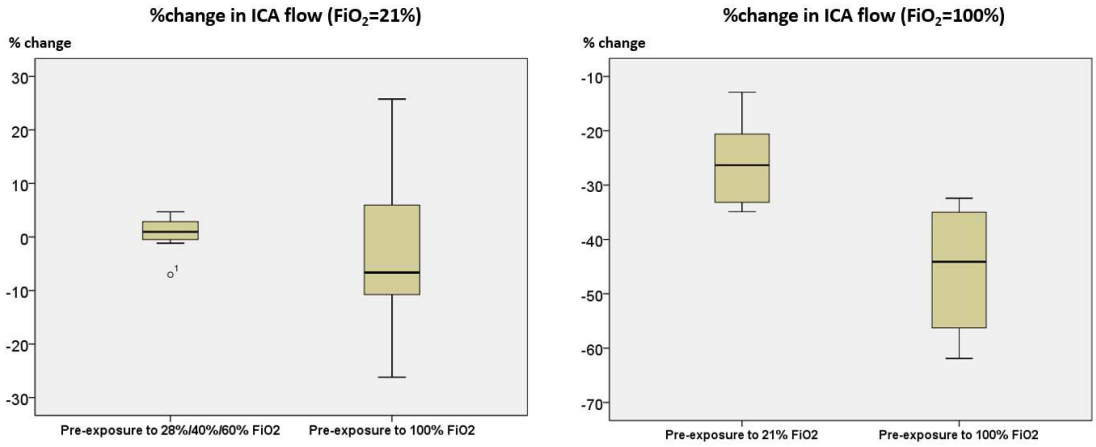

Figure 3.16 Effect of pre-exposure to high FiO_2 on ICA flow. Left: %change in total ICA flow at FiO_2 = 21% from baseline flow (FiO_2 = 21%) with pre-exposure to 21%/28%/40%/60% FiO_2 *vs.* pre-exposure to 100% FiO_2. Right: %change in total ICA flow at FiO_2 = 100% compared to baseline flow (FiO_2 = 21%) with pre-exposure to 21% FiO_2 *vs.* pre-exposure to 60% FiO_2.

Individual percentage changes in changes in total ICA flow in subjects demonstrated a strong inverse correlation with percentage changes in mean R1 in suprasellar cistern CSF (R^2 = 0.552, p < 0.001, **Fig. 3.13**).

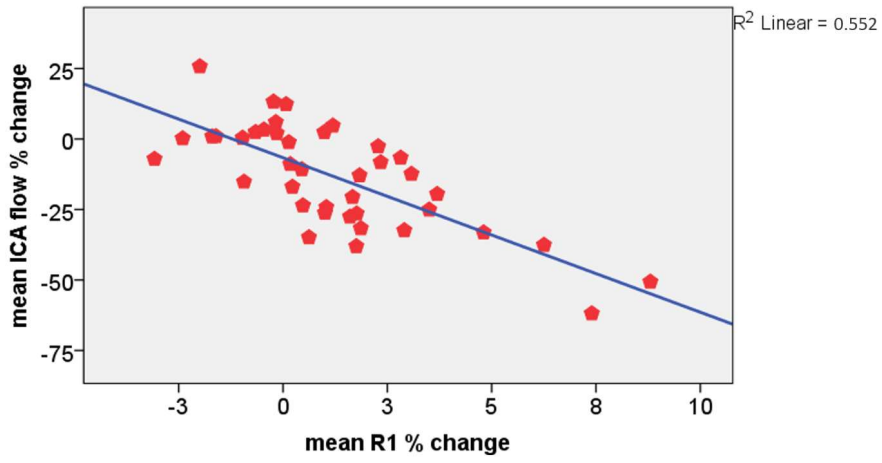

Figure 3.17 Scatter plot showing the correlation of percentage changes in mean ICA flow and in mean R1 in suprasellar cistern CSF.

At a FiO_2 of 100%, total ICA flow presented higher %change decreases in volunteers with higher %change in mean R1 in suprasellar cistern CSF (R^2 = 0.614, p = 0.007);

this relationship resulted not significant taking into account only administration of air ($R^2 = 0.119$, $p = 0.191$) **Fig. 3.18**).

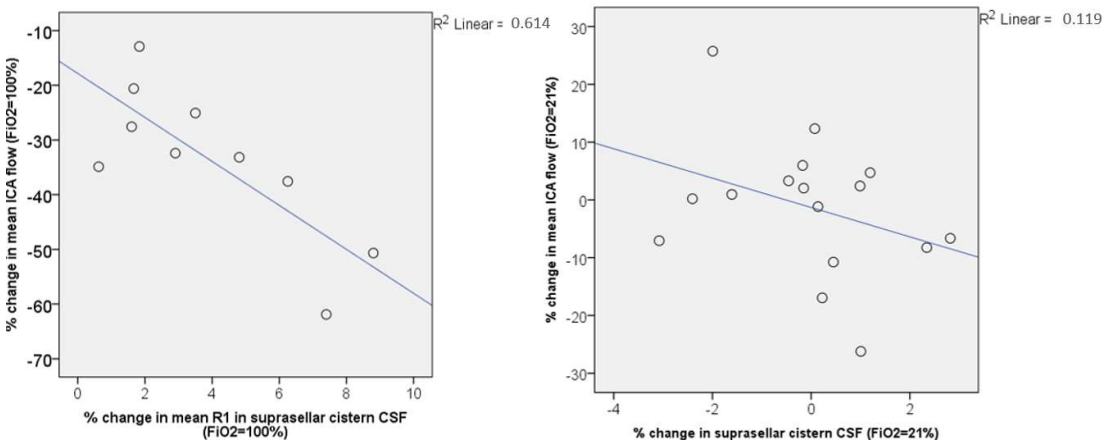

Figure 3.18 Correlation of %change in mean R1 in suprasellar cistern CSF and %change in ICA flow. Left: linear regression between %changes from baseline conditions (FiO_2 = 21%) in mean R1 in suprasellar cistern CSF and in total ICA flow in response to the administration of 100% FiO_2.
Right: linear regression between %changes from baseline conditions (FiO_2 = 21%) in mean R1 in suprasellar cistern CSF and %change in total ICA flow at a challenge FiO_2 of 21%.

Discussion

In the past few years there has been growing interest in the use of OE-MRI to assess regional hypoxaemia in a range of tumor types [62, 74, 136, 137]. In cerebral tumors, hypoxia is known to be a significant feature largely due to reduced cerebral blood flow reflecting increases in intracranial pressure [138]. Our group has previously shown that OE-MRI can produce T1 signal change in patients with GBM [62], however no systematic study of oxygen induced T1 changes in brain has been presented.

In this study, we have examined the effects of oxygen administration on T1 signal change in the brains of normal volunteers. Previous workers have shown that supra-physiological levels of FiO_2 can produce reductions in CBF of healthy volunteers [139-143]. Decrease of CBF of up to 30% have been reported in response to 100% O_2 producing decrease of oxygen delivery (DO_2) of over 25% [139]. In the current study, we measured combined internal carotid artery flow and demonstrated a 34% reduction

in total ICA flow in response to 100% FiO_2. Furthermore, significant decreases were observed also at lower levels of FiO_2 and there was a strong correlation between the percentage change in total ICA flow from baseline and FiO_2 levels (in our study, Pseudo R-Square = 0.938), in keeping with previous literature [144, 145]. Previous workers have shown that these decreases tend to be greater in childhood and young adults, reducing in early middle age ([139, 146]).

Previous studies have demonstrated very significant changes in suprasellar cistern CSF T1 values in response to increased FiO_2 [123, 147, 148]. Similar signal changes were not seen within the ventricles or in the CSF spaces over the vertex [123, 149, 150]. We have shown similar significant changes, with peak increases in R1 of over 4% in suprasellar cistern CSF in response to 100% FiO_2. Further similarity in the behaviour of suprasellar cistern CSF-R1 values and total ICA flow is seen when 100% oxygen administration is preceded by a lower supraphysiological concentration (FiO_2 = 60%). Both suprasellar cistern CSF-R1 and total ICA flow changes are larger under these circumstances than when 100% oxygen is preceded by air (increase in suprasellar cistern CSF-R1 = 7.46% *vs.* 3.49%; decrease in total ICA flow = -45.6% vs. -25.7%).

The physiological mechanism underlying hypoperfusion in response to hyperoxia is undefined. In hypoxia decreases in CBF mirror arterial oxygen content and show a semi-logarithmic relationship with PaO_2, which reflects the shape of the oxygen dissociation curve [139, 151]. The mechanism for this hypoxic response is a decrease in cerebral vascular resistance due to vasoconstriction in pial arteries [140, 151-153] . In significant hyperoxia in healthy subjects, haemoglobin is essentially saturated, having reached the flat part of the dissociation curve. Previous workers have speculated that the CBF response to hyperoxia is mediated by the concentration of dissolved oxygen (PaO_2) in arterial plasma [144], since this will continue to linearly

increase with FiO_2 after haemoglobin is saturated. The observation that the mean R1 change in the suprasellar cistern CSF is greater when 100% oxygen is preceded by 60% oxygen than when it is preceded by air is of particular interest. This suggests that the oxygen content within the CSF increases during administration of 60% and then continues to increase through administration of 100%. This would suggest a diffusion process from plasma to CSF that has not reached saturation during the standard 100% FiO_2 experiment. The fact that internal carotid flow shows the same response is illuminating. There is no physiological reason why pre-administration of 60% FiO_2 should result in a higher arterial plasma PaO_2 making it difficult to understand how plasma PaO_2 could be the physiological driver to decreased ICA flow. We propose the hypothesis that PaO_2 in CSF rather than in arterial blood drives decreases in CBF resulting from supraphysiological FiO_2. Clearly, although the findings of this study are suggestive, formal testing of this hypothesis is necessary. CSF PaO_2 is influenced by arterial oxygen tension and is normally expected to be higher than PaO_2 in the venous compartment draining neural tissue [154]. Of note, Kazemi *et al.* reported that CSF PaO_2 presents not uniform values across different locations of sampling and measurements are influenced by the PaO_2 of the neighbour neural tissue (specifically by the venous blood PaO_2) and proximity of the measurement location to the site of oxygen transfer from arterial blood to the CSF. Previous evidence of significant increase in CSF PaO_2 following 100% oxygen inhalation comes from a study by Zaharchuk *et al.* who demonstrated larger increases of PaO_2 in the basilar cisterns and cortical sulci of 155 ± 45 mmHg of and 124 ± 34 mmHg, respectively, and a linear relationship between R1 and oxygen content in CSF[147]. In addition, we expect that the magnitude of ICA flow change would be also influenced by the efficiency of PO_2 exchange between the CSF and vascular compartment. It is not clear whether the

dysmorphic anatomy of patients with brain tumors could alter this complex mechanism. As long as the exchange between CSF and vascular compartment is still maintained, despite the altered brain anatomy, with increasing tumor masses, the resulting higher intracranial pressure may compress CSF, augment the effect of CSF PaO_2 on neural tissue and diminish the effect of CSF PaO_2 on CBF measured in ICAs. The administration of 100% FiO_2 is therefore supposed to determine higher changes in R1 in normal GM and WM in patients with larger tumors (possibly causing intracranial pressure), up to a dimensional tumor threshold, after which the efficiency of PO_2 exchange between the CSF and neural tissue become lower.

In contrast to previously published findings in a variety of normal and tumor tissues [62, 74, 93, 155, 156], we saw significant changes in R1 in GM but not in WM in response to 100% FiO_2. Different factors may have determined the discrepancy with previous literature. First, differences may derive from different sensibility of R1 to oxygen challenges in animal models, investigated by most studies in literature, and humans. Wu et al. documented significant change in both GM and WM in a rodent model of glioma [93]; in the only existing study investigating OE-MRI in patients with high-grade glioma R1 change in normal brain tissues was not reported [62]. Second, although we tried to check and manually edited the masks, inclusion of pixels containing non-WM tissue in the VOIs may have occurred. A third source of variability may arise from different characteristics of the scanners used in the studies. In our opinion, in light of the decreases in overall CBF observed at high FiO_2, our results are not totally surprising. Cerebral autoregulation is designed to maintain regional PaO_2 within the brain tissue at a constant level [157] and these results suggest that that mechanism is active in supraphysiological hyperoxic states as well as the physiological state of hypoxia. Clearly, this has impact for future studies investigating

hypoxia in cerebral tumors using oxygen challenges with measurement of T1 change. The identification of hypoxia within the tissue requires the presence of perfusion and the absence of signal response to high FiO_2 concentrations. If this autoregulatory mechanism is in place then the oxygen challenge will reduce CBF to the normal tissues and possibly to the tumor. This could lead to inappropriate characterisation of tumor tissue with false positive classification of tissue as hypoxic. Indeed, in the current study GM and WM would both have been classified as hypoxic with current recommended analysis techniques [122].

In applying oxygen challenge imaging to patients with cerebral tumors it is therefore essential to ensure that oxygen has reached the cerebral circulation and that DO_2 has not resulted in autoregulatory decreases of CBF. Patients with cerebral tumors may be unwell, elderly or frail. Previous works have shown that administration of oxygen via a simple facemask or a "Hudson" facemask with a small reservoir bag can lead to suboptimal oxygen administration due to inadequate peak flow and entrainment of room air [125]. However, elderly or infirm patients may poorly tolerate the use of the mouthpiece or formal anaesthetic mask. We would therefore recommend that measurement of oxygen induced changes in suprasellar cistern CSF-R1 values should be routinely performed to confirm that oxygen has been successfully administered. In the current study, significant change (1.40%) in the suprasellar cistern identified that pure oxygen rather than lower FiO_2 had been administered with a sensitivity of 69.44% and a specificity of and 93.33%; furthermore the same threshold distinguished administration of 100% FiO_2 from air with excellent accuracy (sensitivity = 93.3% and specificity = 81%).

As stated above, the presence of a physiological autoregulatory decrease in cerebral blood flow in response to high levels of inspired oxygen would significantly affect and

potentially invalidate identification of hypoxia in cerebral tumors. This physiological response to hyperoxia is not well understood and it is likely that, in the presence of cerebral tumor, the response may be absent. In the study of Linnik *et al.* significant signal changes were seen within tumor tissue in response to high FiO_2 although normal tissue values were not presented [62]. In order to confirm that a significant physiological reduction in CBF has not occurred we would recommend routine performance of PCA measurements in the major cerebral arteries before and during oxygen administration. Measurement of R1 change in normal GM and WM would also be of value and should be performed.

Conclusions

In conclusion, administration of high concentrations of inspired oxygen results in significant decreases in CBF in young normal subjects. Measurement of R1 in suprasellar CSF and GM shows significant increases at a FiO_2 of 100%. Prior exposure to supraphysiological FiO_2 before the oxygen challenge experiment results in larger decreases in cerebral blood flow and larger increases in suprasellar cistern CSF-R1. This behaviour suggests that CSF PaO_2 may be a physiological driver for the reduction in CBF. WM shows no significant changes in response to high FiO_2 which we attribute to a constant local tissue oxygen delivery due to a combination of increased oxygen carriage and decreased CBF. We recommend that studies using oxygen challenge in patients with cerebral tumors should confirm oxygen delivery by measurement of signal change in the basal CSF and should characterise the status of the autoregulatory response by measurement of major arterial flow before and during oxygen administration and by documentation of signal change in normal GM and WM.

Chapter 4 Time Course and Reproducibility of R1 in Brain and Tumor Regions of Patients with High-grade Gliomas

This chapter describes a prospective MRI study. This research material has not yet been submitted for publication but has been presented in the alternative thesis format.

The study design was by Prof Jackson, Dr. Coope and the candidate. Ethical application was by Professor Jackson. Patients were recruited at the Salford Royal NHS Foundation Trust and research MRI studies were carried out at the Wolfson Molecular Imaging Centre.

The candidate has been involved with the recruitment, data acquisition, data processing, image analysis and statistical analysis. MRI sequence development was by Dr Morris. Interpretation of the results was carried out by Prof Jackson, Dr. Coope and the candidate. Literature review was by the candidate and Prof. Jackson.

Dr Coope has also been involved in the development of the analytical techniques.

The candidate gave his contribution in writing the first draft of the manuscript. Prof Jackson helped in the revision of the manuscript. All authors have provided input into helpful discussions. This study was jointly funded by Cancer Research UK and the Engineering and Physical Sciences Research Council (Grant reference C8742/A 18097).

Abstract

Background: Tumor hypoxia represents a crucial factor in determining the invasiveness of GBM. Previous studies have demonstrated the feasibility of measuring R1 change in brain tumors in response to 100% oxygen by means of OE-MRI. The main aim of this study was to document the magnitude, timing and distribution of R1 changes in brain tumors (enhancing and non-enhancing regions) and in normal brain in response to a FiO_2 of 100% in patients with high-grade glioma and to evaluate the reproducibility of the measurements.

Methods: 12 patients were connected through a mouthpiece to a modified "Mapleson A" semi-open anaesthetic circuit and underwent two whole-brain OE-MRI scans (visit

1 and 2) in the same day being exposed in sequence to a FiO_2 of 21%, 100% and back to 21%. Capnography traces of O_2 and CO_2 were monitored to assess satisfactory O_2 delivery and proper connection between the mouthpiece and patient mouth. Percentage change of mean R1 (from baseline level) at 100% FiO_2 and at return to 21% FiO_2 was calculated for tumor regions (enhancing = EN and non-enhancing = NE) and the different brain tissue components: whole cerebrospinal fluid (CSF), grey matter (GM), white matter (WM) and, in addition, in the suprasellar cistern CSF. Significance of %change of mean R1 was assessed using a 2-tailed one sample t-test ($p \leq 0.05$). Reproducibility of change between visit 1 and 2 was evaluated by means of 2-tailed independent samples t-test. Reproducibility of the different segments of the R1 mean time course (ascending portion, 100% O_2 portion and descending segment) for the two visits was assessed calculating coefficients of correlation.

Results: Significant %change in mean R1 was measured under the administration of 100% FiO_2 in brain (suprasellar cistern CSF = 4.82%, whole CSF = 1.39%, GM = 0.63% and WM = 0.26%) and tumor regions (EN = 2.31%, NE = 1.42%) of patients with satisfactory gas delivery; no significant change was detected in patients with unsatisfactory gas delivery. No significant difference of mean R1 change in response to a FiO_2 of 100% was detected in normal brain and tumor regions when comparing visit 1 and 2. Overall, the time courses of mean R1 change in brain and tumor regions appeared reproducible.

Conclusions: Mean R1 in brain and tumor regions shows significant increases at a FiO_2 of 100%. Therefore, mean R1 change may be used as a metric in clinical trials involving patients with brain tumors undergoing OE-MRI, ensuring that participants are receiving proper O_2 delivery.

Introduction

Tumor hypoxia is one of the main histological hallmarks of high-grade gliomas although it appears to vary between patients and shows significant variations within individual tumors [22]. Tumor hypoxia represents a crucial factor in determining the invasiveness of GBM, and has been associated with amplified resistance to radiotherapy, chemotherapy and with worse outcome after standard of care therapy [22, 52]. The relationship between tissue hypoxia, treatment resistance and decreased survival has raised the possibility of improving outcome by targeting novel therapeutic approaches to the hypoxic component of the tumor. This may be addressed by the use of hypoxia reversal strategies in combination with conventional chemo-radiotherapy or by the use of novel cytoreductive agents that are specifically taken up by, and toxic to, hypoxic cells [52].

The presence of significant tissue heterogeneity within individual tumors, together with the need to target hypoxic areas using surgery or radiotherapy, has led to increasing demands for effective imaging biomarkers of tissue hypoxia [33]. Although a number of MRI-based methods have been applied to the study of tumor hypoxia, none has proven satisfactory.

OE-MRI employs a hyperoxic challenge. The patient, lying in the MR scanner, inhales 100% oxygen via a face mask or non-rebreathing circuit. Molecular oxygen acts as a contrast agent increasing the longitudinal relaxation rate (R1) of water [74, 158]. Changes in R1, due to hyperoxic breathing, are thought to be proportional to changes in tissue oxygen concentration, and allow identification of hypoxic tissue Initial pre-clinical and small-scale clinical studies have shown considerable promise for this technique. Pioneer studies have demonstrated the feasibility of visualizing tumor hypoxia in brain tumors [62, 159, 160]. Ongoing preclinical validation studies

(unpublished observations) continue to show close agreement between tissue hypoxia and OE-MRI signal change. At the present time, this represents the most promising method for clinical imaging of regional tissue hypoxia although there is a clear need for extensive biological validation before it can be applied in clinical studies. Furthermore, to date, no trial has ever validated the reproducibility of OE-MRI in patients with high-grade gliomas

The aim of the study was to develop optimized acquisition and analysis strategies for the use of OE-MRI in high-grade gliomas. Specifically the study aimed to evaluate the magnitude, timing, distribution and reproducibility of R1 changes, in response to the administration of 100% FiO2, in normal [grey matter (GM), white matter (WM), CSF] and tumor tissues of patients affected by high-grade gliomas. In addition, we assessed also these features in the suprasellar cistern CSF, to validate the findings reported by our group in a cohort of normal volunteers (chapter 3) and demonstrate the possibility of clinical translation.

Methods

1. Patients

The patient group was composed of twelve patients with high-grade gliomas (suspected on the basis of a clinical MRI) recruited through the Neuro-oncology multidisciplinary team (MDT) at Salford Royal NHS Foundation Trust (SRFT). Inclusion criteria involved the presence of a brain lesion radiological compatible with a newly diagnosed glioblastoma and/or recurrent grade 3 glioma with secondary resection planned, age > 18 years, capability to receive and understand verbal and written information regarding the study and give written informed consent, ability to lie still for two one-hour scanning sessions. Participants to the study were asked to sign

a consent form after reading patient information sheet and adequate time to ask questions or additional information.

Patients with contraindications to MRI scanning (e.g. pacemaker, heart valve replacement, metal implants not approved for MRI, neurostimulators, claustrophobia), history of contrast (gadolinium) or radiotracer allergy, Karnofsky Performance Score < 60 were not enrolled into the study.

Patients underwent two consecutive OE-MRI experiments at our institution on the same day, separated by 2-4 hours from each other, with a break of a minimum of 90 minutes between the oxygen challenges. Each OE-MRI visit had an approximate duration of one hour. The patients were connected to a modified "Mapleson A" semi-open anaesthetic circuit implemented in the scan, as for the normal volunteers (see chapter 3).

2. OE-MRI protocol and analysis, oxygen delivery gas sampling unit system

A modified Mapleson anaestheric gas delivery circuit (as described in chapter 3) was used to administer different level of molecular oxygen (21% and 100%) through a mouthpiece at a rate of 15 litres/min throughout the imaging protocol. A nasal clip was also provided to prevent respiration of the environment air through the noose. The O_2 and CO_2 levels within the system were constantly monitored displaying the corresponding traces on a computer receiving data from a commercial gas sampling unit (ML206 Gas Analyser and Powerlab 8/35; ADInstruments, Oxford, UK) and analysed (Labchart v. 7.3.4, ADInstruments, Oxford, UK). The O_2 trace was assessed to ascertain the O_2 level within the circuit, whereas the satisfactory sealing of the mouthpiece was assessed monitoring the characteristic alternating pattern of CO_2. **Fig. 4.1** shows examples of O_2 and CO_2 capnography traces displayed by the Labchart system reflecting satisfactory and unsatisfactory O_2 delivery and proper connection

between the mouthpiece and patient mouth.

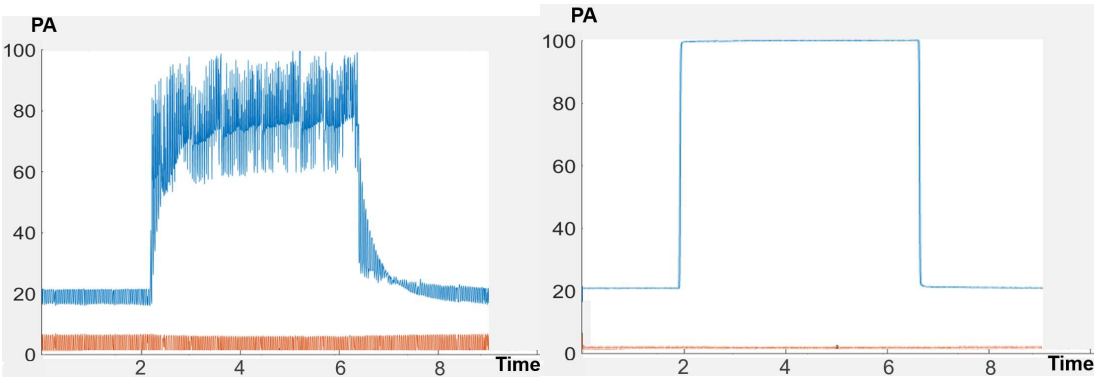

Figure 4.1 Representative capnographic traces of satisfactory and unsatisfactory gas delivery. Left: satisfactory gas delivery in a patient undergoing the OE-MRI protocol; note the waveform trace of CO_2 (red) and the rise of PO_2 (blue). Right: capnographic traces evidencing failed sealing between mouthpiece and mouth; note the shape of the rise of PO_2 and CO_2 trace developing as at a lower level than satisfactory gas delivery. Time is expressed in minutes.

The MRI experiments was carried on a 1.5 T Achieva scanner (Philips Healthcare, Eindhoven, The Netherlands) using a using an eight-channel SENSE head coil.

In the first MRI experiment, the MRI protocol included

1) Survey acquisitions on three planes *(*TE: 5 ms, TR:15 ms, α: 20°, FOV: 250x250 mm, matrix: 256x256; imaging duration: 2 min);

2) T1-w axial structure SENSE acquisition (TE: 4ms, TR 9 ms, α: 8°, FOV 230x230, matrix: 256x256, voxel size: 1.8x1.8x2.5 mm; imaging duration: 7 min);

3) three selective high resolution variable flip angle (VFA) whole brain maps (α = 3°, 13° and 18°, TE: 1 ms, TR: 12 ms, matrix: 128x128, FOV 230x230 mm, voxel size: 1.8x1.8x5 mm; imaging duration: 58 sec);

4) A VFA dynamic sequence comprising 70 frames (frame duration = 8 sec), lasting in total approximately 9.30 min (TE: 1ms, TR: 12ms, matrix: 128x128, FOV: 230x230 mm, voxel size: 1.8x1.8x5 mm). The first 15 frames were acquired were acquired under the administration of a baseline FiO_2 of 21%.

frames 16-50 under of FiO_2 of 100% and the remaining frames (51-70) under a FiO_2 of 21%. Patients were therefore systematically exposed to the 21%/100% and again 21% FiO_2.

The second MRI experiment included the same sequences and in addition:

1) Survey sequences (acquired with the same parameters as for the first MRI experiment);
2) T1-w axial high-resolution acquisition (TE: 4ms, TR 9 ms, α: 8°, FOV: 240x240, matrix: 256x256, voxel size: 1.25x1.25x1.25 mm; imaging duration: 8.30 min);
3) Four T_1-FFE spoiled gradient echo sequences with different flip angles (2°, 8°, 15°, 20°) for calculation of baseline T_1 maps (TR 2.6 ms, TE 1 ms, FOV:240x240, matrix: 128x128; voxel size: 1.8x1.8x2.5 mm);
4) Dynamic contrast enhanced acquisition with identical acquisition parameters and a temporal resolution of 3.4 sec. Gadolinium-based contrast agent (Gd-DTPA-BMA; Omniscan, GE Healthcare, Oslo, Norway) was injected using a pressure injector as a bolus of 3ml, at a rate of 15 mls^{-1} and dose of 0.1 $mmolkg^{-1}$ of body weight after acquisition of the fifth image volume. This was followed by a saline flush;
5) T1-w axial post-contrast acquisition (TE: 4ms, TR 500 ms, α: 8°, FOV: 240x240, matrix: 256x256, voxel size: 1.25x1.25x1.25 mm; imaging duration: 8 min).

Additional imaging sequences were also acquired for other research projects running at our institute. 2D phase contrast angiography (PCA) surveys and quantitative flow (QF) measurement could not be performed because the sequences would had prolonged the MRI protocol duration and diminished patient compliance.

3. Data processing and analysis

a. Motion correction of the VFA data

For each individual scan, motion correction was performed after merging the baseline VFA maps (voxel size: 1.8x1.8x5 mm, 3 frames x 3 repetitions = 9 images) and the 70-frames of each VFA dynamic sequences together, using the mean volume of the concatenated sequence as reference volume for the registration. All these processing steps were performed using FSL (FMRIB Software Library v 5.0).

b. Generation of R1 values and maps

R1 values were calculated from the concatenated motion corrected variable flip angle dynamic series using an in-house R script (R-Project, Levallois Perret, France; library: www.dcemri.com).

c. Tissue-type segmentation and definition of volumes of interest for the R1 maps

Definition of volumes of interest encompassing the tumor was performed manually on Analyze v. 11.0 (AnalyzeDirect, Overland Park, KS) reviewing all the slices of the brain MRI post-contrast images on the axial plane and delineating: 1) a region including the enhancing part of the tumor, 2) the non-enhancing component of the tumor (**Fig. 4.2**).

As for normal volunteers (chapter 3), a spherical VOI (radius: 10 mm), encompassing the suprasellar cistern CSF, was generated in fslmaths (FMRIB Software Library v5.0) defining the centre of the suprasellar cistern on the mean volume of the concatenated VFA datasets (VFA maps + VFA baseline dynamic sequence + VFA dynamic sequences acquired under different FiO_2).

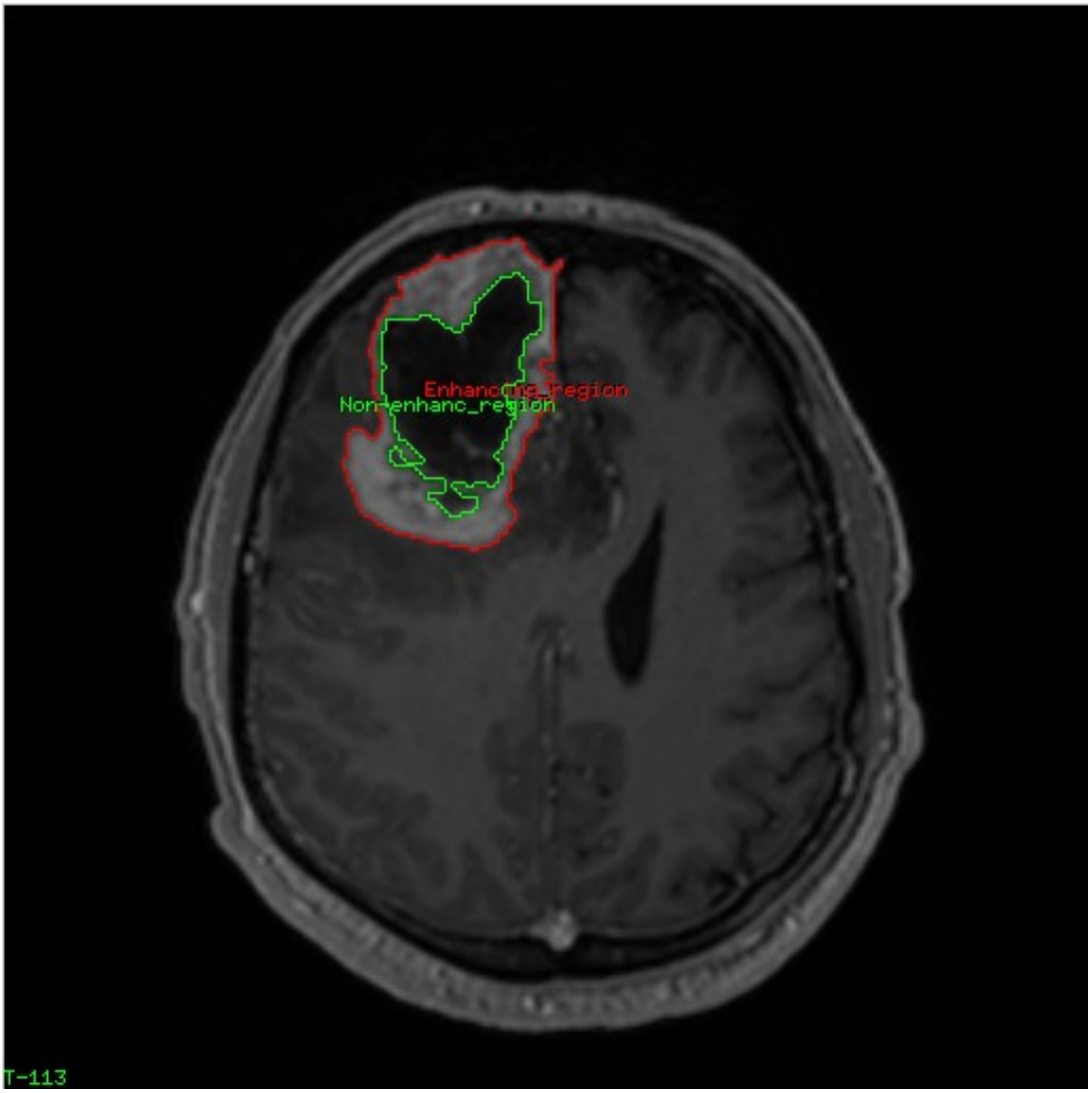

Figure 4.2 Segmentation of enhancing and non-enhancing tumor region on high-resolution post-contrast MRI images. Green = non-enhancing region; red = enhancing region.

The spherical VOI was generated to evaluate whether a specific %change in mean R1 (1.40%), identified in the cohort of normal volunteers described in chapter 3, could be used as cut-off in the clinical scenario to predict the satisfactory delivery of 100% O_2 using the gas traces as reference for validation.

Volumes of interest (VOI) representing GM, WM and CSF were defined on the T1-weighted axial images after segmenting the brain from the skull using BET (Brain Extraction Tool) implemented in FSL [126], using as default parameters a fractional intensity threshold (f) of 0.4 and a threshold gradient (g) of 0.2, based on previous

literature and local experiments [129]. Due to the altered anatomy of brain in patients, the extracted brain and brain mask were visually checked for each scan and eventually reprocessed modifying the f and g parameters. Before generating masks for GM, WM and CSF, the tumor masks were subtracted from the brain mask. The high resolution T1-weighted images of each individual MRI scan were automatically segmented using FAST (FSL, FMRIB Software Library v 5.0) to obtain the normal tissue masks (GM, WM and CSF masks), which were systematically visually checked and manually edited using Analyze 11.0 (AnalyzeDirect, Overland Park, KS).

The tumor masks and normal tissue masks were subsequently registered to the low-resolution space of the VFA dynamic sequences, to match the spatial resolution of the R1 maps. The masks were then re-sliced using the mean volume of the motion-corrected concatenated VFA dynamic sequence as a reference.

d. Measurement of R1 change

For each FiO_2 level (baseline 21%FiO_2, 100% FiO_2 and 21%FiO_2), R1 was sampled from every scan using the defined VOIs and tissue masks. Data beyond 3 standard deviations from the mean were excluded to remove outliers. The mean R1 baseline value was obtained by averaging values from frames acquired breathing air (11 frames, n = 5-15); the initial 4 frames were excluded from the calculation due to image noise. The mean experimental R1 value for each FiO_2 challenge (100% and 21%) was calculated from the last 11 frames (frames 40-50 for 100% FiO_2 and frames 60-70 for 21% FiO_2) acquired during oxygen administration (**Fig. 4.3**). The choice of selecting the same number of frames (n = 11) for baseline and challenge sequences was taken to minizing the risk of violating the assumption of independent samples t-Test [161].

Finally, the %change in mean R1 was calculated as:

$$\%\text{change in mean R1} = \frac{\text{mean R1(challenge)} - \text{mean R(baseline)}}{\text{mean R1(baseline)}} * 100.$$

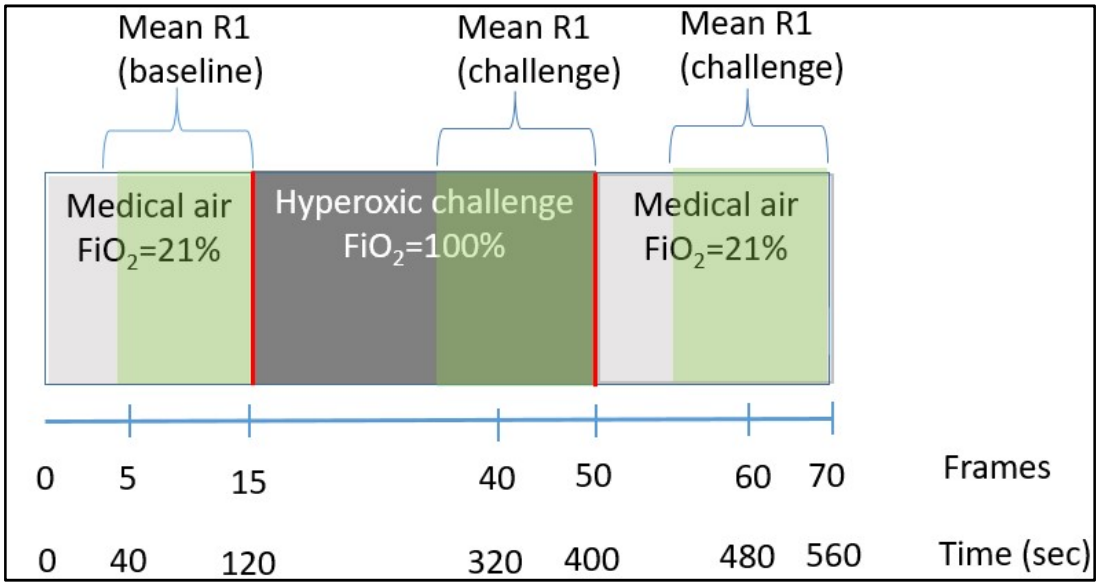

Figure 4.3 Scheme of the OE-MRI protocol

e. Reproducibility of changes

The time course of R1 change in suprasellar cistern CSF, whole CSF, GM and WM and tumor regions were represented by line plots. Frames were also binned (1 bin = 3 frames; duration = 24 sec: 8 sec x 3; number of bines acquired under 100% FiO_2 = 11) in separate plots. The choice of merging 3 frames in 1 bin was made in order to obtain a bin duration similar to those obtained in previous experiment in volunteers (40s in healthy volunteers, chapter 3) and not reduce excessively the number of measurements (n. bins at baseline = 5, n bins at 100% FiO_2 = 11, n. bins at 21% FiO_2 = 7). An upper boundary consisting of the baseline mean R1 + 1 standard deviation was established as a threshold for significant signal change. The histogram bins in which 1) the threshold was exceeded; 2) peak signal change was reached and 3) signal fell below the threshold following return to medical air were recorded.

Reproducibility of the signal change time course was assessed using repeated scans with satisfactory oxygen delivery according to the gas traces. In these subjects, %change in mean R1 visit 1 and 2, in response to 100%FiO_2, were compared by means of 2-tailed independent samples t-test. (p = 0.05). The reproducibility of the histogram

bins in which: 1) peak signal change was reached and 2) signal fell below the threshold following return to medical air was examined. The reproducibility of the ascending (FiO_2 switched from 21% to 100%) and descending (FiO_2 switched from 100% to 21%) parts of the R1 time course curve were compared by measurement of the coefficient of determination: $r = \frac{1}{n}\sum \frac{(x_{exp}-\overline{x_{exp}})\cdot(x_{mod}-\overline{x_{mod}})}{s_{exp}\cdot s_{mod}}$.

A further analysis was carried out for each individual undergoing OE-MRI twice to assess the equality of the binned R1 time curves in the two experiements under a 100% FiO_2. Therefore, it was investigated the null hypothesis that the slopes were identical (parallel) considering significant differences only for p values < 0.05.

4. Statistics

Most of statistics were performed in IBM SPSS v.22 (IBM Corp. Released 2013. IBM SPSS Statistics for Windows, Version 22.0. Armonk, NY: IBM Corp.); GraphPad Prism version 7.04 (GraphPad Software, La Jolla California USA, www.graphpad.com) was used exclusively to compare the segments of the mean R1 dynamic course acquired 100% FiO_2 [132]. Normality of data distributions was evaluated examining the normal quantile-quantile (Q-Q) plots. The mean R1 measured during the administration of 100%FiO_2, was compared to the mean R1 calculated under the baseline 21% FiO_2; the comparisons were performed for suprasellar cistern CSF, whole CSF, GM, WM and tumor lesions (enhancing and non-enhancing regions), using the methods explained in chapter 3 for healthy volunteers.

The reproducibility of the dynamic curves was assessed applying the same methods used for healthy volunteers (see chapter 3).

The hypotheses tested were that:

1) exposure to 100% FiO_2 produces significant changes in mean R1 in suprasellar CSF, whole CSF, GM and in WM of patients with satisfactory oxygen delivery;

2) in patients with satisfactory oxygen delivery, exposure to 100%FiO_2 produces higher changes in suprasellar CSF, whole CSF, GM, in WM compared to return to 21 FiO_2 following 100%FiO_2;

3) a %change in mean R1 > 1.40 in suprasellar cistern CSF, in response to the administration of 100% FiO_2, can predict the satisfactory delivery of oxygen;

4) in patients with satisfactory administration of 100% FiO_2 the %change in mean R1 in the enhancing region of the tumor is significantly higher than in the non-enhancing region;

5) the significant changes in mean R1 in both normal and tumor tissue are reproducible.

Results

Initially, thirteen patients were recruited. Eleven out of the 13 scanned patients gave a positive feedback to the scanning protocol; only one patient did not tolerate the entire imaging protocol and was excluded from the study. Eleven out of 12 patients were grade IV glioma at the histology examination: 10 classical GBM (one multifocal tumor) and 1 gliosarcoma (GSM); a patient turned out to have a grade III glioma (anaplastic oligodendroglioma - AOD). Unfortunately 5 scans in 3 patients (patient 4 – visit 1, patient 9 – visits 1 and 2, patient 11 – visits 1 and 2), as also confirmed by the capnography traces, were affected by difficulty in holding the mouthpiece and unsatisfactory O_2 delivery. Out of these 3 patients, one patient was female (patient n. 9) and complained about the size of the mouthpiece and the other two patients had dentures.

Patient demographic data and capnography information are illustrated in **Table 4.1**.

Pt n.	Age (y)	Sex	Histology	Tumor Location	Total tumor volume (cm^3)	EN region (volume, cm^3)	NE region (volume, cm^3)	Normal trace visit 1	Normal trace visit 2
1	56	F	GBM	Left temporo-occipital	47.87	35.29	12.58	yes	Yes
2	52	M	* AOD	Right frontal	184.39	124.65	59.74	yes	Yes
3	53	F	GBM multifocal	Left occipital	43.57	29.77	13.8	yes	Yes
4	60	M	* GSM	Right temporal	58.69	30.4	28.29	**no**	yes
5	58	M	GBM	Right frontal	89.82	52.86	36.96	yes	yes
6	67	F	GBM	Left temporal	12.93	8.1	4.83	yes	yes
7	66	M	GBM	Left frontal	100.52	52.13	48.39	yes	yes
8	68	F	GBM	Left parietal	10.85	7.91	2.94	yes	yes
9	64	F	GBM	Right frontoparietal	5.47	5.16	0.31	**no**	**no**
10	38	M	GBM	Right parietal	57.96	38.79	19.17	yes	yes
11	77	M	GBM	Right parietal	100.97	54.22	46.75	**no**	**no**
12	70	F	GBM	Left frontal	15.73	11.97	3.76	yes	yes

Table 4.1 Patient characteristics and capnography information. "Normal trace" indicates an expected physiological O_2 and CO_2 traces, displayed on the computer connected to the gas analysis system. Pt. = patient, n. = number, Y = years, EN = enhancing, NE = non-enhancing; AOD = Anaplastic oligodendroglioma; GSM = gliosarcoma.

1) The effect of 100% FiO_2 on mean R1 of normal tissue (WM, GM, whole CSF and suprasellar cistern CSF)

All patient scans with satisfactory capnography data, under the administration of 100% FiO_2, showed significant positive %change of mean R1 from baseline (FiO_2 = 21%) in all normal tissue types ($p < 0.001$). The region with the highest %change in mean R1 resulted the suprasellar cistern CSF, followed by the whole CSF, GM and WM (**Table 4.2**).

	Average mean R1 at baseline FiO_2	Average mean R1 at 100% FiO_2	Average mean R1 at 21% FiO_2	%change in mean R1 (FiO_2 = 100%)	St. dev of %change	Lower CI (95%) of %change	Upper CI (95%) of %change	Sig. of %change
WM	1.192	1.195	1.193	0.266	0.225	0.107	0.324	**< 0.001**
GM	0.918	0.924	0.919	0.626	0.224	0.468	0.684	**< 0.001**
CSF	0.885	0.896	0.884	1.392	0.818	0.947	1.737	**< 0.001**
Suprasellar cistern CSF	0.647	0.679	0.654	4.822	1.750	3.928	5.615	**< 0.001**

Table 4.2 Significance of %change in mean R1 in WM, GM, whole CSF and suprasellar cistern CSF. Significance of %change in mean R1 in WM, GM, whole CSF and suprasellar cistern CSF from baseline mean R1 (FiO_2 = 21%), in response to administration of 100% FiO_2, in patient scans (n = 19) with satisfactory gas delivery (one sample 2-tailed t-test).

Analysis of individual p values in these patient scans revealed significance of change in most cases for suprasellar cistern CSF (18/19), whole CSF (17/19) and GM (18/19) but only in 4 cases for WM (**Table 4.3** and **4.4**). Patient 7 - visit 2 did not presented significant individual p value of change in CSF; patient 4 visit 2 demonstrated not significant individual p value of change in all tissue types (the same subject in visit 1 proved to have unsatisfactory gas delivery in visit 1 on the basis of the capnography). Conversely, no significant change in response to the hyperoxic challenge was detected in patient scans with unsatisfactory gas delivery in all tissue types (**Table 4.5**). The highest pair of %change of mean R1 in suprasellar cistern CSF was measured in visit 1 and 2 of patient n. 2 (AOD). The only scan with no significant p value of change in suprasellar cistern CSF was patient 4 (visit 2) who had a different histology (GSM) compared to the other patients.

Patient scan	FiO_2	%change in mean R1	p value of %change	FiO_2	%change in mean R1	p value of %change
Patient 1 visit_1	100	5.637	**0.02**	21	-1.344	0.101
Patient 1 visit_2	100	8.178	**0.01**	21	3.565	**0.027**
Patient 2 visit_1	100	6.071	**0.01**	21	0.626	0.603
Patient 2 visit_2	100	8.210	**< 0.0001**	21	0.621	0.598
Patient 3 visit_1	100	3.574	**0.004**	21	-0.917	0.248
Patient 3 visit_2	100	3.291	**< 0.0001**	21	0.212	0.780
Patient 4 visit_2	100	5.712	0.074	21	3.600	0.084
Patient 5 visit_1	100	3.726	**< 0.0001**	21	-0.082	0.900
Patient 5 visit_2	100	3.820	**0.01**	21	1.094	0.240
Patient 6 visit_1	100	5.660	**< 0.0001**	21	1.873	**0.020**
Patient 6 visit_2	100	4.463	**< 0.0001**	21	0.529	0.404
Patient 7 visit_1	100	4.942	**< 0.0001**	21	2.068	**0.046**
Patient 7 visit_2	100	2.823	**0.004**	21	-0.870	0.190
Patient 8 visit_1	100	4.603	**< 0.0001**	21	2.232	**0.019**
Patient 8 visit_2	100	2.418	**0.003**	21	-0.041	0.947
Patient 10 visit_1	100	3.436	**< 0.0001**	21	0.585	0.313
Patient 10 visit_2	100	2.524	**0.002**	21	1.358	0.190
Patient 12 visit_1	100	5.479	**< 0.0001**	21	1.185	0.204
Patient 12 visit_2	100	7.044	**< 0.0001**	21	0.430	0.563

Table 4.3 Patients with satisfactory oxygen delivery: individual percentage changes in mean R1 in suprasellar cistern CSF. Patients with satisfactory oxygen delivery: individual percentage changes in mean R1 in suprasellar cistern CSF (from individual baseline average mean R1) at different FiO_2 and corresponding p values (significant values are in bold), assessed by 2-tailed independent samples t-test.

Patient scan	FiO_2 = 100%					
	%change in mean R1 in WM	p value of %change	%change in mean R1 in GM	p value of %change	%change in mean R1 in CSF	p value of %change
Patient 1 visit_1	0.003	0.98	0.392	**0.038**	1.277	**0.002**
Patient 1 visit_2	0.593	**0.019**	0.790	**0.005**	1.744	**< 0.0001**
Patient 2 visit_1	0.570	**0.042**	0.817	**0.002**	0.801	**0.017**
Patient 2 visit_2	0.256	0.18	0.515	**0.015**	0.986	**0.017**
Patient 3 visit_1	0.550	**0.014**	0.828	**< 0.0001**	0.955	**0.001**
Patient 3 visit_2	0.070	0.62	0.441	**0.001**	1.038	**< 0.0001**
Patient 4 visit_2	-0.180	0.146	0.234	0.081	0.275	0.070
Patient 5 visit_1	0.468	**0.016**	0.738	**< 0.0001**	0.666	**0.003**
Patient 5 visit_2	0.266	0.06	0.403	**0.006**	0.543	**0.001**
Patient 6 visit_1	0.083	0.427	0.522	**< 0.0001**	1.919	**< 0.0001**
Patient 6 visit_2	0.033	0.733	0.509	**< 0.0001**	2.074	**< 0.0001**
Patient 7 visit_1	0.187	0.494	0.642	**0.006**	1.423	**< 0.0001**
Patient 7 visit_2	0.191	0.208	0.356	**0.013**	0.116	0.571
Patient 8 visit_1	0.314	0.078	0.991	**< 0.0001**	3.041	**< 0.0001**
Patient 8 visit_2	0.179	0.58	0.813	**0.008**	2.822	**< 0.0001**
Patient 10 visit_1	0.294	0.18	0.364	**0.043**	0.936	**< 0.0001**
Patient 10 visit_2	0.674	0.023	0.894	**0.003**	1.557	**< 0.0001**
Patient 12 visit_1	0.321	0.059	0.848	**< 0.0001**	1.921	**< 0.0001**
Patient 12 visit_2	0.175	0.16	0.795	**< 0.0001**	2.362	**< 0.0001**

Table 4.4 Patients with satisfactory oxygen delivery: individual percentage changes in mean R1 in whole WM, GM and whole CSF. Patients with satisfactory oxygen delivery: individual percentage changes in mean R1 in whole WM, GM and whole CSF (from individual baseline average mean R1) at different FiO_2 and corresponding p values (significant values are in bold), assessed by 2-tailed independent samples t-test.

	Average mean R1 at baseline FiO_2	Average mean R1 at 100% FiO_2	Average mean R1 at 21% FiO_2	%change in mean R1 (FiO_2 = 100%)	St. dev of %change	Lower CI (95%) of %change	Upper CI (95%) of %change	Sig. of %change (FiO_2 = 100%)
WM	1.128	1.127	1.127	-0.087	0.409	-0.645	0.370	0.495
GM	0.895	0.894	0.895	-0.086	0.650	-0.942	0.671	0.665
CSF	0.826	0.823	0.820	-0.165	1.285	-1.810	1.380	0.727
Suprasellar cistern CSF	0.757	0.750	0.757	-0.400	3.042	-4.227	3.327	0.757

Table 4.5 Significance of %change in mean R1 in WM, GM, whole CSF and suprasellar cistern CSF from baseline mean R1 (FiO_2 = 21%), in response to administration of a FiO_2 of 100%, in patient scans with unsatisfactory gas delivery (one sample 2-tailed t-test).

Patients with satisfactory oxygen delivery demonstrated significantly higher percentage change of mean R1 in suprasellar cistern CSF (4.821% *vs.* -0.400%, p = 0.00004), whole CSF (1.392% *vs.* -0.165% p = 0.003) and WM (0.266% *vs*. -0.086%, p = 0.016) compared to patients with unsatisfactory gas delivery. Percentage change of mean R1 in GM was nearly significantly higher (0.626% *vs.* -0.086%; p = 0.07) in case of good satisfactory O_2 delivery compared to unsatisfactory delivery (**Fig. 4.4**, **Table 4.6**).

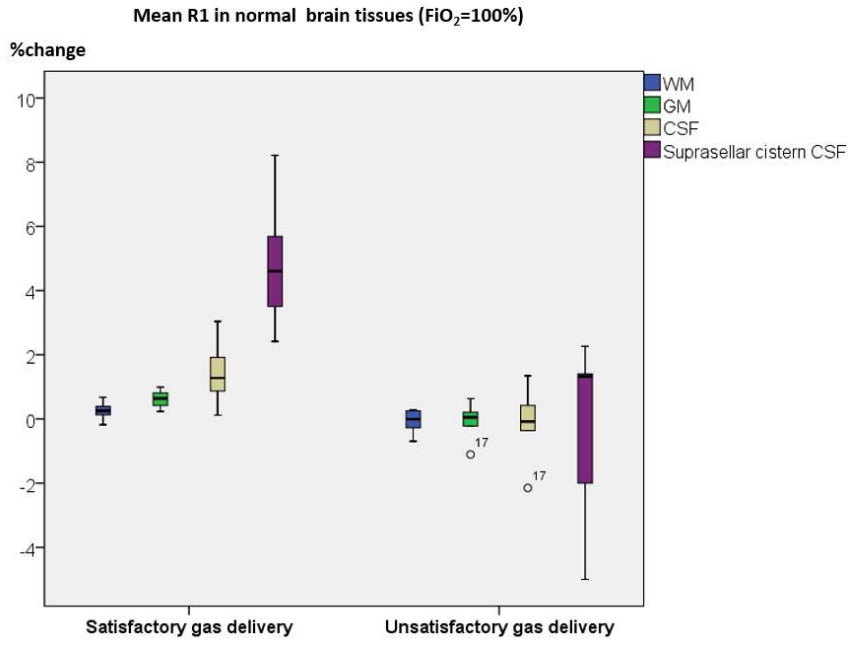

Figure 4.4 Box plot comparing %changes in mean R1 from to baseline mean R1, determined by the administration of a FiO_2 of 100%, in patients with satisfactory and unsatisfactory O_2 delivery (WM, GM, whole CSF and suprasellar cistern CSF).

	Levene's t test for Equality of Variance		Independent Samples t-test
	F	Sig.	Sig. (2-tailed)
WM	3.649	0.69	**0.016**
GM	7.854	0.01	0.07
CSF	0.574	0.427	**0.003**
Suprasellar cistern CSF	4.227	0.082	**0.00004**

Table 4.6 Comparison of %changes in mean R1 in WM, GM, whole CSF and suprasellar cistern CSF from baseline mean R1 (FiO_2 = 21%), in response to administration of a FiO_2 of 100%, in OE-MRI experiments with satisfactory (n = 19) and unsatisfactory (n = 5) O_2 delivery.

In addition, in patients with satisfactory oxygen delivery significant differences in R1 changes were also measured between suprasellar cistern CSF and other brain tissue types, with suprasellar cistern CSF showing a larger increase in mean R1 ($p < 0.001$) in all paired comparisons. Similary, whole CSF demonstrate a significantly higher increase of mean R1 compared to GM and WM ($p < 0.001$); further significant difference was found comparing mean R1 change in GM and WM, with GM showing the higher increase ($p < 0.001$; **Fig. 4.5**).

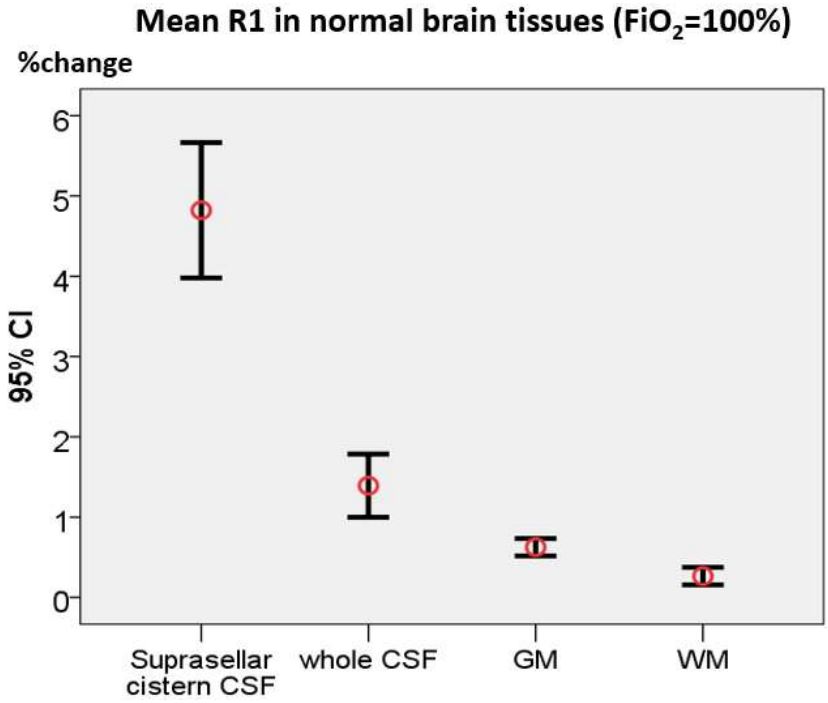

Figure 4.5 Confidence interval graph of mean R1 change in suprasellar cistern CSF, whole CSF, GM and WM patients with satisfactory gas delivery. Bars represent 95% confidence interval for mean R1 change in suprasellar cistern CSF, whole CSF, GM and WM of patients with satisfactory gas delivery. Significant differences are documented between each couple of tissue types.

2) Prediction of satisfactory gas delivery in suprasellar cistern CSF

In previous experiments, conducted in healthy subjects (chapter 3), undergoing brain OE-MRI scans under different FiO_2 levels, we had identified a cut-off value for %change of mean R1 measured in the suprasellar cistern CSF able to distinguish with sufficient accuracy the administration of 100% FiO_2 from delivery of 21% FiO_2.

The %change of mean R1 from baseline in the suprasellar cistern CSF (4.822%) in our patients, in response to 100% FiO_2, did not differ significantly from the corresponding %change in a subgroup of normal volunteers (n = 14) directly exposed to 100% FiO_2 following air (4.108%, see chapter 3). The threshold value (1.40%) was able to distinguish satisfactory from unsatisfactory gas delivery also in our patient group with notable accuracy (sensitivity = 95.83% and specificity = 100%, **Fig. 4.6**) with 19 true positive and no false negative cases.

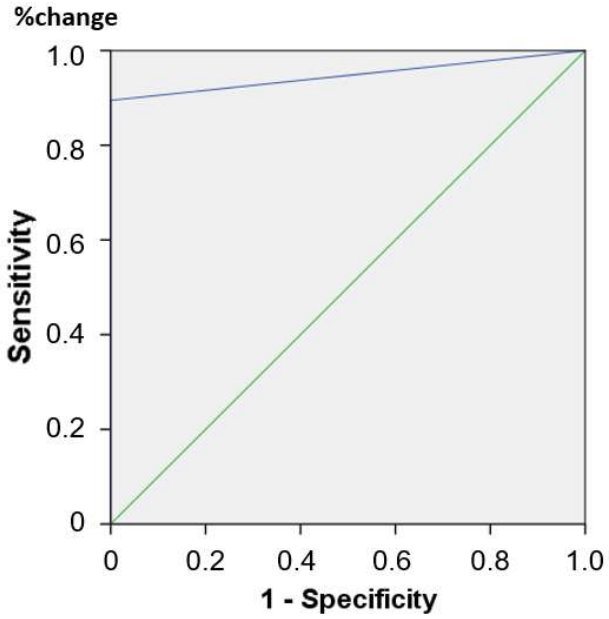

Figure 4.6 ROC curve for prediction of satisfactory 100%FiO_2 administration using a cut-off value of 1.40% for %change in mean R1 in suprasellar cistern CSF. The threshold value was identified using a cohort of normal volunteers administered with different FiO_2 levels.

Four out of 5 patient scans with unsatisfactory gas delivery were correctly classified (true negative). The only scan which was erroneously classified by the mean R1 cut-

off as "scan with satisfactory gas delivery" (false positive) was patient scan n. 11 – visit 2 (mean R1 change at 100% FiO_2 = 1.40%; male, 77 years, large right temporal tumor). Visit 1 of the same patient was correctly classified as (true negative; mean R1 change at 100% FiO_2 = 1.32%).

3) Effect of return to baseline FiO_2 (21%) in mean R1 of normal brain tissues

Following exposure to 100%FiO_2, in patients with satisfactory capnography data mean R1 at return to 21% FiO_2 did not present significant change compared to baseline mean R1 level, except for suprasellar cistern CSF (p = 0.016). However, under the administration of air, significant p values of change in suprasellar cistern CSF were detected only in four out 19 scans (see **Table 4.3**). Furthermore, in suprasellar cistern CSF, this change was statically lower than change detected under 100% FiO_2 (0.88% *vs.* 4.82%, respectively; p < 0.001; **Fig. 4.7**). No significant percentage changes from baseline in mean R1 were measured at 21% FiO_2 in scans with unsatisfactory gas delivery.

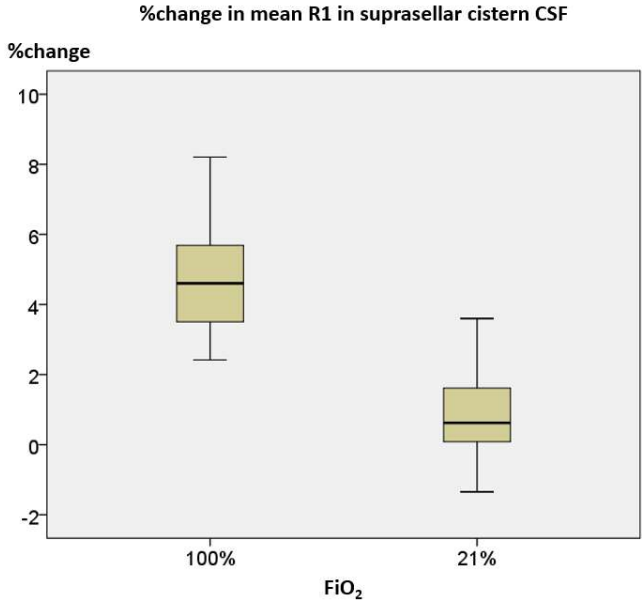

Figure 4.7 Whisker plot comparing %changes in mean R1 in suprasellar cistern CSF in patients with satisfactory capnography data at 100%FiO_2 and at return to 21%FiO_2 (following a $FiO_2$of 100%).

In addition, in patients with satisfactory oxygen delivery, magnitude of change in mean R1 at 100% FiO_2 demonstrated significant correlation ($p < 0.01$) with corresponding values at return to 21% FiO_2 in whole CSF, GM, WM but not in suprasellar cistern CSF (**Fig. 4.8**).

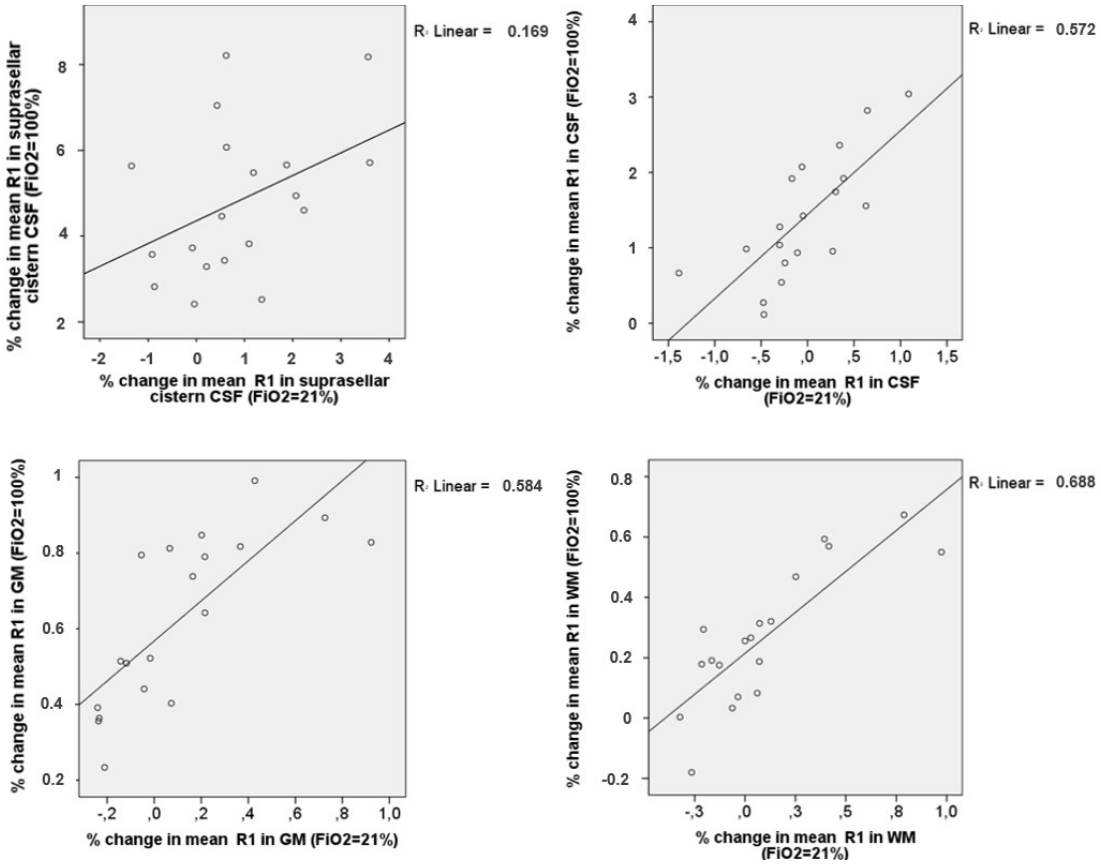

Figure 4.8 Scatter plots showing correlations of %change in mean R1 at 100% and at return to 21% FiO_2 in suprasellar cistern CSF, whole CSF, GM and WM.

4) The effect of 100% FiO_2 and 21% FiO_2 in mean R1 of brain tumor regions

In patients with no physiological capnography traces, no significant change in mean R1 was found at 100% FiO_2 or 21%FiO_2 in enhancing and non-enhancing regions.

In patients with satisfactory capnography data enhancing and non-enhancing tumor regions demonstrated significant change in mean R1 from baseline R1 level in response to 100% FiO_2 (2.31% and 1.42%, respectively; **Table 4.7- 9**).

	Average mean R1 at baseline FiO_2	Average mean R1 at 100% FiO_2	Average mean R1 at 21% FiO_2	%change in mean R1 (FiO_2 = 100%)	St. dev of %change	Lower CI (95%) of %change	Upper CI (95%) of %change	Sig. of %change (FiO_2 = 100%)
EN	0.712	0.729	0.714	**2.310**	1.002	1.777	2.743	**< 0.001**
NE	0.538	0.545	0.540	**1.424**	0.953	0.915	1.834	**< 0.001**

Table 4.7 Significance of %change of mean R1 in response to the administration of 100% FiO_2, in enhancing and non-enhancing regions in patient scans (n = 19) with satisfactory gas delivery (one sample 2-tailed t-test). EN = enhancing region; NE = non-enhancing region.

Enhancing regions presented a significantly higher positive change at 100% FiO_2 compared to non-enhancing regions (p = 0.008; **Fig. 4.9**); furthermore, at 100% FiO_2, all individual p values of change in enhancing regions resulted significant (**Table 4.8**), whereas, in non-enhancing region, only part of individual p values (12/19) proved significant (**Table 4.9**).

By contrast, at return to 21% FiO_2 following 100% FiO_2, significant mean R1 change was measured by means of 2-tailed one-sample t test in patients with satisfactory oxygen delivery only in non-enhancing regions (0.514%; C.I.: 0.084 – 0.844; p = 0.019). However the magnitude of change of mean R1 in non-enhancing regions was not significantly different from change in enhancing regions (0.232%, p = 0.206; **Fig. 4.9**) at independent sample t-test.

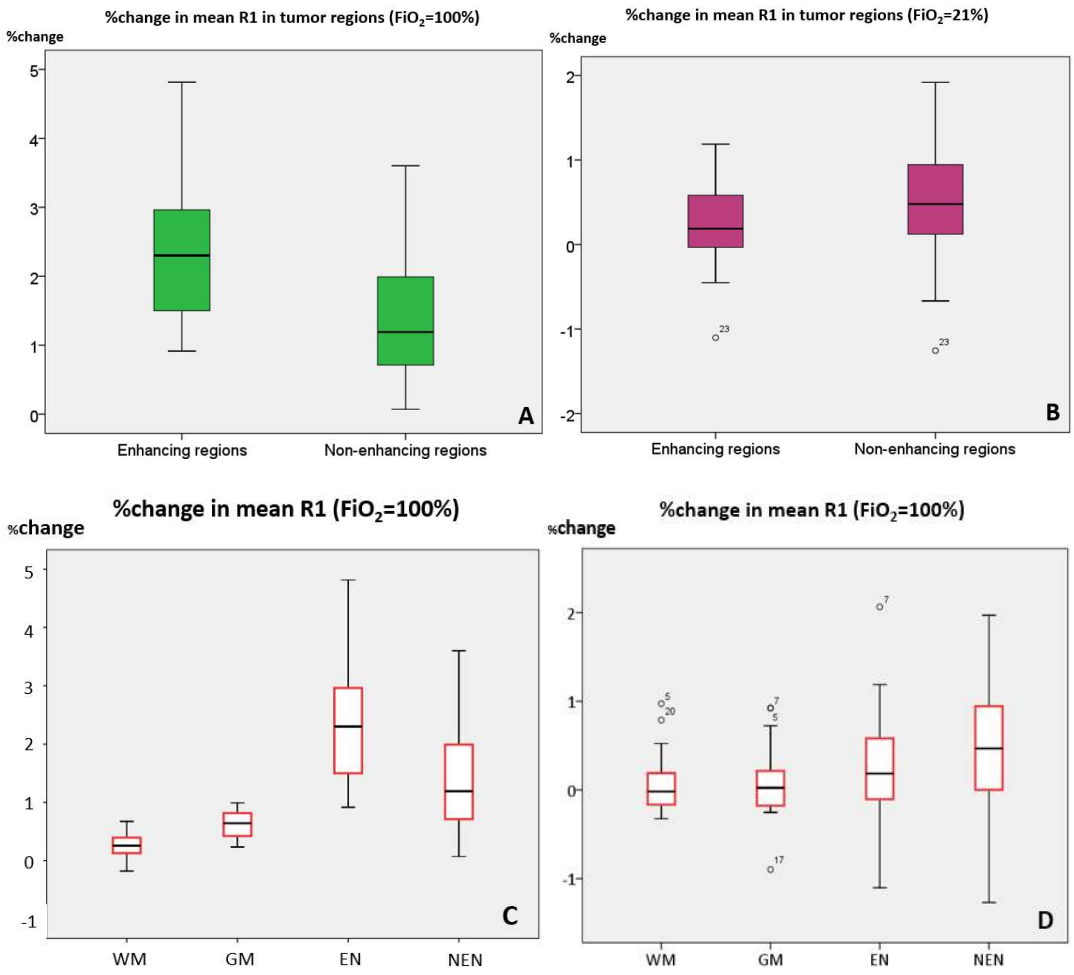

Figure 4.9 Whisker plot comparing %changes in mean R1 in enhancing and non-enhancing tumor regions in patients with satisfactory capnography data at 100%FiO_2. A: Whisker plot comparing %changes in mean R1 in enhancing and non-enhancing tumor regions in patients with satisfactory capnography data at 100%FiO_2. B: Whisker plot comparing %changes in mean R1 in enhancing and non-enhancing tumor regions in patients with satisfactory capnography data at 21%FiO_2. C: Whisker plot comparing %changes in mean R1 in WM, GM and tumor regions EN=enhancing; NEN=non-enhancing) in patients with satisfactory capnography data at 100%FiO_2. D: Whisker plot comparing %changes in mean R1 in enhancing and non-enhancing tumor regions in patients with satisfactory capnography data at 21%FiO_2.

Patient	FiO_2	%change in mean R1	p value of %change	FiO_2	%change in mean R1	p value of %change
Patient 1 visit_1	100	2.307	**< 0.0001**	21	0.187	0.336
Patient 1 visit_2	100	2.879	**< 0.0001**	21	0.830	**0.031**
Patient 2 visit_1	100	1.458	**0.019**	21	0.215	0.712
Patient 2 visit_2	100	3.044	**0.001**	21	0.0015	0.976
Patient 3 visit_1	100	2.881	**0.009**	21	1.187	**0.025**
Patient 3 visit_2	100	1.541	**< 0.0001**	21	0.492	**0.029**
Patient 4 visit_2	100	1.248	**0.013**	21	-0.035	0.938
Patient 5 visit_1	100	3.076	**< 0.0001**	21	0.808	**0.004**
Patient 5 visit_2	100	2.015	**< 0.0001**	21	0.182	0.499
Patient 6 visit_1	100	3.182	**< 0.0001**	21	0.817	**0.009**
Patient 6 visit_2	100	2.301	**< 0.0001**	21	-0.451	0.216
Patient 7 visit_1	100	2.351	**< 0.0001**	21	0.488	0.515
Patient 7 visit_2	100	1.292	**0.006**	21	-0.267	0.527
Patient 8 visit_1	100	2.162	**< 0.0001**	21	0.672	**0.032**
Patient 8 visit_2	100	0.916	**< 0.0001**	21	0.183	0.443
Patient 10 visit_1	100	0.968	**< 0.0001**	21	-0.180	0.427
Patient 10 visit_2	100	1.839	**0.002**	21	0.406	0.309
Patient 12 visit_1	100	3.614	**< 0.0001**	21	-1.103	**< 0.0001**
Patient 12 visit_2	100	4.814	**< 0.0001**	21	-0.031	0.847

Table 4.8 Individual percentage changes in mean R1 in enhancing tumor regions. Individual percentage changes in mean R1 in enhancing tumor regions (from baseline individual average mean R1) at 100% FiO_2 and at return to 21% FiO_2 with corresponding p values (significant values are in bold), assessed by 2-tailed independent samples t-test.

Patient	FiO_2	%change in mean R1	p value of %change	FiO_2	%change in mean R1	p value of %change
Patient 1 visit_1	100	1.271	**0.002**	21	0.566	**0.031**
Patient 1 visit_2	100	1.519	**0.003**	21	1.010	**0.028**
Patient 2 visit_1	100	2.212	**< 0.0001**	21	1.918	**0.024**
Patient 2 visit_2	100	1.869	**0.02**	21	0.397	0.411
Patient 3 visit_1	100	0.740	0.358	21	0.406	0.579
Patient 3 visit_2	100	0.425	0.131	21	0.315	0.350
Patient 4 visit_2	100	0.071	0.908	21	0.119	0.842
Patient 5 visit_1	100	1.735	**< 0.0001**	21	1.467	**0.001**
Patient 5 visit_2	100	1.127	**0.031**	21	0.871	0.041
Patient 6 visit_1	100	3.602	**< 0.0001**	21	1.717	**< 0.0001**
Patient 6 visit_2	100	3.229	**< 0.0001**	21	0.810	0.065
Patient 7 visit_1	100	1.142	0.124	21	0.880	0.253
Patient 7 visit_2	100	0.684	0.160	21	-0.667	0.452
Patient 8 visit_1	100	2.200	**< 0.0001**	21	1.044	**0.018**
Patient 8 visit_2	100	1.191	**0.001**	21	-0.117	0.718
Patient 10 visit_1	100	0.271	0.354	21	0.125	0.704
Patient 10 visit_2	100	2.114	**0.024**	21	0.427	0.544
Patient 12 visit_1	100	0.489	0.189	21	-1.256	**0.001**
Patient 12 visit_2	100	1.172	**0.002**	21	-0.315	0.360

Table 4.9 Individual percentage changes in mean R1 in non-enhancing tumor regions. Individual percentage changes in mean R1 in non-enhancing tumor regions (from baseline individual average mean R1) at at 100% FiO_2 and at return to 21% FiO_2 with corresponding p values (significant values are in bold), assessed by 2-tailed independent samples t-test.

In enhancing tumor regions of patients presenting satisfactory O_2 administration, no correlation was found between %change in mean R1 at 100% and 21% FiO_2 (R^2 =

0.001; p = 0.97); conversely, significant correlation was documented in non-enhancing tumor regions (R^2 = 0.433, p = 0.03; **Fig. 4.10**).

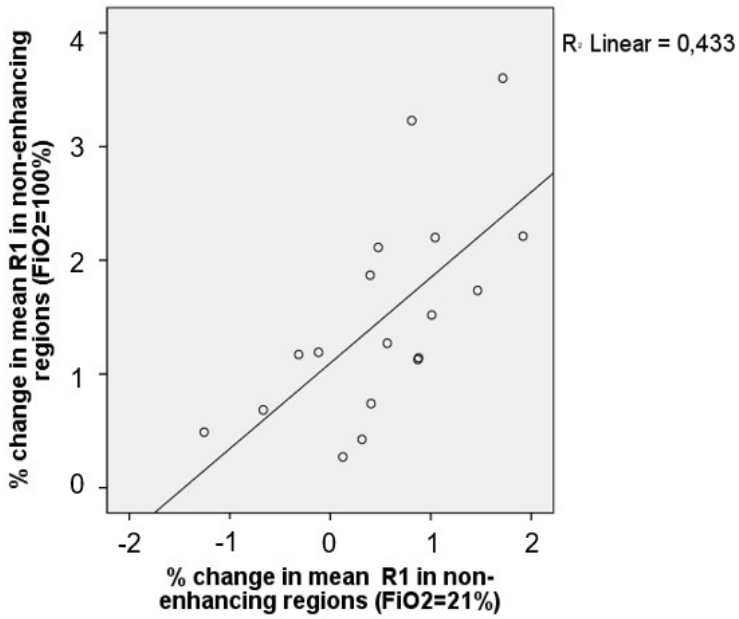

Figure 4.10 Scatter plot showing correlation of magnitude of change in mean R1 of non-enhancing regions at 100% and 21% FiO_2

5) Correlation of magnitude of change of mean R1 at 100% FiO_2 in different tissues

In dynamic sequences acquired under a FiO_2 of 100%, no significant correlation was found between magnitude of change in mean R1 and volume of tumor regions (p = ns).

Interestingly, the magnitude of change in mean R1 in suprasellar cistern CSF demonstrated a positive moderate correlation with %change of mean R1 in the enhancing tumor regions (R^2 = 0.319, p = 0.05). Percentage changes in mean R1 of CSF demonstrated significant inverse correlations with dimension of enhancing (R^2 = 0.314, p = 0.05) and non-enhancing regions (R^2 = 0.490, p = 0.01) and positive correlation with percentage change in mean R1 of GM (R^2 = 0.377, p = 0.05). A moderate positive correlation was also found between percentage changes in mean R1 of GM and WM (R^2 = 0.480, p = 0.01). Lastly, dimensions of enhancing and non-

enhancing regions demonstrated very strong correlation (R^2 = 0.815, p = 0.01, **Table 4.10**).

		ENH_R1_100%	NON-ENH_R1_100%	Dimension enhancing region	Dimension non-enhancing region	WM_100	GM_100	CSF_100	Supr_cist_CSF_100
ENH_R1_100%	Pearson Correlation	1	.236	-.142	-.235	.125	.367	.315	.565*
	Sig. (2-tailed)		.331	.562	.333	.611	.122	.190	.012
	N	19	19	19	19	19	19	19	19
NON-ENH_R1_100%	Pearson Correlation	.236	1	.017	-.085	.132	.277	.410	.189
	Sig. (2-tailed)	.331		.946	.730	.591	.251	.082	.439
	N	19	19	19	19	19	19	19	19
Dimension enhancing region	Pearson Correlation	-.142	.017	1	.903**	.308	-.119	-.561*	.315
	Sig. (2-tailed)	.562	.946		.000	.199	.627	.012	.188
	N	19	19	19	19	19	19	19	19
Dimension non-enhancing region	Pearson Correlation	-.235	-.085	.903**	1	.174	-.257	-.700**	.131
	Sig. (2-tailed)	.333	.730	.000		.477	.288	.001	.593
	N	19	19	19	19	19	19	19	19
WM_100	Pearson Correlation	.125	.132	.308	.174	1	.693**	.014	-.044
	Sig. (2-tailed)	.611	.591	.199	.477		.001	.956	.857
	N	19	19	19	19	19	19	19	19
GM_100	Pearson Correlation	.367	.277	-.119	-.257	.693**	1	.618**	.034
	Sig. (2-tailed)	.122	.251	.627	.288	.001		.005	.890
	N	19	19	19	19	19	19	19	19
CSF_100	Pearson Correlation	.315	.410	-.561*	-.700**	.014	.618**	1	.099
	Sig. (2-tailed)	.190	.082	.012	.001	.956	.005		.688
	N	19	19	19	19	19	19	19	19
Supr_cist_CSF_100	Pearson Correlation	.565*	.189	.315	.131	-.044	.034	.099	1
	Sig. (2-tailed)	.012	.439	.188	.593	.857	.890	.688	
	N	19	19	19	19	19	19	19	19

*. Correlation is significant at the 0.05 level (2-tailed).

**. Correlation is significant at the 0.01 level (2-tailed).

Table 4.10 Correlation coefficients of different variables in patients with satisfactory gas delivery at a FiO_2 of 100%

6) Time course of signal change in WM, GM, whole CSF and suprasellar cistern CSF in patients with satisfactory gas delivery

Time courses in patients with satisfactory gas delivery was analysed for experiments with significant p value of change in normal tissues in response to 100% FiO_2 (GM = 18; CSF = 17; suprasellar cistern CSF = 18). There were too few cases (n = 4) of WM masks with significant change to draw definite conclusions on time course.

After the switch to 100% FiO_2, mean R1 in suprasellar cistern CSF rose above the pre-set threshold value (mean R1 of baseline sequence + 1 SD) within 96 sec: bin 1 (24 sec) in 8/19 cases, bin 2 (5 cases) and bin 3 (4 cases) and bin 4 (1 scan). The peak signal change was reached starting from the 7th bin (after approximately 2 minutes and 30 sec from the switch) in 15/18 cases. After switching back from 100% FiO_2 to 21%

FiO_2 the mean R1 dropped below the threshold value in 16 out of 18 scans (within 4 bins = 96 sec in 11/16 cases).

In CSF, taking into account the 17 scans with significant individual p value of change in mean R1 in response to 100% FiO_2 (**Table 4.4**), R1 overcame the threshold value within 96 sec (bin 1 = 10 scans, bin 2 = 3 scans, bin 3 = 2 scans, bin 4 = 2 scans). The peak signal change was reached most frequently after approximately 2 minutes and 30 sec (in the last 5 bins in 12 experiments). The return to baseline level after the switch back to 21% FiO_2 happened in 15 cases (most commonly within 96 sec, 12/15 scans).

In GM the threshold value was passed in 17 out of 18 scans after switching FiO_2 from 21% to 100% (in 16/17 cases within the first 4 bins). The peak change was reached most commonly in the first 5 bins (120 sec; 10/18 scans) and the return to the baseline mean R1 level occurred in 14 cases (within the 96 sec in 13 experiments).

Suprasellar cistern CSF demonstrated a slower return below the mean R1 threshold level compared to whole CSF and GM in independent-samples Kruskal-Wallis test ($p = 0.012$). Typical time courses of mean R1 for brain tissues are presented in **Fig. 4.11**, whereas analysis of R1 mean time courses is summarized in **Table 4.11-13**.

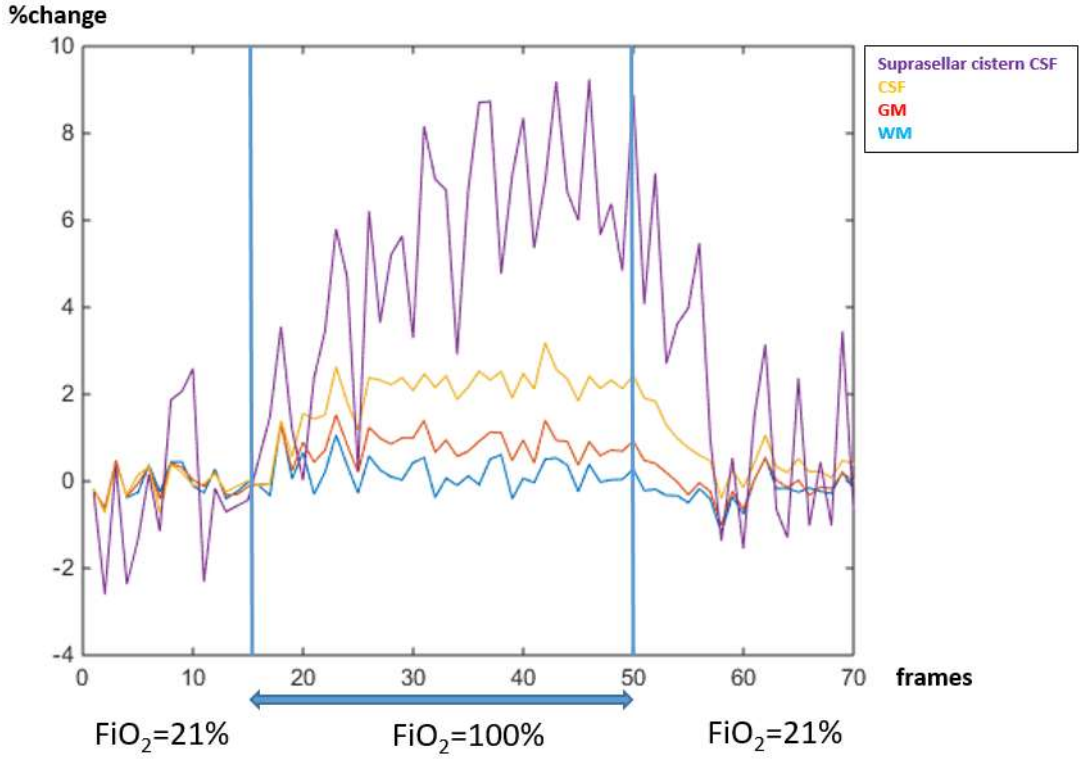

Figure 4.11 Multiseries plot representing typical time course of %change in mean R1 of different normal brain tissues in a patient scan. Patient 13 – scan 2; frames 1-15 were acquired under a FiO_2 of 21%; frames 16-50 were acquired under a FiO_2 of 100%; FiO_2 returns to 21% at the 50th frame; vertical light lines bar correspond to the time-points of FiO_2 switch.

	GM	CSF	Suprasellar cistern CSF
Patient 1 visit_1	1	1	2
Patient 1 visit_2	1	1	1
Patient 2 visit_1	1	1	1
Patient 2 visit_2		4	1
Patient 3 visit_1	2	1	1
Patient 3 visit_2	2	3	3
Patient 5 visit_1	1	2	1
Patient 5 visit_2	1	1	1
Patient 6 visit_1	3	2	3
Patient 6 visit_2	1	1	2
Patient 7 visit_1	2	2	3
Patient 7 visit_2	2		3
Patient 8 visit_1	1	1	2
Patient 8 visit_2	9	4	4
Patient 11 visit_1	2	3	2
Patient 11 visit_2	2	1	2
Patient 13 visit_1	1	1	1
Patient 13 visit_2	1	1	1
Mean bin	**1.9**	**3.2**	**4.3**

Table 4.11 Summary of ordinal bin numbers in R1 mean time courses passing the threshold (baseline mean R1 + 1 SD) after administration of a FiO_2 of 100% in different brain tissue types.

	GM	CSF	Suprasellar cistern CSF
Patient 1 visit_1	2	4	7
Patient 1 visit_2	2	4	7
Patient 2 visit_1	3	3	3
Patient 2 visit_2		7	4
Patient 3 visit_1	7	2	7
Patient 3 visit_2	5	10	10
Patient 5 visit_1	11	11	9
Patient 5 visit_2	5	2	9
Patient 6 visit_1	4	10	10
Patient 6 visit_2	6	5	10
Patient 7 visit_1	9	9	9
Patient 7 visit_2	9		11
Patient 8 visit_1	6	6	4
Patient 8 visit_2	11	11	9
Patient 10 visit_1	2	1	11
Patient 10 visit_2	10	10	11
Patient 12 visit_1	5	5	5
Patient 12 visit_2	5	9	7
Mean bin	**6**	**6.4**	**7.9**

Table 4.12 Summary of ordinal bin number in R1 mean time courses reaching the peak signal change after administration of 100% FiO_2 in different brain regions.

	GM	CSF	Suprasellar cistern CSF
Patient 1 visit_1	2	2	4
Patient 1 visit_2	3	3	
Patient 2 visit_1		2	
Patient 2 visit_2		2	3
Patient 3 visit_1	3	3	8
Patient 3 visit_2	1	3	4
Patient 5 visit_1	4	2	5
Patient 5 visit_2	2		4
Patient 6 visit_1	2	3	6
Patient 6 visit_2	4	6	6
Patient 7 visit_1	3	3	3
Patient 7 visit_2	1		4
Patient 8 visit_1			6
Patient 8 visit_2	1	3	1
Patient 10 visit_1	1	2	4
Patient 10 visit_2	1	6	2
Patient 12 visit_1	3	5	4
Patient 12 visit_2	2	3	4
Mean bin	**2.2**	**3.2**	**4.25**

Table 4.13 Number of time bins needed to in mean R1 time courses to pass the threshold (baseline mean R1 + 1 SD) after administration of 100% FiO_2 in different brain tissue types.

7) Reproducibility of time course in WM, GM, whole CSF and suprasellar cistern CSF in in patients with satisfactory gas delivery

No significant difference was detected for magnitude of change of mean R1 in response to the administration of 100% oxygen between visit 1 and 2 in normal brain tissues of patients with satisfactory gas delivery (WM = 0.309% *vs.* 0.271%; GM = 0.683% *vs.* 0.613%; CSF = 1.437% *vs.* 1.471%; suprasellar cistern CSF = 4.792 *vs.* 4.752%).

Reproducibility of change in mean R1 using the binned data was evaluated in patients presenting significant individual p value of %change in visit 1 and 2. Since for WM significant p values were documented only in 4 scans (patient 1 - visit 2, patient 2 - visit 1, patient n. 3 - visit 1 and patient 5 - visit 1), reproducibility of R1 mean dynamic courses was not assessed. Exemplificative plots of mean R1 dynamic course are presented in **Fig. 4.12**. In GM significant correlation between the mean R1 dynamic course of visit 1 and 2 was found in 6 cases for the ascending segment (FiO_2 switching from 21% to 100%) and in 6 patients for the descending segment (FiO_2 switching from 100% to 21%). The correlation was moderate (R^2 = 0.338) for the ascending portions and weak (R^2 = 0.268) for the descending portions of the dynamic courses. Only 5 out of 9 patients presented significant correlation in both ascending and descending portion of the dynamic courses (**Table 4.14**).

	Coeff. Det. (challenge)	Coeff. Det. (back to baseline)
Pt. 1	**0.859**	**0.921**
Pt. 2	0.332	**0.677**
Pt. 3	**0.726**	0.594
Pt. 5	**0.736**	**0.497**
Pt. 6	**0.739**	**0.769**
Pt. 7	**0.706**	**0.597**
Pt. 8	0.107	0.012
Pt. 10	0.131	-0.296
Pt. 12	**0.902**	**0.891**
Mean	0.582	0.518
SD	0.307	0.406

Table 4.14 Coefficients of determination for the ascending portion (challenge) and descending (back to baseline) portion of the mean R1 dynamic course in GM of patients undergoing the OE-MRI experiment twice. Significant correlation ($p < 0.05$) are presented in bold.

In the whole CSF region, strong reproducibility was found for the ascending segments ($R^2 = 0.546$) and moderate reproducibility ($R^2 = 0.448$) for the descending segments of the dynamic courses (**Table 4.15**).

	Coeff. Det. (challenge)	Coeff. Det. (back to baseline)
Pt. 1	**0.966**	**0.956**
Pt. 2	0.052	0.454
Pt. 3	0.370	0.526
Pt. 5	**0.576**	**0.834**
Pt. 6	**0.899**	**0.919**
Pt. 8	**0.727**	**0.727**
Pt. 10	**0.618**	0.414
Pt. 12	**0.955**	**0.916**
Mean	0.645	0.718
SD	0.317	0.223

Table 4.15 Coefficients of determination for the ascending portion (challenge) and descending (back to baseline) portion of the mean R1 dynamic courses in CSF of patients undergoing the OE-MRI experiment twice. Significant correlation ($p < 0.05$) are presented in bold.

In suprasellar cistern CSF, 6 out of 9 patients presented significant correlation in both ascending and descending segments of the R1 dynamic courses in visit1 and 2. Correlation resulted strong ($R^2 = 0.552$) for the ascending segments and moderate for the descending segments ($R^2 = 0.4$).

	Coeff. Det. (challenge)	Coeff. Det. (back to baseline)
Pt. 1	**0.981**	**0.917**
Pt. 2	**0.808**	**0.762**
Pt. 3	**0.825**	**0.850**
Pt. 5	0.670	0.403
Pt. 6	**0.879**	**0.827**
Pt. 7	**0.696**	0.483
Pt. 8	0.527	**0.537**
Pt. 10	**0.551**	0.157
Pt. 12	**0.746**	**0.759**
Mean	0.743	0.630
SD	0.149	0.249

Table 4.16 Coefficients of determination the ascending (challenge) and descending (back to baseline) portions of the mean R1 dynamic courses in suprasellar cistern CSF of patients undergoing the OE-MRI experiment twice. Significant correlation ($p < 0.05$) are shown in bold.

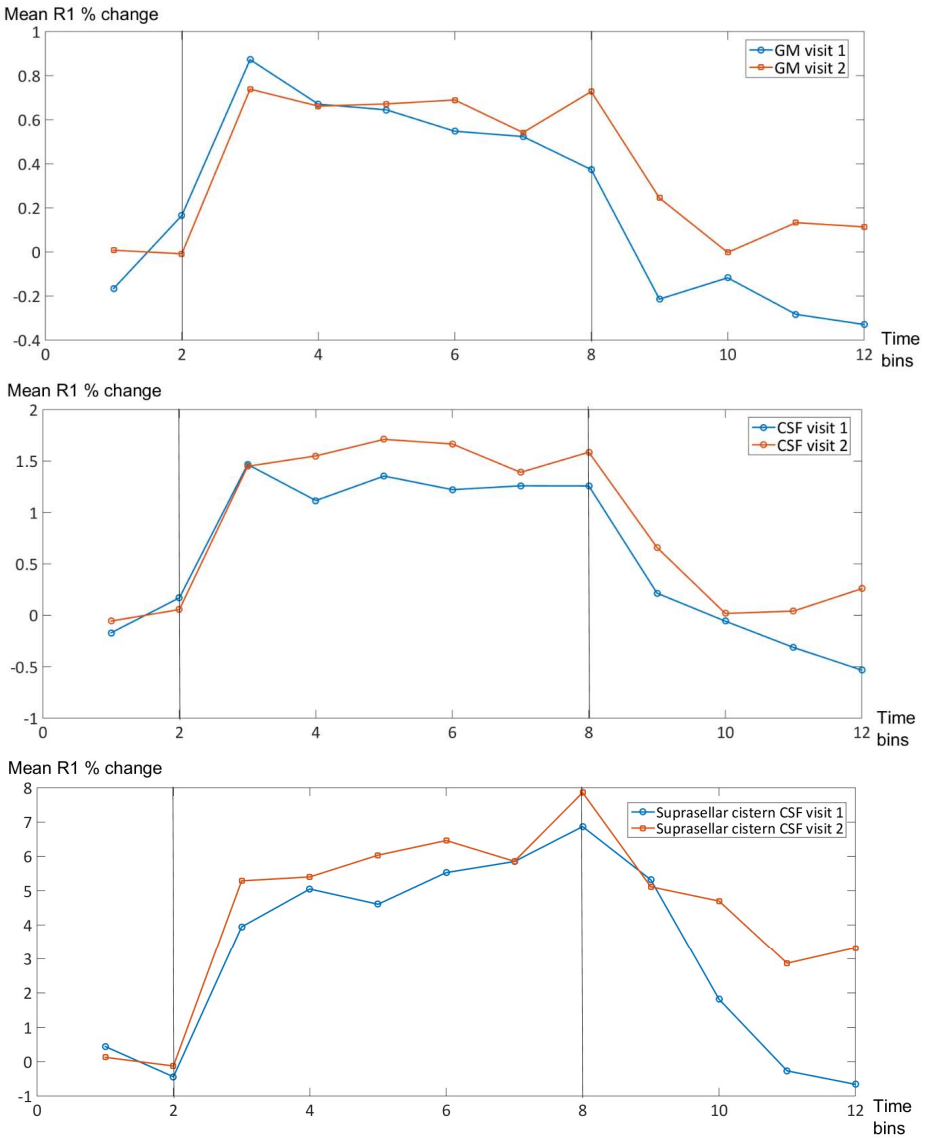

Figure 4.12 Time courses (visit 1 and 2) of %change in mean R1 in the GM, whole CSF and suprasellar cistern CSF. Patient n.1; bins 2-8 are acquired under FiO_2 of 100%.

The sub-analysis of the portion of mean R1 %change in response to 100% FiO_2 demonstrated the absence of significant differences between the slopes in visit 1 and 2 in all subjects (n = 9) for suprasellar cistern CSF, in 7/8 patients for whole CSF regions and in 5/9 subjects for GM (**Table 4.17**).

	Pt. 1	Pt. 2	Pt. 3	Pt. 5	Pt. 6	Pt. 7	Pt. 8	Pt. 10	Pt. 12
GM	0.008	**0.531**	**0.809**	**0.860**	0.005	**0.751**	0.045	0.008	**0.720**
CSF	**0.577**	**0.088**	0.012	**0.697**	**0.089**	N/A	**0.207**	**0.062**	**0.300**
Suprasellar cistern CSF	**0.587**	**0.338**	**0.098**	**0.494**	**0.052**	**0.148**	**0.216**	**0.374**	**0.167**

Table 4.17 Comparison of slopes under the administration of 100% FiO_2 in GM, whole CSF, suprasellar cistern CSF in patients with satisfactory O_2 delivery in both the OE-MRI experiments. P values > 0.05 indicate absence of significant differences between the two visits.

8) Time course of signal change in brain tumor regions in patients with satisfactory gas delivery

Mean R1, in enhancing regions, surpassed the threshold value within 2 bins (48 sec) in all patient scans except one (n = 18, excluding patient 7 - visit 2) after switching FiO_2 from 21% to 100%. The peak signal change was reached most commonly after two minutes and 30 sec (bin $\geq 7^{th}$ in 13/19 scans) and the return to the baseline mean R1 level occurred in 17 cases (within 96 sec in 12 experiments) (**Fig. 4.13** and **Table 4.18**).

In non-enhancing regions (12 scans with significant individual p value of change), the threshold was passed in 7 out of 12 scans after the enhancing regions and in 5 cases in the same bin. The peak was reached in a similar timing (mean bin = 7.5) compared to enhancing regions. The return to baseline mean R1 level occurred slightly after the corresponding timing for the corresponding time regions (the same bin in 5/8 cases and one bin after in 3 scans); the return to the baseline level did not occur within the

end of the experiments in 4/12 patient scans. In non-enhancing regions the threshold value was passed significantly later compared to enhancing regions as evaluated by Wilcoxon's rank sum test ($p = 0.016$).

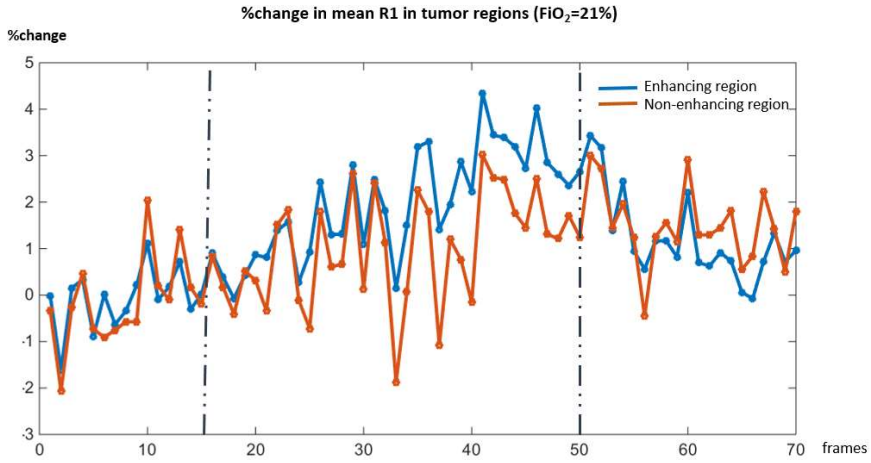

Figure 4.13 Multiseries plot representing typical time course of %change of mean R1 of the enhancing and non-enhancing tumor regions in a patient scan (pt. n. 5 – scan 1). Frames 1-15 were acquired under a FiO_2 of 21%; frames 16-50 were acquired under a FiO_2 of 100%; FiO_2 returns to 21% at the 50th frame; vertical dotted black lines correspond to the time-points of FiO_2 switch.

	Threshold EN region	Threshold NE region	Peak change EN region	Peak change NE region	Back to baseline EN	Back to baseline NE
Patient 1 visit_1	1	2	4	6		
Patient 1 visit_2	1	1	7	7		
Patient 2 visit_1	1	2	4	4	5	
Patient 2 visit_2	1	2	4	6	5	5
Patient 3 visit_1	1		7		3	
Patient 3 visit_2	1		10		2	
Patient 4 visit_2	1		5		2	2
Patient 5 visit_1	2	3	9	10	6	
Patient 5 visit_2	2	4	11	11	5	5
Patient 6 visit_1	1	4	11	11	7	
Patient 6 visit_2	2	2	9	6	4	4
Patient 7 visit_1	2		8		3	
Patient 7 visit_2	4		8		1	
Patient 8 visit_1	2	2	10	5	3	4
Patient 8 visit_2	2	2	8	9	2	4
Patient 10 visit_1	2		5		3	
Patient 10 visit_2	2	5	10	9	2	2
Patient 12 visit_1	1		3		3	
Patient 12 visit_2	1	1	9	6	4	5
Mean bin	**1.6**	**2.5**	**7.5**	**7.5**	**3.5**	**3.9**

Table 4.18 Comparison of mean R1 time courses in tumor enhancing (EN) and non-enhancing regions (NE)

9) Reproducibility of time course in brain tumor regions of patients with satisfactory gas delivery

Between visit 1 and 2 of patients with satisfactory capnography data no significant differences were found in mean R1 change in response to 100% FiO_2 either in enhancing (2.44% *vs.* 2.29%; p = ns) or non-enhancing tumor regions (1.51% *vs.* 1.42%; p = ns). Parametric maps were also generated using an in-house R script for display and comparison purposes (visit 1 *vs*. visit 2). An example comparison between different types of maps (ΔR1, ΔR1 max, ΔR1 t-test) in a patient with satisfactory gas delivery in both OE-MRI experiments is shown in **Fig. 4.14**.

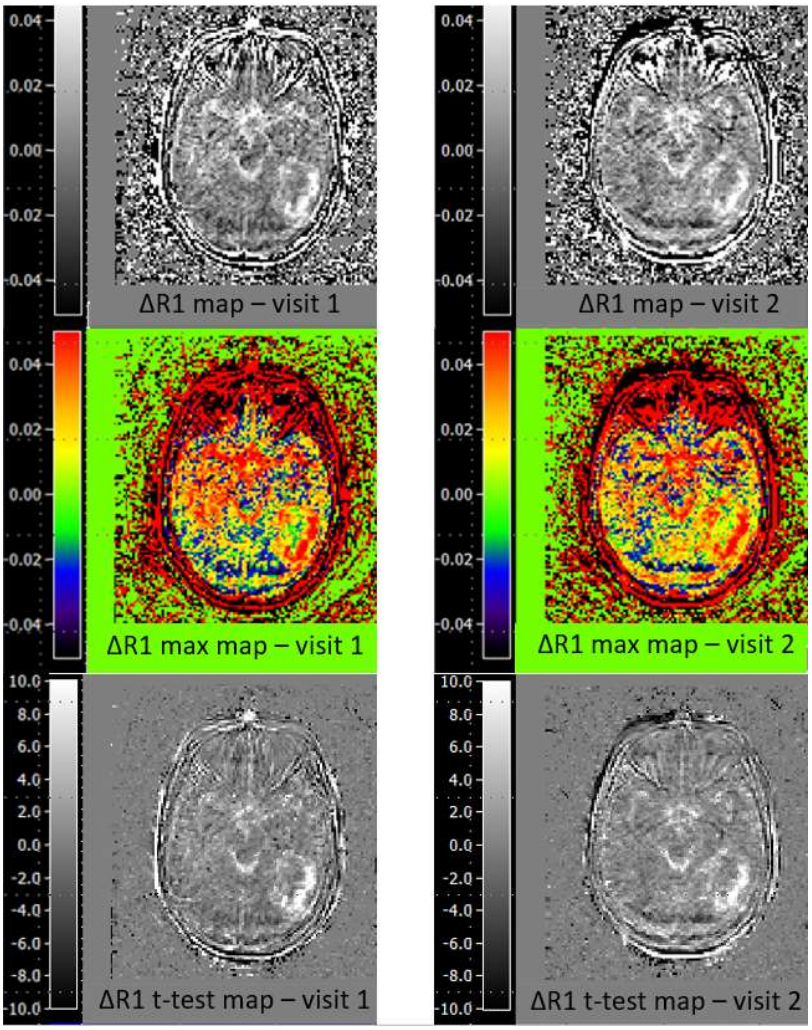

Figure 4.14 ΔR1, ΔR1 max, ΔR1 t-test maps in patient n. 1 (visit 1 and visit 2)
ΔR1 = mean R1(FiO_2 = 100%)-mean R1(baseline FiO_2); ΔR1 max = maximum R1(FiO_2 = 100%)-maximum R1(baseline FiO_2); ΔR1 t-test = significance of change using Welch's t-statistic: peak-baseline.

Strong correlation ($R^2 = 0.624$) between visit 1 and 2 was demonstrated only for the ascending segment of the mean R1 time courses in the enhancing regions, whereas weak correlation was found for the descending segment ($R^2 = 0.254$) of the time courses. In the non-enhancing regions, the ascending and the descending segments demonstrated, respectively, moderate ($R^2 = 0.469$) and weak correlation ($R^2 = 0.06$; **Table 4.19**).

	Coeff. Det. (challenge)		Coeff. Det. (back to baseline)	
	EN	NE	EN	NE
Pt. 1	**0.98**	**0.836**	**0.974**	0.343
Pt. 2	**0.935**	-0.11	**0.919**	-0.534
Pt. 3	0.601	N/A	0.149	N/A
Pt. 5	**0.834**	0.178	**0.655**	0.008
Pt. 6	**0.824**	**0.906**	**0.801**	**0.83**
Pt. 7	**0.685**	N/A	**0.729**	N/A
Pt. 8	**0.772**	**0.712**	**0.628**	**0.613**
Pt. 10	0.486	N/A	0.354	N/A
Pt. 12	**0.935**	N/A	**0.957**	N/A
Mean	0.790	0.504	0.685	0.252
SD	0.159	0.447	0.280	0.536

Table 4.19 Coefficients of determination for the ascending portion (challenge) and descending (back to baseline) portion of the mean R1 dynamic courses in tumor regions of patients with satisfactory O_2 delivery in visit 1 and 2. Significant correlation ($p < 0.05$) are presented in bold. EN = enhancing region; NE = non-enhancing region.

Most of the slopes of mean R1 %change, acquired under 100% FiO_2, did not present significant differences between visit 1 and 2 in the enhancing (8/9 pairs of experiments) and non-enhancing regions (5/5 couples of experiments; see **Table 4.20**).

	Pt. 1	Pt. 2	Pt. 3	Pt. 5	Pt. 6	Pt. 7	Pt. 8	Pt. 10	Pt. 12
EN	**0.26**	**0.71**	**0.627**	0.03	**0.239**	**0.973**	**0.768**	**0.141**	**0.058**
NE	**0.325**	**0.409**	N/A	**0.832**	**0.947**	N/A	**0.367**	N/A	N/A

Table 4.20 Comparison of slopes under the administration of 100% FiO_2 in enhancing and non-enhancing tumor regions in patients with satisfactory O_2 in the two OE-MRI experiments
P values > 0.05 indicate absence of significant differences between the two visits. EN = enhancing region; NE = non-enhancing region.

Discussion

Although hypoxia is definitively considered a relevant biological feature in high-grade glioma, conditioning resistance to conventional treatments, no MRI technique for the characterization of tumor hypoxia in brain tumors has yet gained access to the clinical scenario [33]. R1 change has been investigated by different preclinical and clinical studies as a marker of hypoxia [62, 74, 159]. Measurement of change in R1 may provide prognostic stratification and help selecting patients with brain tumors with higher change of benefit from hypoxia-modifying treatments. Furthermore, serial measurements of R1 change may be useful in monitoring treatment response [52].

This is the first study evaluating the time course and reproducibility of R1 change in response to the administration of 100% FiO_2 in normal brain tissue and tumor regions of patients affected by high-grade glioma. In this study, in patients with satisfactory O_2 delivery, significant %changes of mean R1 were identified at 100% FiO_2 in suprasellar cistern CSF (4.82%) followed by whole CSF (1.39%), GM (0.626%) and WM (0.266%), at a magnitude in keeping with previous studies in animal models [93]. In healthy subjects undergoing OE-MRI (see chapter 3) we had documented similar changes of mean R1 in suprasellar cistern (4.83%) but lower proportional changes in GM (0.438%, with individual significant changes in only 7 out of 15 scans) and no significant changes in WM (p = ns). Some authors have also reported the lack of change of T1 values in GM and WM in response to hyperoxia in healthy subjects [147, 149, 162]. Given the adequate O_2 delivery, the reason for the higher changes of mean R1 in GM and WM in patients may be related to the lost or impairment of the downregulation of CBF in response to hyperoxia. We could not acquire PCA data in our patient group because additional sequences would have prolonged the MRI protocol and limit patient compliance; therefore, this hypothesis will need to be fully

validated in future studies including quantitative measurement of CBF. Nevertheless, the absence of an efficient autoregulatory mechanism of CBF would strength the reliability of R1 change measurement in patients with subcortical lesions.

Taking into account CSF, R1 change may be related to direct diffusion of O_2 from brain arteries, as suggested by preclinical evidence [154]. In our study, this mechanism is also reinforced by the inverse relationship between tumor size and %change of mean R1 in CSF; higher tumor compression may possibly diminish the flow and determining lower O_2 diffusion to the CSF. In turn, the higher intracranial pressure of CSF due to the tumor compression may cause lower O_2 delivery to the tumor explaining also the inverse correlation we found between the magnitude of R1 change in CSF and in enhancing regions at 100% FiO_2.

Magnitude of change of mean R1 in whole CSF demonstrate also a linear correlation with corresponding %changes in GM and WM during the hyperoxic challenge; conversely change of mean R1 in suprasellar cistern CSF did not present significant correlation with other tissues. The intrinsic difference of suprasellar cistern CSF region compared to other brain tissue components emerges also from the analysis of R1 mean dynamic courses. Following the administration of 100% oxygen, mean R1 presented significant change (above the prefixed threshold) within short time (96 sec) in all brain components. The time of onset of significant change in mean R1 can be in part justified by the sum of the time interval needed for the oxygen to fill the gas delivery system and the time needed by the oxygen saturation to reach the maximum level [155]. However, mean R1 showed a trend in surpassing the threshold value and reaching the peak level in suprasellar cistern after CSF and GM. In particular, mean R1 level surpassed the threshold value in the suprasellar cistern CSF in the same bin or after the whole CSF and GM masks in 12/17 cases; similarly, the peak signal change in

suprasellar cistern CSF was reached in 12/17 cases in concomitance or after the whole CSF and GM regions. The difference of temporal patterns between whole CSF and suprasellar cistern may also be partially justified by the inclusion of sulcal CSF in the whole CSF mask, since sulcal CSF is exposed to a larger surface area of diffusion represented by the vessels on the brain cortex, as also suggested by Bhogal *et al.* [149]. One of the novelties of the present study is the identification of a cut-off of mean R1 %change in suprasellar cistern CSF (1.40%), in response to the administration of 100% oxygen, to discriminate satisfactory from unsatisfactory O_2 delivery (AUC = 0.905; sensitivity = 95.83% and specificity = 100%) in patients with brain tumors undergoing OE-MRI. In a previous study at our institution (see chapter 3) the same threshold discriminated administration of 100% FiO_2 from 21% FiO_2 in a group of healthy volunteers with comparable diagnostic performance (AUC = 0.900; sensitivity = 93.3% and specificity = 81%). The only patient who was wrongly classified as "patient with satisfactory gas delivery" by means of the cut-off reported some problem in holding the mouthpiece due to dentures (male, 77 years) and got a suboptimal amount of O_2. Nevertheless, we believe that this mean R1 %change threshold may result useful in radiology departments not equipped with capnography analysis system to provide confirmation of correct oxygen administration. However, further validation in larger groups of patients with high-grade gliomas in warranted.

Within the tumor lesions, in contrast to our expectations, we documented significant changes not only in the enhancing regions but also in the non-enhancing core of the tumor, which is commonly known to have poor perfusion and correlate with presence of hypoxic and anoxic tissue at histological examination [163-165]. Of note, preclinical studies on different tumor models have recently demonstrated that that even in necrotic tissue, late and slow enhancement of gadolinium in the tumor interstitium

may still occur due to passive diffusion dictated by spatial concentration gradients [166-168]. This fact may, therefore, explain the significant but lower ($p = 0.008$) and slower ($p = 0.016$) R1 change in non-enhancing areas reflecting scarce O_2 diffusion, which is the biological cause of chronic hypoxia [33]. An additional point that would need to be cleared is whether O_2 diffuses from the enhancing to the non-enhancing regions or reaches the interstitium due to misery perfusion through non-functional capillaries. Likewise, the significant change of mean R1 in non-enhancing regions at return to air, following administration of pure oxygen, may simply reflect the slower wash-out of O_2 and compared to enhancing regions. The same consideration is possibly interesting also normal brain tissues. The return to the baseline mean R1 level was slower in suprasellar cistern CSF and whole CSF than GM, probably reflecting difference in O_2 diffusion across pial and large brain arteries. Significant correlations were also found between changes of R1 at 100% and at return to baseline FiO_2 in CSF, GM, WM and non-enhancing regions probably due to the effect of residual O_2 at the moment of R1 measurement. As expected mean R1 change in response to 100% FiO_2 occurred in non-enhancing regions after enhancing regions, suggesting that O_2 may present a slower diffusion in the inner putative hypoxic core of the tumor. However, no significant differences were evidenced between the two types of tumor regions for the bins corresponding to the peak signal change and the return below the mean R1 threshold value after the switch of FiO_2 from 100% to 21%.

The linear correlation of mean R1 change in suprasellar cistern CSF and in enhancing tumor areas could instead reflect simply brain blood flow. In normal volunteers (chapter 3) we had documented an inverse correlation between R1 change (reflecting oxygen content) in suprasellar cistern CSF at 100% FiO_2 and flow change of internal carotid arteries (showing reduction at increasing FiO_2 levels). Conversely, in patients

the correlation between changes of mean R1 in suprasellar cistern CSF and enhancing regions is linear due to the lack of autoregulation of cerebral blood flow in response to hyperoxia. In contrast, %change of mean R1 in suprasellar cistern CSF did not show correlation with magnitude of change of mean R1 in non-enhancing tumor regions, possibly suggesting that O_2 in putative hypoxic regions is influenced by non-functional and unpredictable lower perfusion compared to enhancing regions.

Linnik *et al.* first demonstrated a linear correlation between ΔR1 in response to administration of pure oxygen and pimonidazole binding in an animal brain tumor model [62]. Recently Fan and colleagues in a study with rat model of glioma (n = 25 Sprague-Dawley rats) proved the presence of tissue hypoxia in tumor areas with less increasing signal compared to non-hypoxic tumor regions. In their study the glioma models underwent a turbo-spin-echo sequence with inversion recovery (IR) and the authors used a threshold of 10%change in percentage of signal intensity change (PSIC) maps in response to administration of 100% oxygen to define low and high regions of interest. The authors demonstrated the correlation of tumor areas with low PSIC (< 10%) with hypoxia staining (GLUT-1) and necrosis ($r = 0.71$; $P < 0.05$) and a significant longer survival (log-rank $P = 0.035$) in rats with higher PSIC [160]. Similarly, also in patients undergoing OE-MRI VFA protocols, there could be a threshold of mean R1 at a voxel level that could be tested as imaging biomarker of hypoxia; however, this hypothesis deserves further well-designed studies including histological assessment.

In addition, this is the first study demonstrating reproducibility (visit 1 *vs.* visit 2) of the magnitude of mean R1 change in human normal brain tissue components and high-grade gliomas. In addition, the pattern of rise of the mean R1 dynamic courses in response to administration of 100% FiO_2 resulted sufficiently reproducible in normal

tissues and tumor regions. Similar reproducibility was documented for the R1 mean dynamic course in response to the administration and cessation of 100% FiO_2. The only evident exception was the return to the baseline mean R1 level in non-enhancing regions which presented weak reproducibility.

Conclusions

From this investigation, mean R1 change appears to be significant and acceptably reproducible in normal brain tissue, especially in suprasellar cistern CSF, and in tumor regions (in particular in the enhancing areas of the lesion) in terms of magnitude and rate of change. Therefore, mean R1 may be used as a metric in clinical trials involving patients with brain tumors undergoing OE-MRI, ensuring that participants are receiving proper O_2 delivery. Our findings suggest that R1 change may be correlated, at least partially, to O_2 diffusion. The magnitude of change of mean R1 in CSF is associated to tumor volume and therefore possibly influenced by blood flow.

Chapter 5 Histogram Analysis of Extravascular Extracellular Space Data from DCE-MRI in Glioblastoma Provides a Potential Imaging Biomarker Of Micro-necrosis, Related To Survival

This chapter describes a retrospective MRI study, which has been submitted for publication. The authors are Dr Ka-loh Li, Dr Natale Quartuccio, Dr Samantha Mills and Prof Alan Jackson.

The study design was by Prof Jackson; Dr Mills has been involved with the recruitment, data acquisition and analysis; data processing was done by Dr. Dr Ka-loh Li and the candidate. Dr Ka-loh Li has also been involved in the development of the analytical techniques.

Data analysis and statistical analysis was done by Dr Ka-loh Li Prof Jackson and the candidate. The candidate gave his contribution in writing the first draft of the manuscript. Prof Jackson performed much of the statistical analysis and manuscript preparation. All authors have provided input into writing and editing of the manuscript. This study was jointly funded by Cancer Research UK and the Engineering and Physical Sciences Research Council (Grant reference C8742/A 18097).

Abstract

Background: This study was designed to test the hypothesis that "features describing the distribution of DCE-MRI derived parameters provide additional predictive power for overall survival (OS) compared to estimation of median or mean values".

Methods: 27 patients with glioblastoma were imaged prior to treatment. Imaging included T_1-weighted DCE-MRI and data were analyzed using median and centile values of DCE-MRI parameters. Histograms of *ve* were processed using a Gaussian-mixture model.

Results: Using only median values of DCE derived parameters, age, $R1_{med}$, $(v_e)_{med}$ and $(v_p)_{med}$ were independent significant predictors of OS. Inclusion of centile values showed age, $R1_5$, v_{e20} and K^{trans}_{med} as predictors. Following Gaussian fitting of *ve*, three fitting parameters $\mu 2$, W3 and $\sigma 3$ showed significant variations in hazard rates across quartiles. Multiparametric proportional hazards modeling showed age, v_p, $\mu 2$, and $\sigma 3$ as independent significant predictors and this model was significantly superior to the others. The second and third Gaussian components identify a tissue habitat adjacent to nonperfused areas in patients with long

survival and an increased volume distributed throughout the enhancing tumor in patients with short survival.

Conclusions: Accurate measurements of v_e support identification of a distinct tumor habitat whose existence relates to survival.

Introduction

Overall survival in Glioblastoma (GBM) varies significantly and there is increasing interest in the identification of predictive and early response biomarkers. Overactivation of the epidermal growth factor receptor (EGFR), O6-methylguanine-DNA methyltransferase (MGMT) promoter methylation, TP53 mutation and Ki-67 indices provide prognostic information but cannot be assessed without resection or biopsy [22].

A number of MR-derived imaging biomarkers (IB) correlate with progression free survival (PFS), overall survival (OS) or various specific tissue characteristics. Texture analysis of contrast enhanced MR images provides prognostic information [169, 170]. However, IB derived from dynamic contrast enhanced MRI (DCE-MRI) and diffusion weighted imaging (DWI) have received particular attention. Apparent diffusion coefficient (ADC) is predictive of OS particularly in pure astrocytic tumors [171-173]. Relative cerebral blood volume (rCBV) from dynamic susceptibility contrast-enhanced MR is predictive of OS and PFS [174-177] and the contrast transfer coefficient (K^{trans}) derived from DCE-MRI is predictive of OS [178], MGMT methylation [179] and EGFR status [180]. Recent work has also described a relationship between OS and the extravascular extracellular volume fraction (v_e)[181]. Choi and colleagues showed improved predictive power for DCE-MRI parameters when centile values and the shape of the distribution curve are considered [182]. OS was best predicted by the 5^{th} centile value of K^{trans} and kurtosis of v_e and PFS by the minimum and 5^{th} percentile values of K^{trans} and kurtosis of v_e.

Recent workers have hypothesized that tumor "habitats", identified by multispectral imaging data, represent tissue subtypes that drive localized biological and genetic variability giving rise to the concept of "habitat imaging"[183, 184].

In this study we describe the additional information provided by analysis of data distributions of parametric variables from DCE-MRI. We describe the identification of a tissue habitat, defined by Gaussian fitting of the histogram of v_e, the presence of which is directly related to survival.

Materials and Methods

Patients

Ethical approval was obtained for the study from the North-West of England Medical Ethics committee (NW 04-293), the study was performed in accordance with the experimental protocol approved and all patients gave informed consent prior to imaging. All imaging was performed prior to surgery and all patients received corticosteroid treatment for a minimum of 48 hours prior to imaging. Suitable patients were identified via the weekly neuro-oncology multi-disciplinary team meetings at Salford Royal NHS Foundation Trust. Inclusion criteria included: 1) age > 17 years; 2) histological confirmation of grade IV GBM according to World Health Organisation (WHO) criteria. Exclusion criteria included: 1) patients in whom MRI was contraindicated, 2) failure to histologically confirm GBM, 3) patients who did not receive standard treatment of concomitant and adjuvant temozolomide with radiotherapy and 4) patients in whom death was unrelated to the diagnosis of GBM. Clinical notes were reviewed retrospectively to establish the date and cause of death. This cohort has been reported previously in two studies examining the relationship between enhancing fraction and tumor grade [185, 186].

Data acquisition

Imaging was performed at Salford Royal Foundation Trust on a 3 Tesla Philips Achieva system (Philips Medical Systems, Best, NL) using an 8-channel SENSE head coil. All imaging sequences were acquired in a sagittal oblique orientation incorporating the internal carotid for arterial input function (AIF) measurement. Imaging sequences included:

1) Sagittal oblique pre contrast T_1-weighted sequence (TR 9.3 ms, TE 4.6 ms, slice

thickness 4.2 mm, 128 x 128);

2) Three T_1-FFE spoiled gradient echo sequences with different flip angles (2°, 10°, 16°) for calculation of baseline T_1 maps (TR 3.5 ms, TE 1.1 ms, slice thickness 4.2 mm, 128 x 128);

3) Dynamic, contrast enhanced acquisition with identical acquisition parameters as above and a flip angle of (16°), consisting of 100 volumes with temporal spacing of approximately 3.4 seconds. Gadolinium-based contrast agent (Gd-DTPA-BMA; Omniscan, GE Healthcare, Oslo, Norway) was injected using a pressure injector as a bolus of 3ml, at a rate of 15 mls^{-1} and dose of 0.1 $mmolkg^{-1}$ of body weight after acquisition of the fifth image volume. This was followed by a saline flush;

4) A sagittal oblique post contrast T_1-weighted sequence (TR 9.3 ms, TE 4.6 ms, slice thickness 4.2 mm, 128 x 128).

Data analysis

Tumor volumes of interest (VOIs) were manually defined using a previously validated technique (Intraclass Correlation Coefficient > 0.94)[185]. Initial analysis used the extended Tofts and Kermode model [187] using MIStar (Apollo Medical Imaging, Melbourne, Australia) according to the conventional equation describing the equilibrium of contrast media between the intravascular space and the extravascular-extracellular space (EES):

$$\frac{dC_t}{dt} = K^{trans}(C_p - \frac{C_t}{v_e})$$

where C_t is the concentration of the contrast media in the tissue, t is the time, K^{trans} is the volume transfer constant (from plasma to EES), C_p is the concentration of contrast media in plasma and v_e is the fractional volume of EES per unit volume of tissue [188].

Parametric maps of R1, the integrated area under the contrast concentration curve over 60 seconds ($IAUC_{60}$), the enhancing fraction (EnF%), the contrast transfer coefficient (K^{trans}), the proportional vascular fraction (v_p) and the extravascular extracellular fraction (v_e) were generated. Measurements of the median value and of the 5th, 10th, 20th, 90th and 95th centile

values were recorded for each variable. These were designated by the abbreviation of the variable followed by of subscript indicating median values (med) or individual centile values (5, 10, 20, 90, 95).

Dynamic data was re-analyzed using a modified hybrid pharmacokinetic model to reduce artefactual correlations between parameters [189] and histograms of v_e constructed. This hybrid models combines two major approaches for the analysis of DCE-MRI from the first passage of a Gd-DTPA contrast bolus, tested at our institution, in order to improve the accuracy of the estimation of K^{trans}, v_p and v_e: 1) the multiparametric curve-fitting (MPCF) approach and the 2) first-pass leakage profile (FPLP) method [189-191].

The hybrid method derives v_e values by the MPCF method from the equation:

$$C_i(t) = k_{\int p} \int_0^t C_p(t')d\,t'$$

which describes the leakage profile of the tumor, namely the relationship between $k_{\int p}$ (permeability), *Ci(t)* (tracer concentration measured from the tumor) and the sum of accumulated Cp(t) in the vascular compartment.

The final values of v_p are obtained from the FPLP analysis according to the equation [189]:

$$v_p = \int_0^{T_{FP}} C_v(t')dt' / \int_0^{T_{FP}} C_p(t')dt' /$$

where the fractional plasma volume - v_p – is the ratio of the area under the $C_v(t)$ curve and the area under the *Cp(t)* curve, during the first passage of the contrast agent bolus; T_{FP} is the end of the first pass.

Patients were divided into three groups characterized by OS: group 1 (OS < 150 days); group 2 (OS = 150-365 days); group 3 (OS > 365 days). Group histograms were produced by pooling all tumor voxels and normalizing by the total number of tumor voxels in the group. Group histograms were plotted on the same axes to support direct comparison.

Histograms of v_e were fitted using a mixture of Gaussian functions, a parametric probability density function generated as a weighted sum of a finite number of Gaussian distributions. Optimal fitting required four Gaussians using the following expression:

$$Y = w1*n(x;\mu 1,\sigma 1)+ w2*n(x;\mu 2,\sigma 2)+ w3*n(x;\mu 3,\sigma 3)+ w4*n(x;\mu 4,\sigma 4)$$

where w1, w2, w3, and w4 are weights, μ1, μ2, μ3, and μ4 are means, σ1, σ2, σ3, and σ4 are standard deviations for the 4 components respectively.

Statistical analysis

Correlations between measured parameters were assessed using Pearson's correlation coefficient. Correlations with survival data were identified by calculation of Spearman's correlation coefficient (assuming constant risk). These data were used only to provide comparison with other studies that employ this technique. Log-rank analysis was used to identify potential predictors of survival testing the hypothesis that: "the hazard rate for survival showed no significant difference across terciles of the variable". Values for Chi^2 were generated and compared to the critical value for each distribution. All analyses were adjusted for multiple comparisons using a Šidák correction. Cox proportional hazards modeling was used to study the effect on survival of variables that were significant in univariate analysis. Models were constructed using variable selection based on significance of individual parameters ($p < 0.01$) using a stepwise leave one out approach. Three models were constructed. Following model construction the performance was assessed by calculation of the Harrell concordance index (C; where a value of 0.5 indicates random performance and a value of 1.0 indicates perfect predictive power) [192]. Concordance indexes were then compared using the method described by Newson [193]. A jackknife data resampling technique was applied in calculating concordance indexes and their confidence intervals. Statistical analyses were performed using SPSS version 15.0 (SPSS Inc., Chicago, USA); Wizard Pro for the Mac (http://www.wizardmac.com/) and Stata version 11.1 (StataCorp, College Station, Tex).

Results

Patients

32 patients were initially recruited into the study between April 2006 and August 2008. Two patients initially recruited were excluded as they did not have GBM confirmed on histology (glial tumor, likely high-grade but not diagnostic of GBM) and 1 patient was excluded due to a non tumor-related death. Two patients were excluded as they were assigned to non-standard (palliative) therapy. Of the remaining 27 patients the median age was 61 (range 38-76) and 19 patients were male. Median survival was 202 days (range 62-1363). All patients had a KPS of > 80 at presentation. Patient information are summarized in **Table 5.1**.

Patient n.	Gender	Age	Survival (Days)
1	f	66	87
2	m	65	62
3	f	57	81
4	m	63	40
5	m	63	400
6	f	58	568
7	m	55	172
8	m	66	133
9	m	70	127
10	m	62	182
11	f	76	94
12	f	61	1363
13	f	53	1231
14	m	69	30
15	m	64	224
16	f	52	583
17	m	58	230
18	m	70	221
19	f	61	279
20	m	41	575
21	m	71	332
22	m	58	528
23	m	48	68
24	m	38	904
25	m	66	523
26	m	70	166
27	m	56	152

Table 5.1 Patient information

Do Centile Values of DCE-MRI Biomarkers Contain Additional Predictive Information compared to Median values?

Survival showed linear correlations with age ($R^2 = 0.41$; $p < 0.05$); $R1_{med}$ ($R^2 = 0.55$; $p < 0.003$); $R1_5$ ($R^2 = 0.64$; $p < 0.001$); $R1_{10}$ ($R^2 = 0.63$; $p < 0.001$); $R1_{20}$ ($R^2 = 0.61$; $p < 0.001$); $R1_{90}$ ($R^2 = 0.50$; $p < 0.05$); v_{e10} ($R^2 = 0.50$; $p < 0.01$) and v_{e20} ($R^2 = 0.42$; $p < 0.05$). Log-Rank analysis showed significant variations in hazard rates across quartiles for: age; tumor size, EnF%, $R1_{med}$, $R1_5$, $R1_{10}$, $R1_{20}$, $R1_{90}$ ($p < 0.01$), v_{e10}, v_{e20} ($p < 0.01$), $IAUC_{60med}$ ($p < 0.05$), $K^{trans}{}_5$ and $K^{trans}{}_{10}$ ($p < 0.05$).

Proportional hazard modeling demonstrated significant improvement in separation between the terciles of OS by v_{e20} compared to $ve_{\ med}$. Median values for the terciles defined by $v_{e\ med}$ were: 221, 166 and 224 days compared to 152, 182 and 230 days for the terciles defined by v_{e20}. Although percentile distributions of R1 ($R1_{med}$, $R1_5$, $R1_{10}$, $R1_{20}$, and $R1_{90}$) also showed significant variations on log-rank tests, the differences in separation of survival terciles were less striking. Proportional hazards models were constructed to compare comparative predictive power between median biomarker values and centile values showing increased predictive power in log-rank tests.

Model 1 included only median values of DCE derived parameters; age, $R1_{med}$, $v_{e\ med}$ and $v_{p\ med}$ provided the only independent statistically significant predictors (**Table 5.2**, **Fig. 5.1A**). The mean residual error was 2.93 days. Model 2 allowed inclusion of both median and centile values of parametric variables (**Figure 5.1B**); age, $R1_5$, v_{e20} and $K^{trans}{}_{med}$ were the only independent significant predictors (**Table 5.2**). The mean residual error was 2.37 days. The Harrell concordance indices for models 1 and 2 were $C = 0.76$ and $C = 0.83$ this difference was significant ($p < 0.05$).

Model	Variable	Coefficients	SE	Z score	Significance	Mean Residual Error in Survival (days)	Harrell Concordance Index
1	Age	0.103	0.031	3.342	<0.001	2.93	0.76
	$R1_{med}$	-0.047	0.018	-2.610	<0.001		
	ve_{med}	-0.056	0.020	-2.714	<0.01		
	vp_{med}	0.015	0.005	2.898	<0.01		
2	Age	0.093	0.036	2.584	<0.05	2.37	0.83
	$R1_5$	-0.056	0.025	1.676	<0.05		
	Ve_{20}	-0.090	0.040	-2,245	<0.01		
	K^{trans}_{med}	1.066	0.025	-2.79	<0.05		
3	Age	0.103	0.031	3.334	<0.001	1.65	0.88
	μ2	134.22	34.42	3.90	<0.001		
	σ3	44.95	12.98	3.464	<0.001		
	vp_{med}	-39.01	19.12	-2.041	<0.05		

Table 5.2 Results of multi-parametric proportional hazards models 1-3. The variable column shows all parameters with independent significant predictive value.

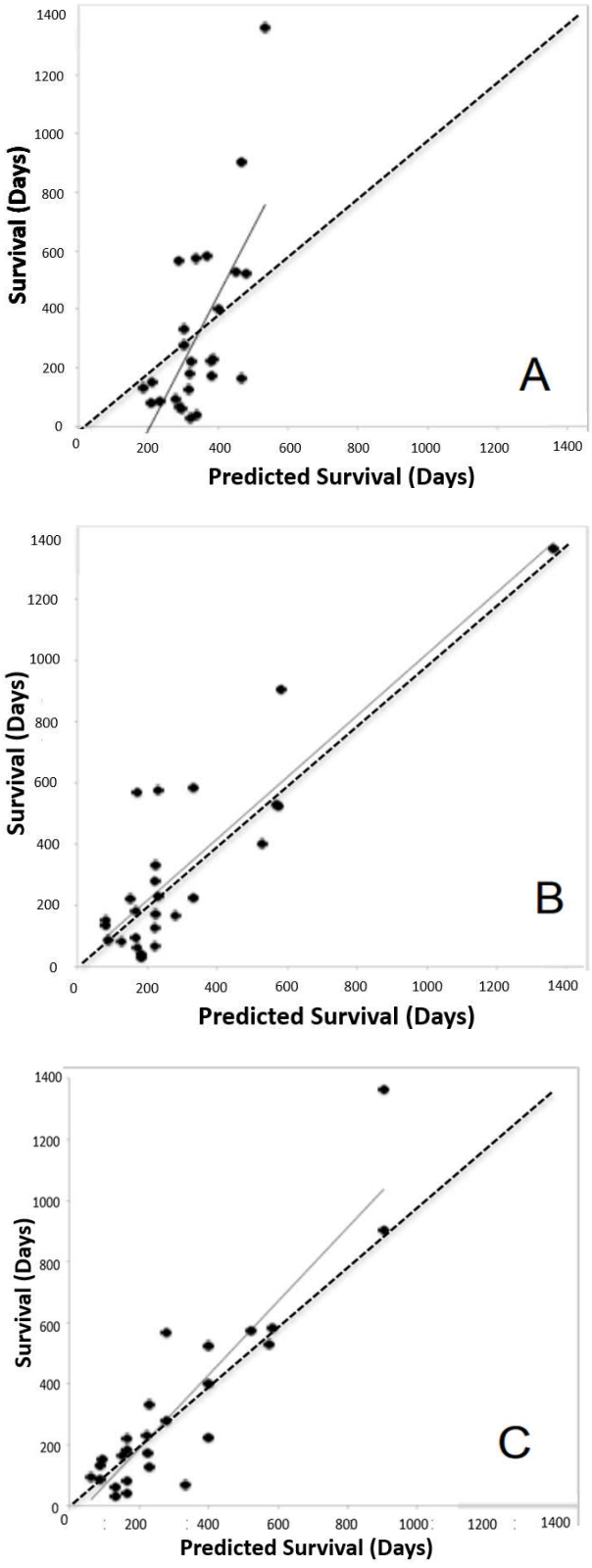

Figure 5.1 A-C Scatter plots of OS versus predicted OS from each of the three multiparametric proportional hazards models (1-3) shown in Table 5.1
Points represent individual cases. The dashed line shows the line of perfect agreement and the solid line shows the linear regression fit for the model.

Can Histogram Analysis Identify Tumor Regions Associated with Overall Survival?

Data analyzed using the extended Tofts and Kermode pharmacokinetic model [187] demonstrated strong correlations between median values ($R1_{med}$, $v_{e\ med}$, K^{trans}_{med}, $v_{p\ med}$) and each of their calculated centile values ($P < 0.001$). Significant correlations were also observed between K^{trans}_{med} and $v_{e\ med}$ and between their centile values. Data analyzed using the hybrid model [194] showed no correlations between individual parameters. R1 values conformed to a normal distribution. In contrast, histograms of v_e distributions showed subjective differences between the three survival groups.

Patients with long survival showed an almost bimodal distribution, whereas patients with short survival appeared to show the same two peaks but with an increasing number of pixels representing intermediate values (**Fig. 5.2**). Patients with short survival show an increasing proportion of pixels falling into the second and third Gaussian distribution (**Fig. 5.2**).

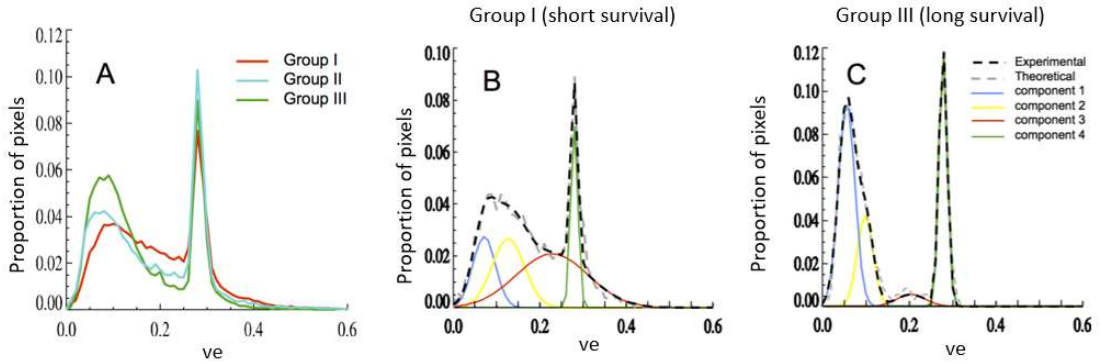

Figure 5.2 Comparison of histograms in patient grups with differents survival
A) comparison of the averaged v_e values from each of the three groups (I-III; short, intermediate and long survival). There is a clear bimodal structure seen in groups II and III whilst group I shows increased proportions of pixels lying between these two extreme distributions.
B) histogram showing the results of Gaussian fitting to the averaged data from group 1 (short survival). Note the relatively large contributions from tissue components 2 and 3. The dark dashed line demonstrates the combined v_e histogram for this group and the pale dashed line shows the summation of the fitted Gaussian model.
C) histogram showing the results of Gaussian fitting to the average data from group III (long survival).

Note the essentially bimodal distribution with relatively little contribution from components two and three.

Table 5.3 shows the mean value for each of the fitting parameters in the three survival groups. Correlation analysis showed significant correlations between σ3 and $R1_{med}$ and all centile values of R1 ($p < 0.001$). There was no significant correlation between median or centile values of v_e and any Gaussian fitting parameter. Significant intergroup differences were observed in μ2 ($p < 0.01$), W3 ($p < 0.01$) and σ3 ($p < 0.05$). The same parameters also showed significant linear correlation with OS: μ2 ($R^2 = 0.44$, $p < 0.001$), W3 ($R^2 = 0.26$, $p < 0.01$) and σ3 ($R^2 = 0.23$, $p < 0.05$).

grp	w1	μ1	σ1	w2	**μ2**	σ2	**w3**	**μ3**	**σ3**	w4	μ4	σ4
I (short)	0.0019	0.079	0.036	0.0024	0.130	0.043	0.0039	0.231	0.079	0.0018	0.284	0.011
	± 0.0015	± 0.015	± 0.016	± 0.0010	± 0.010	± 0.011	± 0.0022	± 0.024	± 0.023	± 0.0007	± 0.004	± 0.003
II	0.0024	0.067	0.023	0.0022	0.120	0.041	0.0019	0.219	0.053	0.0032	0.283	0.013
	± 0.0015	± 0.014	± 0.009	± 0.0012	± 0.004	± 0.010	± 0.0011	± 0.013	± 0.021	± 0.0017	± 0.003	± 0.007
III (long)	0.0027	0.068	0.026	0.0035	0.112	0.037	0.0010	0.201	0.037	0.0026	0.284	0.013
	± 0.0017	± 0.011	± 0.009	± 0.0022	± 0.014	± 0.018	± 0.0005	± 0.016	± 0.014	± 0.0013	± 0.004	± 0.004

Table 5.3 Gaussian fitting parameters averaged over three groups (I-III) showing short, intermediate and long survival

Log-Rank analysis showed significant variations in hazard rates across quartiles for all three parameters ($p < 0.001$). Proportional hazards modeling was performed using parameters selected as significant ($p < 0.1$) in univariate log rank tests from descriptive variables, mean DCE-MRI derived parameters (excluding v_e) and Gaussian fitting model parameters (model 3, **Fig. 1C**). Variables initially entered into the model were age, tumor size, R1, EnF%, K^{trans}, v_p, μ2, W3 and σ3. Age, v_p, μ2, and σ3 were the only independently significant parameters (**Table 5.2**). The mean residual error was 1.65

days. The Harrell concordance index was C = 0.88 and was significantly better than models 1 and 2 ($p < 0.05$). Histogram data from individual cases was used to identify each of the four components identified from Gaussian fitting. Thresholds are identified at the boundaries of the tissue types (ie a probabilistic Bayesian threshold used to segment at $p = 0.5$).

In group 1, only small areas of component two and three were identified. Typically, component three tissue was identified within the spatial distribution of a larger area of component two and these were seen predominantly adjacent to central areas of non-enhancement. In patients with short survival a much larger fraction of the tumor was represented by components two and three that were, typically, distributed throughout the enhancing component of the tumor (**Fig. 5.3**).

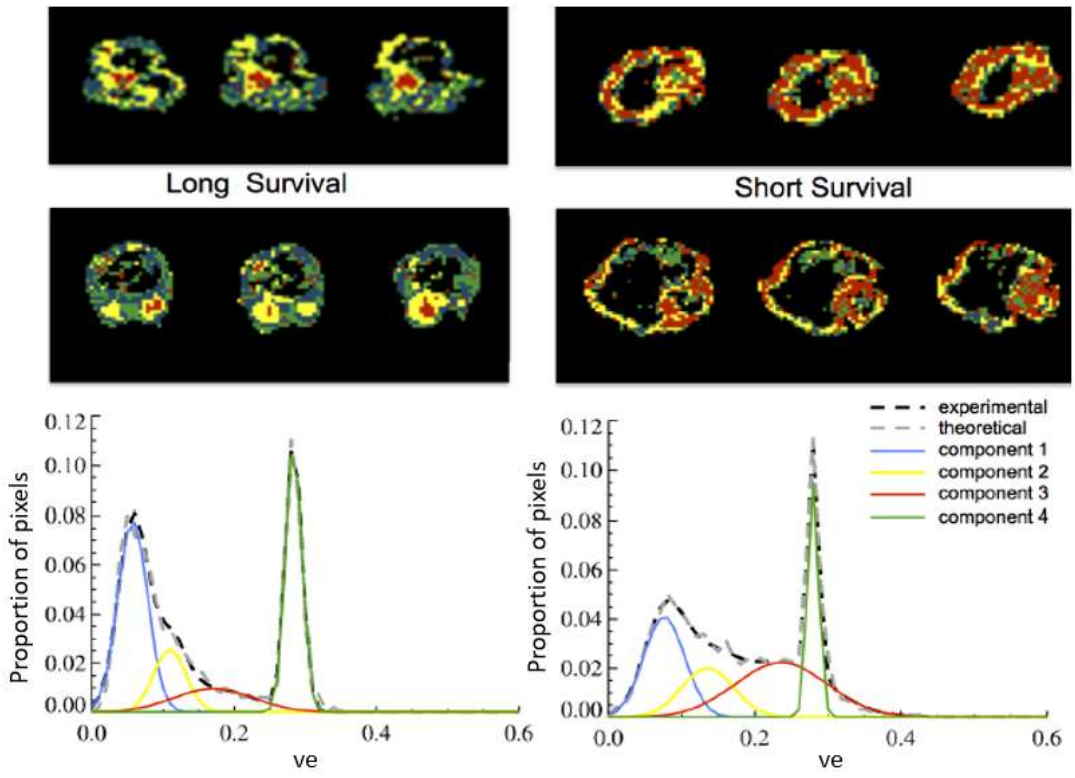

Figure 5.3 Parametric images showing the approximate anatomical distributions of components 1-4 in two patients with long survival (A) and two patients with short survival (B). The fitting histograms from the patient represented in the bottom image are shown in each case. Note that in the short survival patients areas of component three appear only within contiguous areas of component two and that these abut areas of non-enhancement. In short survival patients, components two and three are distributed throughout the solid enhancing component of the tumor.

Discussion

The data presented in this study confirms previous observations that, compared to simple median values, distribution properties of derived parameters can show significantly greater predictive power for OS. These data support the hypothesis that additional predictive information is provided by the use of centile values of distributions compared to the use of median values alone in agreement with Choi *et al*. who identified strong relationships between OS and low centile values of K^{trans} and the skewness of the distribution of v_e [182].

The prognostic significance of R1, which was seen in univariate logistic regression, is no longer seen in the multivariate regression, which incorporates the Gaussian fit and centile parameters. R1 is largely affected by the free water fraction within the tumor. In a recent study of vestibular schwannomas treated with anti-antiangiogenic therapy R1 was shown to be the most significant predictor of volumetric response and this was attributed to rapid reductions in endothelial permeability with associated decreases in intracellular oedema. Thus, tumors with the greatest oedema show the greatest volumetric response [194]. Decreases in R1 would therefore be associated with increases in extracellular extravascular space (EES) and consequently v_e. We believe that this expected biological correlation explains the loss of predictive activity of R1 in multivariate analyses in the current study.

Histograms of v_e contained clear structure, which varied between patients with long and short survival (**Fig. 5.2**). Subjective assessment demonstrated a bimodal distribution associated with long survival and an increase in the number of pixels lying between these distributions in patients with short survival. Gaussian fitting confirmed this and parameters from the second and third component demonstrated strong correlations with OS. Multivariate analysis showed that μ 2 (which represents

the mean v_e value of the second Gaussian component), and σ 3 (which represents the width of the distribution of the third component) became the most predictive imaging features whilst R1 measurements were no longer independently significant. The exact biological significance of v_e measurements is not entirely clear [195, 196]. Previous studies have shown some discriminative power between intra-axial and extra-axial tumors [197, 198] and a tendency to increase with increasing grade in glioma [197, 199] and a relationship between the kurtosis of the distribution and both OS and PFS[182]. In addition, v_e demonstrated sensitivity in identifying changes in response to treatment with corticosteroids, with decreases in v_e occurring following treatment, presumably reflecting a reduction in tumor oedema [200, 201].

Ludemann and colleagues described two independent contrast distribution spaces, characterized by rapid and slow leakage of contrast, suggesting that fast transport describes vessel permeability, whilst slow transport represents contrast diffusion occurring into "(micro)-necrotic tissue". They further identified a typical distribution of slow permeability components adjacent to necrotic areas supporting their hypothesis that these areas represent increasing micro-necrosis in areas of hypoperfusion [197, 199].

Our findings are in keeping with these observations and the development of fitting components two and three in the Gaussian model may therefore represent increasing development of micronecrosis although it may also represent development of a tumor habitat with an increase in EES for some other reason. The distribution of components two and three in patients with long survival shows a preferential location in large solid tumor masses and adjacent to the necrotic, non-perfused, core. Furthermore, component three is seen preferentially to be located within areas characterized as component two. In patients with short survival the distribution of

components two and three is far more extensive throughout the solid tumor mass and is not particularly characterized by location adjacent to necrotic areas, although involvement is so extensive in this group that it is difficult to judge this reliably. The major weaknesses of the current study are: 1) a small sample size and 2) the lack of recognized prognostic tissue biomarkers (MGMT, EGFR, IDH1), not available for analysis in this cohort. In addition, we have not compared the predictive power of identifying this tumor habitat with the predictive power from other known imaging biomarkers, particularly ADC. Although this does not invalidate the observation of the relationship between survival and the presence of habitats identified on the basis of v_e distribution, it will be essential both to confirm the observation in larger cohorts. Furthermore, it would be worthy to examine the relationship between molecular tissue subtype and associated prognostic tissue biomarkers and the presence and distribution of the tissue habitat identified here.

Conclusions

We have shown that accurate measurements of v_e, designed to reduce correlation with other DCE derived biomarkers, support identification of a distinct tumor habitat whose existence is related to survival. The distributions of v_e demonstrate a strong significant relationship to overall survival, even in this small patient group, and clearly warrant further investigation.

Chapter 6 Conclusions and Future Work

This thesis was focused on validating the measurability and reproducibility of certain putative imaging MRI biomarkers of tissue hypoxia in high-grade gliomas. Our investigations were concentrated on OE-MRI, QF measurements and DCE-MRI.

The studies presented in chapter 3 and 4 represent an improvement of OE-MRI understanding and demonstrate that R1 change, a commonly used biomarker of hypoxia, is reasonably predictable, measurable and reproducible in normal brain tissue and in high-grade gliomas and documented a relationship between increasing FiO_2 and CBF changes.

The last experimental part of the thesis (chapter 5) investigated, instead, the association between DCE-MRI derived parameters and tumor microenvironment demonstrating a correlation of the histogram of the extravascular extracellular space (v_e) with different imaging habitats and survival in patients with high-grade glioma.

Magnitude of R1 change in normal brain tissue

In healthy subjects we found significant percentage changes of mean R1 from baseline values in response to hyperoxia (FiO_2 = 100%) in CSF (suprasellar cistern CSF = 4.83%, C.I. = 3.059 – 6.56, $p < 0.001$, individual significant changes in all 14/15 scans). These %changes were barely significant in GM (0.438%, C.I. = 0.054 – 0.721, $p = 0.026$; individual significant changes in only 7 subjects) but not significant in WM. Our explanation for the absence of a compelling R1 change in response to hyperoxia in normal brain parenchyma relies on the relation between physiological reactive vasoconstriction of brain arteries (determining a progressive reduction of cerebral blood flow) at increasing concentration of administered O_2. A decrease of CBF under

hyperoxic conditions in healthy subjects has been previously reported [156, 202]. In addition, it is worth to mention that Xu *et al*. reported a decrease of global cerebral metabolic rate of O_2 by 10.3±1.5% and 16.9±2.7% for increasing levels of supraphysiological FiO_2 (50 and 98% in their study, respectively) in healthy participants [144].

The significant change of mean R1 in CSF (suprasellar cistern region) in response to 100% oxygen can be put in relationship with a diffusion process from plasma. Conversely, no significant changes at lower supraphysiological FiO_2 were measured in CSF, possibly suggesting a delicate balance between the O_2-induced vasoconstriction that is sufficient, up to certain levels of O_2 concentration, to mask the R1 effect of the O_2 diffusion from plasma, which becomes evident at 100% FiO_2. Additionally, CSF compartment may be considered as a large reservoir, where changes in oxygenation would need more time to occur [147].

In CSF of patients, similarly to our findings in healthy subjects, we detected significant response of mean R1 to pure oxygen; however, %change in response to hyperoxia in GM and WM resulted higher in patients than in volunteers. Noteworthy R1 change in brain parenchyma of patients resulted more convincing, with significant changes in almost all cases for GM. As for healthy participants, R1 change in WM was not compellingly significant.

The discrepancy of mean R1 %change in GM between healthy volunteers and patients can be explained due to at least a damaged cerebral blood flow regulation [203]. The stability of CBF is regulated by three key paradigms: cerebral pressure autoregulation, flow-metabolism coupling and a widespread network of perivascular nerves (the so-called neurogenic regulation). In these three physiological models a key role is played by endothelial cells and astrocytes [204]. In this regard, Sharma *et al*. reported a larger

tumor size (100 ± 32; range = 89-265 cm^3) in patients with impairment of autoregulation compared to patients without impaired autoregulation (40 ± 8; range = 7-136 cm^3; p = 0.002)[205].

Discrimination of successful and unsuccessful O_2 delivery in subjects undergoing OE-MRI

In patients undergoing OE-MRI, we documented a %change in mean R1 of suprasellar cistern CSF under a FiO_2 of 100% comparable to that observed in healthy volunteers. Indeed the cut-off of mean R1 change (1.40%), identified in volunteers (chapter 3) discriminating between administrations of 100% O_2 from air, proved in patients an almost identical diagnostic performance (sensitivity = 95.83% and specificity = 100%) in identifying the tightness of the gas delivery system (and consequentially successful 100% O_2 delivery to the patient respiratory system).

Influence of pre-exposure to high supraphysiological FiO_2 on CBF change and R1 change in brain tissue

In normal volunteers, we documented significantly higher R1 change in suprasellar cistern CSF and significantly larger decrease of CBF in response to 100% oxygen when exposure was preceded by high supraphysiological FiO_2 (60% in our experiments) rather than air. This suggests that CSF needs prolonged administration of high FiO_2 compared to other tissues and that 100% FiO_2, does not allow a complete diffusion process of O_2 to reach the maximal saturation, at least according to our experimental OE-MRI protocol. An important impact of pre-exposure was surprisingly observed also in CBF; we are not aware of similar findings in literature. We postulate that PaO_2 in CSF may drive decreases in CBF resulting from supraphysiological FiO_2.

Time course of R1 change in normal brain tissue

In normal brain parenchyma of healthy volunteers, the onset of significant mean R1 change over our prefixed threshold occurred reasonably rapidly after the administration of pure oxygen (within 120 sec in 10/12 volunteer scans with significant changes in GM) with an apparently slower drop to the baseline level at return to air. Likewise, this trend (surpass of the threshold faster than return to baseline level) was also confirmed in suprasellar cistern CSF. Considering a negligible delay for O_2 to travel through the gas circuit and reach the patient respiratory system, this timing appears coherent with the on-transient (within approximately 30 sec) and off-transient (within approximately 80 sec) responses of cerebral vasculature in normal brain to isocapnic hyperoxia reported by Steinback *et al.* [206]. These findings possibly suggest higher sensibility of R1 change to acute hyperoxia rather to acute hypoxia.

Magnitude of R1 change and time course in brain tumor tissue

Also response of brain tumor regions to hyperoxia has to put in relationship to tumor blood flow, oxygenation status, and metabolism [207]. Within tumor tissue, it is likely that O_2 does not determine vasoconstriction due to abnormal behaviour of pericytes and smooth cells [208].

As expected, R1 change resulted lower and slower in the non-enhancing core compared to enhancing regions of the tumor underlining a weaker O_2 diffusion.

Reproducibility of R1 change in normal brain and tumor tissues

From our analysis, R1 measurement appears sufficiently reproducible to be used in both normal and tumor tissues. The R1 change demonstrates a comparable rise in response to hyperoxia and drop after cessation of the administered O_2. R1 appears therefore a candidate biomarker for serial measurements. Diffusion processes may

influence also reproducibility; in accordance to this postulate, the lowest reproducibility was shown in non-enhancing tumor regions.

Histogram analysis of extravascular extracellular space data from DCE-MRI in glioblastoma provides a potential imaging biomarker of micro-necrosis, related to survival

The last chapter has demonstrated the possibility of identifying different imaging habitats and predicting survival by means of histograms of a DCE-MRI derived parameter (v_e) generated using a mixture of Gaussian functions. Patients with short survival presented the presence of higher percentage of pixels positioned between the second and third Gaussian distribution of the v_e histogram, whereas a clear bimodal distribution of v_e was documented in patients with long survival.

Although histological tissue data were not analysed in this study, v_e may represent an imaging biomarker of micronecrosis. In support of this hypothesis, Egeland *et al.* have reported in a preclinical study, including three amelanotic human melanoma xenograft lines, different v_e frequency distributions in necrotic tissue compared to viable tissue [163]. In particular, voxels with unphysiological v_e value (> 0.15 in this study) correlated with necrotic fraction in histological tissue. Another group, instead, reported a correlation between v_e and tumor growth, possibly related to larger tumor extracellular space and oxygen consumption [209].

Future work

In terms of future work, we aim to analyse the reproducibility of the OE-MRI signal at the voxel levels in normal brain tissue and tumor lesions. A technical aspect that could need to be investigated would be the influence of the magnitude of field of MRI on the magnitude of change and reproducibility of the signal. Furthermore, another

aspect to be implemented in the OE-MRI protocol will be the evaluation and correction of the image noise.

In the present thesis we did not acquire data of ICA flow changes in patients with brain tumors in response to increasing FiO_2; these data would be of paramount importance to validate some of our hypotheses generated by the presented studies and provide further understanding on the relationship between FiO_2 and brain flow.

We aim also to correlate our DCE-MRI findings (chapter 5) in patients with high-grade gliomas with hypoxia markers in previously collected histological tissue.

Furthermore, a future development of my research will be the biological validation of OE-MRI and [^{18}F]FAZA PET. A study, funded by the Cancer Research UK (CRUK) and entitled "Biological Validation of MRI and PET Biomarkers of Tissue Hypoxia in Glioblastoma Multiforme" (see Appendix A), is currently recruiting patients with high-grade glioma awaiting surgery. Study participants undergo our validated MRI research protocol and [^{18}F]FAZA and [^{15}O]H_2O PET scans. On the day of surgery, patients receive pimonidazole tablets; in addition, biopsies, based on hypoxia imaging, are collected. The main goal of this study is to cross-validate the imaging methods and provide a comparison with histological evaluation of hypoxia by means of the pimonidazole distribution in tumor samples. Furthermore, we intend to develop optimized acquisition and analysis strategies for the use of [^{18}F]FAZA PET in cerebral tumours and elucidate the relationship between imaging biomarkers of hypoxia, cerebral blood flow and biomarkers of microvascular structure derived from [^{15}O]H_2O and DCE-MRI.

The study is currently recruiting patients at the weekly multidisciplinary team discussions (MDTs) held at the Neurosurgery department at Salford Royal NHS Foundation Trust (SRFT), whereas the imaging part of the projects is being conducted

at the Wolfson Molecular Imaging Centre (WMIC). At the moment, 6 patients have undergone the research protocol. The image analysis pipeline is still under development.

Appendix A Research protocol Version 2.0 (23/11/2015): Imaging Hypoxia in Cerebral Tumours

Project title:

Biological Validation of MRI and PET Biomarkers of Tissue Hypoxia in Glioblastoma Multiforme

Study Protocol

Chief investigator: Prof Alan Jackson

Co-investigators: Dr Natale Quartuccio, Dr Marie-Claude Asselin, Dr David Coope, Dr Neil Thacker, Dr Erjon Agushi

Aims of the study

1. To provide biological validation of a novel imaging technique: oxygen-enhanced Magnetic Resonance Imaging (OE-MRI), for the evaluation of tumour hypoxia in patients with high grade glioma.
2. To provide biological validation of [^{18}F]Fluoroazomycinarabinofuranoside ([^{18}F]FAZA) or [^{18}F]Fluoromisonidazole ([^{18}F]FMISO) as a potential biomarker of hypoxia in patients with high grade glioma.
3. To develop optimized acquisition and analysis strategies for the use of [^{18}F]FAZA or [^{18}F]FMISO in cerebral tumours.
4. To elucidate the relationship between imaging biomarkers of hypoxia, cerebral blood flow and biomarkers of microvascular structure derived from [^{15}O]H_2O and DCE-MRI.

Introduction and Background

Glioblastoma multiforme (GBM) is the highest grade (IV) glial cell tumour and accounts for 80% of all primary brain malignancies [1]. The incidence of GBM, which has currently increased over the last decades, is around 3-5 new cases per 100.000 in Europe and the US, with 18 cases per 100.000 for individuals over 65 year [1-3]. However, despite recent progress in treatment, prognosis still remains very poor, with an overall survival (OS) of 14.6 months [2]. Due to the common development of the tumour in young adults, it is the largest cause of years of life lost of any cancer type. Tumour hypoxia is one of the main histological hallmarks of GBM although it appears to vary between patients and shows significant variations within individual tumours [4-5]. Tumour hypoxia represents a crucial factor in determining the invasiveness of GBM and has been associated with amplified resistance to radiotherapy, chemotherapy and with worse outcome after standard of care therapy [6-7].

The relationship between tissue hypoxia, treatment resistance and decreased survival has raised the possibility of improving outcome by targeting novel therapeutic approaches to the hypoxic component

of the tumour. This may be addressed by the use of hypoxia reversal strategies in combination with conventional chemo-radiotherapy or by the use of novel cyto-reductive agents that are specifically taken up by, and toxic to, hypoxic cells. The recent failure of antiangiogenic therapies to improve overall survival in patients with GBM, despite dramatic reductions in tumour perfusion and apparent tumour size, has also led to recognition of the importance of therapeutic resistance mechanisms. The presence of significant tissue heterogeneity within individual tumours, together with the need to target hypoxic areas using surgery or radiotherapy, has led to increasing demands for effective imaging biomarkers of tissue hypoxia. Despite extensive research no suitable imaging biomarker of hypoxia yet exists [7].

The most common approach for imaging regional hypoxia has been the use of radiolabeled nitroimidazole compounds combined with positron emission tomography (PET) imaging. The most widely used of these radiotracers has been [^{18}F]FMISO although only a handful of clinical studies have been performed in cerebral tumours [8]. However, [^{18}F]FMISO suffers from low tumour uptake, high uptake into normal brain and, surprisingly, there is no actual biological validation of its ability to detect tissue hypoxia in cerebral tumours [8-9]. [^{18}F]FAZA is an alternative PET hypoxia tracer that provides a number of potential advantages. Its lower lipophilicity yields a much higher tumour uptake relative to the background brain tissue attributable to its faster clearance and, more importantly, to its limited ability to cross the intact blood-brain barrier, resulting in superior contrast to [^{18}F]FMISO. It has undergone preliminary assessment in cerebral tumours [8], but breakdown of the blood-brain barrier in GBM may confound the interpretation of this radiotracer for hypoxia imaging in this tumour type.

Although a number of MRI-based methods have been applied to the study of tumour hypoxia, none has proven satisfactory. The use of dynamic contrast-enhanced MRI (DCE-MRI) allows measurement of microvascular characteristics, but it has been shown that significant areas of perfusion/hypoxic tissue mismatch exist when DCE-MRI is compared to [^{18}F]FMISO PET [10, 11]. Similarly, the use of blood oxygen level dependent (BOLD) imaging has been described but is complicated by the presence of blood products in the tumour and, although regional hypoxia can be inferred by the response to inspired oxygen, it does not provide a reliable indication of the presence of hypoxic tissue or the severity of hypoxia [12].

OE-MRI exploits the weak paramagnetic nature of oxygen. OE-MRI was first validated for the evaluation of regional ventilation in lung [13, 14]. Afterwards, pioneer studies by The University of Manchester, published in 2009 and 2014, demonstrated the feasibility of visualizing tumour hypoxia in a mixed group of solid tumours [15] and in brain tumours [16]. OE-MRI employs a hyperoxic challenge. The patient, lying in the MR scanner, inhales 100% oxygen via a face mask or non-rebreathing circuit [17]. Molecular oxygen acts as a contrast agent increasing the longitudinal relaxation rate (R1) of water. Changes in R1, due to hyperoxic breathing, are thought to be proportional to changes in tissue oxygen concentration, and allow identification of hypoxic tissue [15]. Initial pre-clinical and small-scale clinical studies have shown considerable promise for this technique [15-16].

Ongoing preclinical validation studies (unpublished observations) continue to show close agreement between tissue hypoxia and OE-MRI signal change. At the present time, this represents the most promising method for clinical imaging of regional tissue hypoxia although there is a clear need for extensive biological validation before it can be applied in clinical studies. Furthermore, to date, no trial has ever validated the utility of OE-MRI in patients with high-grade gliomas and correlated its findings to those from other complementary imaging modalities and to the histological features of GBM by means of pimonidazole, the gold-standard for the histological detection of tumour hypoxia.

Objectives

Primary objectives

- To provide biological validation of OE-MRI by comparison with tissue markers of hypoxia.
- To provide biological validation of [^{18}F]FAZA or [^{18}F]FMISO PET by comparison with tissue markers of hypoxia.

Secondary objectives

- To optimize image acquisition protocols for [^{18}F]FAZA or [^{18}F]FMISO PET.
- To elucidate the relationship between imaging biomarkers of hypoxia, cerebral blood flow and biomarkers of microvascular structure derived from [^{15}O]H_2O and DCE-MRI.

Experimental Design

Patient recruitment

This is a prospective pilot study. Potential participants will be recruited through the Neuro-oncology multidisciplinary team (MDT) and screened at Salford Royal NHS Foundation Trust (SRFT) with the collaboration of Dr David Coope (Clinical lecturer and honorary registrar in neurosurgery – The University of Manchester), who has access to the hospital patient database. Potential participants will be approached immediately after the pre-surgical visit; a member of the direct healthcare team will the patient if he/she is interested in getting information about the study. Only if the patient is keen to receive information, there will be a conversation with the clinical research fellow, Dr Natale Quartuccio, or other designated clinical staff, who will explain the study with its risks and will verify the required inclusion criteria. Patients will be provided with a full verbal and written explanation of the study (patient information sheet).

Inclusion criteria

1. Patients with brain lesion compatible with newly diagnosed glioblastoma multiforme and/or recurrent grade 3 glioma with secondary resection planned.
2. Age: 18 years or older.
3. Capability to receive and understand verbal and written information regarding the study and give written informed consent.
4. Ability to lie still for two one hour scanning sessions.

Exclusion criteria

1. Patients with contraindications to MRI scanning (e.g. pacemaker, heart valve replacement, metal implants not approved for MRI, neurostimulators, claustrophobia), history of contrast (gadolinium) or radiotracer allergy.
2. Karnofsky Performance Score < 60.
3. If the patient has not received MR contrast agent in the previous six months or if there is a history, which could be related to poor renal function or recurrent renal infections, then renal function will be estimated. Where possible this will be obtained from the patient's clinical notes and preoperative assessment, otherwise it will be specifically measured. A finding of estimated glomerular filtration rate (eGFR) < 30 mL/min/1.73m^2 will exclude the patient from the study.
4. Patients not suitable to undergo PET or MRI, due to weight greater than 157.50 kg (the weight limit for the MRI and PET tables).
5. Female patients: pregnancy. This will be assessed at Wolfson Molecular Imaging Centre (WMIC) – The University of Manchester by trained staff according to the standard operating procedure (SOP) to establish pregnancy and breastfeeding status.
6. Presence of any other coexisting condition which, in the judgment of the investigator, might increase the risk to the subject.

Consent process

Patients meeting the inclusion criteria and willing to participate in principle to the study will be asked by the investigator or authorized personnel to sign a provisional booking form at the time of the conversation which will allow the transfer of personal data to help schedule the imaging scans. Patients will be contacted by telephone the following day, at least 24 h after the first conversation, by the clinical research fellow or authorized personnel to see if, after consideration, they still wish to remain involved in the study. If still agreeable, then appointments for imaging scans will be booked.

On the day of attendance the patient will be asked to sign the study consent form for enrolment into the study. This form will make it clear that the patients will have a subsequent opportunity to withdraw from the study without any impact on their care. The reasons for this consent

process (provisional booking form and study consent form) are purely logistic; the manufacture of the PET tracers cannot be undertaken without a signed form to confirm that personal details may be transferred to The University of Manchester. Since many patients travel from a considerable distance, the provisional booking form allows radiotracers production without the patient being inconvenienced by requiring a second visit only to obtain signed consent.

Timing of the Scans

The scans will ideally be done on Friday of the same week as the interview or Monday of the following week at WMIC so that results can be sent to the Neuro-oncology MDT at SRFT for the Tuesday meeting for further discussion and evaluation of the case and to allow time for image-based planning of the surgical biopsy procedure. Ideally, the PET and MRI scans will be done on the same day (in the morning and in the afternoon, respectively) in order to limit inconvenience for the patient. If, for any unforeseen reason, this is not feasible, the scans will be done on separate days.

Design of the study

Up to 30 patients will be recruited in order to collect complete datasets for OE-MRI, PET and surgical biopsy in a minimum of 12 patients. In order to avoid unnecessary radiation exposure and risk to patients, we have included an interim analysis of the performance of [^{18}F]FAZA PET after the acquisition of six complete datasets. If the radiotracer accurately reflects tissue hypoxia, demonstrated by histology, the initial cohorts will be expanded. If the radiotracer does not reflect hypoxia, it will be substituted with [^{18}F]FMISO. If neither PET tracer proves effective in the interim analysis, then the study will continue with OE-MRI alone. This results in two potential patient cohorts:

Cohort 1 – Six patients will be scanned using [^{15}O]H_2O and [^{18}F]FAZA PET and OE-MRI. Tissue will be collected for histology and genetic analysis. An interim analysis will then be performed to compare the uptake ratios of [^{18}F]FAZA with the tissue markers of hypoxia, evaluated by immunohistochemistry. If [^{18}F]FAZA uptake shows correlation with tissue hypoxic markers in the first cohort of six patients, then an additional six patients will be recruited with the same protocol.

Cohort 2 – If [^{18}F]FAZA alone fails to show a correlation with tissue hypoxic markers in the first six patients of cohort 1 and is clearly not acting as a marker of hypoxia, then [^{18}F]FAZA will be substituted with [^{18}F]FMISO and additional patients will be recruited to provide a minimum of 12 patients with complete datasets for OE-MRI, PET and surgical biopsy.

Subjects who are recruited and withdraw from or do not complete the entire planned protocol for a given cohort will be replaced.

Imaging

Preliminary procedures

The patients will be contacted by Dr Quartuccio or other designated clinical staff involved in the study to explain again the scanning procedures, potential risks of the research study and provide answers to any additional questions regarding the research protocol.

At their arrival for the imaging session, patients will be received and any outstanding question addressed. Consent will be sought and the patient will be asked to sign the study consent form. The patient will be taken to the scanning suite and radial arterial and venous lines will be inserted by qualified staff. The arterial line will be placed ideally in the non-dominant radial artery under local anesthesia and after a successful modified Allen's test to evaluate ulnar artery patency [18]; if this attempt fails, placement will be tried in the dominant side. Arterial line will subsequently be used to take samples of arterial blood (details in the next section) during the [^{15}O]H_2O and [^{18}F]FAZA or [^{18}F]FMISO scans to generate the arterial input function, which is essential for an accurate estimate of cerebral blood flow using pharmacokinetic modelling. PET scanning will not go ahead without arterial cannulation. A venous line will be also inserted in the antecubital vein on the opposite side and used to inject the radiotracers and the MR contrast agent.

PET

Patients will be positioned supine with their head inside a dedicated brain PET scanner (Siemens HRRT, Knoxville, TN) and will wear a neoprene swim cap with a tracking tool on its top which will be used by an optical measurement device to measure the position and orientation of the subject's head over the course of the scans with minimum discomfort for the patient. The tracking tool will be tracked relative to a second tool attached to the scanner gantry.

Authorized staff will perform all PET scanning procedures. A bolus of [^{15}O]H_2O (maximum radioactivity injected: 740 MBq for both male and female) will be injected in the antecubital vein by an automated injection system with both pre- and after-flush of an inert saline solution. Shortly before radiotracer injection, an automated blood sampler will be started, programmed to withdraw blood continuously over approximately 7 min. Three additional arterial blood samples will be taken at discrete times for cross-calibration with the PET scanner. Approximately 10 min (5 half-lives) after the start of the [^{15}O]H_2O PET scan, the patient will receive a bolus of [^{18}F]FAZA (maximum radioactivity injected: 555 MBq and 415 MBq for male and female, respectively) or [^{18}F]FMISO (maximum radioactivity injected: 555 MBq and 515 MBq for male and female, respectively) through the venous line and dynamic image acquisition will be performed for 60 min; arterial blood will be sampled, continuously by the automated blood sampler for approximately 16 min and additional discrete arterial blood samples will be withdrawn throughout the PET scan. The patient will have a rest period outside the PET scanner (30 min for [^{18}F]FAZA and 60 min for [^{18}F]FMISO) following which a second dynamic 60-min acquisition will be performed. Additional discrete arterial blood samples will be

collected during this scan. A maximum of 200 ml of arterial blood will be sampled in total from the patient.

The patient will be removed from the PET scanner and the arterial line removed. The patient will then be allowed to rest in the clinical area for about an hour during which period he will be provided with food and drink.

MRI

After the PET study, the patient will undergo MR scanning. Patients will be given a face mask or a mouthpiece (possibly along with a nasal clip) to breathe through so that the inspired oxygen concentration can be controlled. Initially, at the start of the MRI scanning the patient will receive medical air. The MR protocol will include:

1. Anatomical sequences for segmentation of tumour and normal tissue.
2. Baseline images for calculation of R1 using inversion recovery images with varying inversion times.
3. Dynamic T1-weighted OE-MRI series lasting 10 minutes during which the administered gas will be changed to 100% oxygen.
4. Images for calculation of R1 using inversion recovery images with varying inversion times.
5. Dynamic T1-weighted OE-MRI series lasting 10 minutes during which the administered gas will be changed to medical air.
6. Diffusion weighted images for measurement of tumour cell invasion into normal tissue.
7. Dynamic contrast enhanced MRI using dynamic T1 acquisitions.
8. Dynamic contrast enhanced MRI using dynamic T2* acquisitions.
9. Post contrast T1-weighted image for surgical planning

The MRI protocol will last approximately an hour.

Surgery and tissue collection

Before the planned surgery, at SRFT, a single dose of pimonidazole will be administered orally to the patient by trained staff. Pimonidazole will help us in the validation of hypoxia imaging allowing a correlation of imaging data with presence of hypoxia at a histological level. The oral formulation of pimonidazole will be prescribed by the healthcare team and dispensed by the hospital pharmacy. At surgery, biopsy samples will be acquired by experienced neurosurgeons using frameless stereotaxy with the Brainlab Varioguide (BrainLAB AG, Feldkirchen, Germany). The BrainLab Varioguide will provide an accurate and safe biopsy procedure. Only tissue which is planned to be subsequently resected will be biopsied; any tissue injury resulting from the biopsy will therefore only occur in regions to be resected in the same operation. Navigation points will be planned by Dr Coope at least the day before surgery using the software system Vinci (Max Planck Institute for Neurological

Research, Cologne, Germany). This process has been used successfully in previous studies at this centre. Targets will be defined on the basis of hypoxia PET imaging, using tumour-to-brain ratios estimated on the summed images of the second scan. The targets will be approved by the treating neurosurgeon at the neuro-oncology MDT.

Targets will be transferred to the BrainLab planning system, which allows co-localization of MRI slices with hypoxia PET imaging. The biopsies will be collected through a standard single 14 mm burr-hole prior to elevating the bone flap for the subsequent surgery in order to minimize brain shift. Tissue samples will be taken at up to 4-points from a single tract collecting 4 cores at each point.

The tissues collected will include:

1 An area of apparent hypoxia.

2 An area of apparently non-hypoxic viable tissue.

3 If possible, an area at the tumour edge where it extends into oedematous tissue, as long as this area has been planned to be included in the surgical field.

The locations from which tissue samples are taken will be recorded using a custom-logging module implemented in the 3D Slicer interfaced with the clinical Brainlab system. Tissues will be collected in sterile pots, separately labeled with the labels prepared the day before to identify the site of biopsy. At resection, additional tissue will be taken for genetic testing and tumour subtype if this is required at a later date.

Trained personnel will transfer tissues to the Neuropathology Department where they will be stored as frozen samples.

Tissue storage

Tumour tissue and blood samples (one for each patient) will be collected and stored at The University of Manchester in a dedicated freezer for biological tissues. After the end of the study the samples will be donated to the Manchester Cancer Research Centre (MCRC) Biobank at the Cancer Research UK (CRUK) Manchester Institute. A suite of standard Patient Information Sheets and Patient Consent Forms have been developed and approved and informed patient consent will always be obtained in this study before patient samples are taken and utilized.

Tissue-based analysis

Tissue analysis will consist at least of staining for pimonidazole, carbonic anhydrase IX (Ca IX), hypoxia-inducible factor 1-alpha (HIF-1α), vascular endothelial growth factor 1 (VEGFR-1) and assessment of other relevant histological characteristics.

Further tissue will be stored for possible future genetic analysis and animal research, for which appropriate ethical consent will be sought. DNA and RNA will be extracted from frozen tissue samples and RNA sequencing (RNASeq) will be performed to correlate hypoxia-related gene expression with hypoxia imaging findings and to potentially identify a hypoxia gene expression

signature more widely applicable to GBM. We will seek additional funding to perform whole exome sequencing (WES) analysis of extracted DNA, at least in a subset of patients, to identify mutations associated with different histological subtypes and hypoxic patterns. Blood samples, collected on the day of the imaging session, will be used to extract circulating free DNA (cfDNA) which will be sequenced to provide exploratory data for the development of liquid biopsy options for identifying hypoxia or GBM-specific mutations. Tumour samples from patients will be used to derive patient-specific cell lines and cancer cells will be implanted in immunocompromised rodents in order to obtain patient derived xenografts (PDX); peripheral blood circulating tumour cells extracted from patient blood samples will be used to establish cell-derived xenografts (CDX); these xenografts will be used to further elucidate the molecular heterogeneity related to hypoxia.

Statistical and imaging analysis

General statistics

The assessment of the data obtained in this study will be the responsibility of Dr Natale Quartuccio, under the supervision of Dr Neil Thacker, who is one of the academic supervisors of the clinical research fellow.

Summary statistics will be provided for patient demographics. For each continuous quantitative variable, descriptive statistics (mean, standard deviation, median, and range) will be calculated. For categorical variables, the frequency and percentage in each category will be displayed.

Imaging analysis and regions of interest

Analysis of [^{15}O]H_2O PET images

Cerebral perfusion (in ml/min/cm^3) will be estimated from the dynamic images using the delay and dispersion-corrected arterial blood input function and the standard one-tissue compartment model. Perfusion values will be calculated at the voxel level (parametric maps) and in different regions of interest (ROI) in the tumour identified using MR and [^{18}F]FAZA and/or [^{18}F]FMISO PET images.

Analysis of [^{18}F]FAZA and/or [^{18}F]FMISO PET images

[^{18}F]FAZA and/or [^{18}F]FMISO tissue time-activity curves (TACs) will be analyzed using various kinetic models. The kinetic parameters will be compared against semi-quantitative parameters: tumour-to-blood and tumour-to-background (contralateral side) ratios. ROIs will be delineated on presumably hypoxic and non-hypoxic areas of the tumour for the calculation of hypoxic volume and hypoxic fraction.

Analysis of OE-MRI images

According to methodology described in previous studies by our groups [15, 16], a ROI will be manually drawn around the entire tumor for each patient based on pre- and post-contrast T1-weighted

and the T2-weighted anatomical images.

R_1 on O_2 breathing ($R_1(O_2)$) and ΔR_1 (R_1 on O_2 breathing minus R_1 on air breathing) will be calculated for each voxel.

Based on its T1-weighted OE-MRI data, each voxel will be classified into one of the three OE-MRI-derived groups: R_1-increasing, R_1-decreasing, or no significant change, using *t*-statistic maps of ΔR_1 after the switch from medical air to oxygen.

Analysis of DCE-MR images

Image analysis will be performed using validated pharmacokinetic analysis techniques. For the DCE-MRI, T1-weighted signal intensity over time will be converted to changes in tumour R_1, using standard methods already employed in studies by our group [15,16]. Changes in R_1 will be related to changes in contrast agent concentration for each tumor voxel using in-house software. The initial area under the contrast agent concentration–time curve post-injection ($IAUC_{Gd}$) will be calculated. In addition, the kinetic parameters of the extended Tofts model will be estimated on a voxel-by-voxel basis.

DSC imaging will be analyzed in-house using standard techniques to determine Cerebral blood volume (CBV), contrast arrival time and Cerebral Blood Flow (CBF) in ml/100 g/min.

Analysis of diffusion weighted MR images

The diffusion acquisitions will be analyzed using in-house software to produce apparent diffusion coefficient (ADC) by fitting the single exponential diffusion equation to the average diffusion weighted imaged with different B values derived from the multiple gradient directions obtained. Fractional anisotropy (FA) maps will be determined from the Eigen values of the diffusion tensor determined from 6 gradient directions and the b zero image. Tumour cell invasion will be assessed by calculation of the disparity between isotropic and non-isotropic diffusion and by calculation of the ADC translational coefficient.

Relationship between OE-MRI and DCE-MRI

T1-weighted OE-MRI data will be combined and then parcellated into statistically significant R_1-increasing and R_1-decreasing voxels. The average DCE-MRI time courses will be determined for these two groups of voxels to investigate any differences in contrast agent uptake (reflecting changes in perfusion capillary permeability and leakage space) between the putative well-oxygenated and hypoxic regions. The median values of AUC_{OE} and $IAUC_{Gd}$ will be calculated for each tumor, as the volume fractions of each tumor that show positive and negative $\Delta R_1(t)$ under oxygen inhalation.

Relationship between [^{18}F]FAZA and/or [^{18}F]FMISO and [^{15}O]H_2O PET images

Pixel-by-pixel correlations between [^{15}O]H_2O and [^{18}F]FAZA and/or [^{18}F]FMISO images will be assessed to evaluate the relationship between hypoxia imaging and different patterns of tumour perfusion derived from [^{15}O]H_2O PET.

Relationship between hypoxia imaging and histology

Tumour hypoxia will be determined as the percentage of the section area that stained positively for pimonidazole and other biomarkers of hypoxia in tumour samples. Relationships between the imaging data (OE-MRI and [^{18}F]FAZA and/or [^{18}F]FMISO PET) and the histological data will be assessed using Pearson's correlation coefficient.

Ethical aspects

The study will be conducted in accordance with the ethical principles of the Declaration of Helsinki of 1996.

Patient information and consent

Consent will be obtained by the principle investigator (PI), coinvestigators or designated, clinically qualified, members of the study team. The investigators or authorized personnel (nurses or clinicians) will explain the nature of the study, its purpose and associated procedures, the expected duration and the potential risks of participation to each patient before entry into the study (i.e. before examinations and procedures associated with selection for the study are performed). By signing the consent, the patient will allow the research team to access his medical history, biopsy samples, imaging data and any other data related to the research study for the purpose of the study. By signing the consent, the patient agrees for scans, blood samples, tumour tissues already collected to be retained and used in the study if he/she withdraws the consent (or if he/she is withdrawn by the research team). The patient will be asked to consent that data, tissue, imaging and medical records derived from the present research project may be reused by our Centre or other Centres for reanalysis or future studies including genetic analysis and animal research. Each patient will have ample opportunity to read the information sheet, ask questions, and discuss with relatives/friends and will be informed about the right to withdraw from the study at any time without any disadvantage and without having to provide reasons for this decision. Potential participants will have at least 24 hours to consider taking part in the study. Staff authorized to obtain consent are trained and experienced in discussing studies with oncological patients and all have good clinical practice (GCP) training. The reasons for the consent process adopted in this study (provisional booking form and study consent form) are purely logistic; the manufacture of the PET radiotracers cannot be undertaken without a signed form confirming that the potential participant's personal details can be transferred to The University of Manchester. Since many patients travel from a considerable distance, the provisional booking form allows radiotracer production to occur without the patient being inconvenienced by requiring an additional visit only to obtain signed consent.

Potential risks and burdens

The University of Manchester as research governance sponsor, will arrange insurance which provides cover for legal liabilities arising from the management and design of the research and the actions or those of its staff and supervised students. The NHS indemnity scheme will apply to the study subject to approval being in place from the NHS Trust. The investigators will report immediately any research incidents according to the sponsor's SOP.

Cannulations

A venous cannulation will be performed. A cannula will be inserted into an antecubital fossa vein for the intravenous administration of the radiotracer. In order to obtain arterial input functions for quantification of the PET images, a cannula will be inserted into the radial artery under local anaesthetic and after a successful modified Allen's test to evaluate ulnar artery patency. Arterial cannulation is a safe procedure, when performed by qualified and trained staff, who limits any potential risk, such as nerve damage and intravascular thrombosis, which furthermore is also counterbalanced by the presence of a dual circulation in most of the population. Cannulations can be slightly painful but local anaesthetic will be used for the arterial cannulation to minimize the pain. Subjects may experience slight bruising after both these procedures.

PET scans

Any exposure to radiation carries a very small risk of potential tissue damage that could lead to cancer at a later date. However, a standard PET scan involves a very small amount of radiation – about the same as the amount a person gets from natural sources, such as the sun, over three years. At a population level, this radiation dose is associated with a very small additional risk of inducing cancer in later life; however, this risk is negligible in patients who have a significantly shortened life expectancy due to the diagnosis of high grade glioma. According to the International Commission for Radiological Protection (ICRP), Report 62 on "Radiation Protection in Biomedical Research", radiation exposure in this study is classified as category IIb (moderate risk) and can be justified by the substantial societal benefit gained from validating noninvasive biomarkers of hypoxia in high-grade glial tumours. As a small precaution, the patients will be advised to keep away children and pregnant women for seven hours after the PET scans. Effective dose for [^{18}F]FAZA is 6.83 mSv. Effective dose for [^{18}F]FMISO is 7.21 mSv. The effective dose for [^{15}O]H_2O is considerably lower (0.89 mSv).

MRI scans

The main issue for the MRI is patient comfort during the scanning procedure. The breathing circuit has been designed to be as comfortable as possible and has been well tolerated in previous experiments performed within this research group on healthy volunteers and patients. However, MRI scanning can be claustrophobic and noisy. Earplugs and music in the background will be provided to make the patient feel more relaxed. We will be administering both medical air and 100% oxygen

through the breathing circuit. Although prolonged breathing of 100% oxygen may potentially result in clinical manifestations of oxygen toxicity, involving prevalently the central nervous system and the lungs, there is no known risk of breathing 100% oxygen for short (<15 minute) periods. Gadolinium contrast agent will also be administered to all subjects during the DCE-MRI acquisition. The potential risk of contrast administration for subjects with healthy kidney function is very small and the most common side–effect of slight nausea is very rare. The hazards of allergy-like reactions to gadolinium have been reported but are extremely rare. The subjects will require a cannula, which can cause bruising and discomfort. However, in all cases full medical cover will be present and capable of using the available medical and resuscitation equipment. Subjects with impaired renal function may be at risk of developing nephrogenic systemic fibrosis (NSF) following administration of gadolinium contrast agent, so subjects should have normal urea and electrolytes test results. If at any point the participant appears distressed, or presses the contact alarm, the scan will be interrupted and if appropriate will be terminated. Occasionally the surgical team may need some extra scan data and images to help plan your surgery. For the patient's convenience, the data could be collected while the patient is being scanned for this study. This will not happen for all patients but we will ask permission from the patients to share the scan data with the surgical team. Any additional clinical MR images acquired by the University will be transferred, with the patient permission, to SRFT for clinical purposes. This transfer will be the responsibility of the University. Clinical reporting and any other related use of these images will be under the responsibility of the Trust.

Surgery

The principal risks of biopsies are bleeding and neurological deficit. However since these biopsies will be taken into regions planned to be resected in the same operation, the hazard is minimal. The additional biopsy of the oedeamatous region will increase the duration of the surgical procedure up to approximately 30 min, which does not have a significant impact upon anesthetic risk.

Tissue storage

Tumour tissue and blood samples will be collected and stored at The University of Manchester in a dedicated freezer, suitable for storage of human samples. At the end of the study the samples will be donated to the MCRC Biobank at the CRUK Manchester Institute. The MRCR Biobank is under custodial arrangements and key-coded/locked access. The laboratory has extensive experience in storing biological samples and integrated systems for documentation and tracking. A suite of standard Patient Information Sheets and Patient Consent Forms have been developed and approved. Informed patient consent will always be obtained in this study before patient samples are taken and utilized.

Patient confidentiality

Once a patient has consented to the study, a patient identification number will be allocated for

MR and PET imaging and brain samples will also be given a lab identifier number. All information collected will be strictly confidential and compliant with the Data Protection Act 1988, Human Tissue Act 2004 and European Law. Only the PI, coinvestigators and authorized personnel will have access to break study codes and identify the donors of the samples. Any unused samples retained indefinitely for use in future research with collaborators will only be available in an anonymous format. No personal details will be divulged. Clinical and imaging data generated will become anonymous by removing all identifiable personal data prior to analysis. Example images will be published without identifiable personal data. Study data and material may be looked at by individuals from the University of Manchester, from regulatory authorities or from the NHS Trust, for monitoring and auditing purposes and this may include access to personal information.

Data handling, storage and processing

The investigator will document in the patient files (hospital files) at least the date of patient's written informed consent, medical history and physical examination, adverse events, concomitant medication and diseases. Consent forms will be retained as essential documents, but items such as contact details will be deleted as soon as they are no longer needed. Researchers and collaborators directly involved in the project will have access to participants' personal data during the study for the purpose of the study. Patient consent will be sought in the study consent form.

Any imaging data related to the study will be archived at the study site or in an online archive, accessible only from computer terminals within The University of Manchester. Any other document related to the study will also be archived at the study sites or in a central archive, in restricted access locked office, if hard copy, or on a user restricted secure file server where electronic. This includes the careful listing of the identity of the patients involved in the study. This list and the signed informed consent forms are key documents that will be stored by the investigators.

All stored research data generated by the study (including some personal data required for retention among the radiopharmaceutical manufacturing and tracer administration records) will be retained for up to 15 years after the end of the study, in accordance with The University of Manchester and the SRFT SOPs on the retention of the research data. At the end of the 15 year period, the chief investigator (CI, Prof Alan Jackson), The University of Manchester and the SRFT R&D manager will be asked for authorization to destroy the documents. Documents will be destroyed through the appropriate systems for the destruction of confidential information. A record of the documents destroyed will be kept.

Processing of imaging data will be performed after anonymization of patient identification data. Following publication of the main findings, anonymized data will be made available through the CRUK imaging data repository which is currently in development. Data access through the repository will be subject to constraints imposed by the scope of the ethics process.

Publication policy

The investigators intend to publish the results of the study via oral/poster presentation at

national or international congresses and via scientific papers to be published in peer-reviewed journals to disseminate the findings.

Benefits of the study

There is no direct benefit to study participants. Findings of this study are likely to benefit patients with high-grade glial cell tumours in the future. Study participants will be offered refreshments after the scans and reimbursement of travel expenses.

Resources and costs

There is secured funding for this study through the Engineering and Physical Sciences Research Council (EPSRC) and CRUK Cancer Imaging Centres grant (reference: C8742/A18097). This will cover the salary of the clinical research fellow and all research costs associated with the acquisition of the data and research costs relating to this application.

References

1. Wen PY, Kesari S, Malignant Gliomas in Adults. N Engl J Med., 2008. 359(5): p. 492-507.
2. Woehrer A, Bauchet L, Barnholtz-Sloan JS, Glioblastoma survival: has it improved? Evidence from population-based studies. Curr Opin Neurol, 2014. 27(6): p. 666-74.
3. Wolbers JG, Novel strategies in glioblastoma surgery aim at safe, supra-maximum resection in conjunction with local therapies. Chin J Cancer, 2014. 33(1): p. 8-15.
4. Yang L, et al., Hypoxia and hypoxia-inducible factors in glioblastoma multiforme progression and therapeutic implications. Exp Cell Res, 2012. 318(19): p. 2417-26.
5. Vartanian A, et al., GBM's multifaceted landscape: highlighting regional and microenvironmental heterogeneity. Neuro Oncol, 2014. 16(9): p. 1167-75.
6. Yoon JH, et al., Proteomic analysis of hypoxia-induced U373MG glioma secretome reveals novel hypoxia-dependent migration factors. Proteomics, 2014. 14(12): p. 1494-502.
7. Hammond EM, et al., The meaning, measurement and modification of hypoxia in the laboratory and the clinic. Clin Oncol (R Coll Radiol), 2014. 26(5): p. 277-88.
8. Postema EJ, et al., Initial results of hypoxia imaging using 1-alpha-D: -(5-deoxy-5-[18F]-fluoroarabinofuranosyl)-2-nitroimidazole (18F-FAZA). Eur J Nucl Med Mol Imaging, 2009. 36(10): p. 1565-73.
9. Wiebe LI, PET radiopharmaceuticals for metabolic imaging in oncology. International Congress Series, 2004. 1264: p. 53-76.
10. Noij DP, et al., Contrast-enhanced perfusion magnetic resonance imaging for head and neck squamous cell carcinoma: a systematic review. Oral Oncol, 2015. 51(2): p. 124-38.
11. Jansen JF, et al., Noninvasive assessment of tumor microenvironment using dynamic contrast-

enhanced magnetic resonance imaging and 18F-fluoromisonidazole positron emission tomography imaging in neck nodal metastases. Int J Radiat Oncol Biol Phys, 2010. 77(5): p. 1403-10.

12. Lopci E, et al., PET radiopharmaceuticals for imaging of tumor hypoxia:a review of the evidence. Am J Nucl Med Mol Imaging, 2014. 4(4): p. 365-384.

13. Ohno Y, Sugimura K, Hatabu H, Clinical oxygen-enhanced magnetic resonance imaging of the lung. Top Magn Reson Imaging., 2003. 14(3): p. 237-43.

14. Morgan AR, et al., Feasibility assessment of using oxygen-enhanced magnetic resonance imaging for evaluating the effect of pharmacological treatment in COPD. Eur J Radiol, 2014. 83(11): p. 2093-101.

15. O'Connor JP, et al., Preliminary study of oxygen-enhanced longitudinal relaxation in MRI: a potential novel biomarker of oxygenation changes in solid tumors. Int J Radiat Oncol Biol Phys, 2009. 75(4): p. 1209-15.

16. Linnik IV, et al., Noninvasive tumor hypoxia measurement using magnetic resonance imaging in murine U87 glioma xenografts and in patients with glioblastoma. Magn Reson Med, 2014. 71(5): p. 1854-62.

17. Ohno Y, Hatabu H, Basics concepts and clinical applications of oxygen-enhanced MR imaging. Eur J Radiol, 2007. 64(3): p. 320-8.

18. Allen E, Thromboangiitis obliterans: methods of diagnosis of chronic occlusive arterial lesions distal to the wrist with illustrative cases. Am J Med Sci, 1929. 178(2): p. 237-243.

References

1. Ostrom, Q.T., et al., *CBTRUS Statistical Report: Primary Brain and Central Nervous System Tumors Diagnosed in the United States in 2007-2011.* Neuro Oncol, 2014. **16**(Suppl 4): p. iv1-iv63.
2. Crocetti, E., et al., *Epidemiology of glial and non-glial brain tumours in Europe.* Eur J Cancer, 2012. **48**(10): p. 1532-42.
3. Louis, D.N., et al., *The 2016 World Health Organization Classification of Tumors of the Central Nervous System: a summary.* Acta Neuropathologica, 2016. **131**(6): p. 803-820.
4. Brodbelt, A., et al., *Glioblastoma in England: 2007-2011.* Eur J Cancer, 2015. **51**(4): p. 533-42.
5. Tran, B. and M.A. Rosenthal, *Survival comparison between glioblastoma multiforme and other incurable cancers.* J Clin Neurosci, 2010. **17**(4): p. 417-21.
6. Woehrer, A., L. Bauchet, and J.S. Barnholtz-Sloan, *Glioblastoma survival: has it improved? Evidence from population-based studies.* Curr Opin Neurol, 2014. **27**(6): p. 666-74.
7. Thakkar, J.P., et al., *Epidemiologic and Molecular Prognostic Review of Glioblastoma.* Cancer Epidemiol Biomarkers Prev, 2014. **23**(10): p. 1985-1996.
8. Ohgaki, H. and P. Kleihues, *The definition of primary and secondary glioblastoma.* Clin Cancer Res, 2013. **19**(4): p. 764-72.
9. Van Meir, E.G., et al., *Exciting new advances in neuro-oncology: the avenue to a cure for malignant glioma.* CA Cancer J Clin, 2010. **60**(3): p. 166-93.
10. Yan, H., et al., *IDH1 and IDH2 mutations in gliomas.* The New England journal of medicine, 2009. **360**(8): p. 765-773.
11. Appin, C.L., et al., *Glioblastoma with oligodendroglioma component (GBM-O): molecular genetic and clinical characteristics.* Brain pathology (Zurich, Switzerland), 2013. **23**(4): p. 454-461.
12. Hartmann, C., et al., *Patients with IDH1 wild type anaplastic astrocytomas exhibit worse prognosis than IDH1-mutated glioblastomas, and IDH1 mutation status accounts for the unfavorable prognostic effect of higher age: implications for classification of gliomas.* Acta Neuropathol, 2010. **120**(6): p. 707-18.
13. Ohgaki, H. and P. Kleihues, *Genetic pathways to primary and secondary glioblastoma.* The American journal of pathology, 2007. **170**(5): p. 1445-1453.
14. Yang, P., et al., *IDH mutation and MGMT promoter methylation in glioblastoma: results of a prospective registry.* Oncotarget, 2015. **6**(38): p. 40896-40906.
15. Louis DN, O.H., Wiestler OD, Cavenee WK, Burger PC, Jouvet A, Scheithauer BW, Kleihues P., *The 2007 WHO classification of tumours of the central nervous system.* Acta Neuropathol, 2007. **114**(2): p. 97-109.
16. Karsy, M., et al., *Established and emerging variants of glioblastoma multiforme: review of morphological and molecular features.* Folia Neuropathologica, 2012. **4**: p. 301-321.
17. Wesseling, P., J.M. Kros, and J.W.M. Jeuken, *The pathological diagnosis of diffuse gliomas: towards a smart synthesis of microscopic and molecular information in a multidisciplinary context.* Diagnostic Histopathology, 2011. **17**(11): p. 486-494.
18. Kanu, O.O., et al., *Glioblastoma multiforme: a review of therapeutic targets.* Expert Opinion on Therapeutic Targets, 2009. **13**(6): p. 701-18.
19. Brahimi-Horn, M.C., J. Chiche, and J. Pouysségur, *Hypoxia and cancer.* Journal of Molecular Medicine, 2007. **85**(12): p. 1301-1307.

20. Höckel, M. and P. Vaupel, *Tumor hypoxia: definitions and current clinical, biologic, and molecular aspects.* J Natl Cancer Inst, 2001. **93**(4): p. 266-76.
21. Tate, M.C. and M.K. Aghi, *Biology of Angiogenesis and Invasion in Glioma.* Neurotherapeutics, 2009. **6**(3): p. 447-57.
22. Vartanian, A., et al., *GBM's multifaceted landscape: highlighting regional and microenvironmental heterogeneity.* Neuro Oncol, 2014. **16**(9): p. 1167-75.
23. Raza, S.M., et al., *Necrosis and glioblastoma: a friend or a foe? A review and a hypothesis.* Neurosurgery, 2002. **51**(1): p. 2-12.
24. Homma, T., et al., *Correlation among pathology, genotype, and patient outcomes in glioblastoma.* J Neuropathol Exp Neurol, 2006. **65**(9): p. 846-54.
25. Phillips, H.S., et al., *Molecular subclasses of high-grade glioma predict prognosis, delineate a pattern of disease progression, and resemble stages in neurogenesis.* Cancer Cell, 2006. **9**(3): p. 157-73.
26. Verhaak, R.G., et al., *Integrated genomic analysis identifies clinically relevant subtypes of glioblastoma characterized by abnormalities in PDGFRA, IDH1, EGFR, and NF1.* Cancer Cell, 2010. **17**(1): p. 98-110.
27. Noushmehr, H., et al., *Identification of a CpG island methylator phenotype that defines a distinct subgroup of glioma.* Cancer Cell, 2010. **17**(5): p. 510-22.
28. Brennan, C.W., et al., *The somatic genomic landscape of glioblastoma.* Cell, 2013. **155**(2): p. 462-77.
29. Patel, A.P., et al., *Single-cell RNA-seq highlights intratumoral heterogeneity in primary glioblastoma.* Science, 2014. **344**(6190): p. 1396-1401.
30. Weller, M., et al., *EANO guideline for the diagnosis and treatment of anaplastic gliomas and glioblastoma.* The Lancet Oncology, 2014. **15**(9): p. e395-e403.
31. Taal, W., et al., *Single-agent bevacizumab or lomustine versus a combination of bevacizumab plus lomustine in patients with recurrent glioblastoma (BELOB trial): a randomised controlled phase 2 trial.* The Lancet Oncology, 2014. **15**(9): p. 943-953.
32. Walsh, J.C., et al., *The clinical importance of assessing tumor hypoxia: relationship of tumor hypoxia to prognosis and therapeutic opportunities.* Antioxid Redox Signal, 2014. **21**(10): p. 1516-54.
33. Mendichovszky, I. and A. Jackson, *Imaging hypoxia in gliomas.* Br J Radiol, 2011. **84 Spec No 2**: p. S145-58.
34. Vaupel, P. and L. Harrison, *Tumor hypoxia: causative factors, compensatory mechanisms, and cellular response.* Oncologist, 2004. **9**(Suppl 5): p. 4-9.
35. Bristow, R.G. and R.P. Hill, *Hypoxia and metabolism. Hypoxia, DNA repair and genetic instability.* Nat Rev Cancer, 2008. **8**(3): p. 180-92.
36. Pacheco-Torres, J., et al., *Imaging tumor hypoxia by magnetic resonance methods.* NMR Biomed, 2011. **24**(1): p. 1-16.
37. Yun, Z. and Q. Lin, *Hypoxia and regulation of cancer cell stemness.* Adv Exp Med Biol, 2014. **772**: p. 41-53.
38. Palazon, A., et al., *Molecular pathways: hypoxia response in immune cells fighting or promoting cancer.* Clin Cancer Res, 2012. **18**(5): p. 1207-13.
39. Brahimi-Horn, M.C., et al., *Hypoxia and Tumour Angiogenesis*, in *Tumor Angiogenesis*, D. Marmé and N. Fusenig, Editors. 2008, Springer Verlag: Berlin/Heidelberg. p. 171-194.
40. Evans, S.M., et al., *Hypoxia is important in the biology and aggression of human glial brain tumors.* Clin Cancer Res, 2004. **10**(24): p. 1078-0432 (Print).
41. Evans SM, J.K., Dunphy I, Jenkins WT, Nelson PT, Collins R, Wileyto EP, Jenkins K, Hahn SM, Stevens CW, Judkins AR, Phillips P, Geoerger B, Koch CJ, *Comparative measurements of hypoxia in human brain tumors using needle electrodes and EF5 binding.* Cancer Res, 2004. **64**(5): p. 1886-92.

42. Mayer, A., M. Hockel, and P. Vaupel, *Endogenous hypoxia markers: case not proven!* Adv Exp Med Biol., 2014. **614**: p. 127-36.
43. Ratcliffe, P.J., C.W. Pugh, and P.H. Maxwell, *Targeting tumors through the HIF system.* Nat Med, 2000. **6**(12): p. 1315-1316.
44. Liu, Y., et al., *The expression and significance of HIF-1alpha and GLUT-3 in glioma.* Brain Res, 2009. **1304**: p. 149-54.
45. Ke, Q. and M. Costa, *Hypoxia-inducible factor-1 (HIF-1).* Mol Pharmacol, 2006. **70**(5): p. 1469-80.
46. Zhang, P., et al., *Hypoxia-inducible factor 3 is an oxygen-dependent transcription activator and regulates a distinct transcriptional response to hypoxia.* Cell Rep, 2014. **6**(6): p. 1110-21.
47. Li, Q.F., et al., *Hypoxia upregulates hypoxia inducible factor (HIF)-3alpha expression in lung epithelial cells: characterization and comparison with HIF-1alpha.* Cell Res, 2006. **16**(6): p. 548-58.
48. Vaupel, P. and A. Mayer, *The clinical importance of assessing tumor hypoxia: Relationship of tumor hypoxia to prognosis and therapeutic opportunities.* Antioxid Redox Signal, 2014. **21**(10): p. 1516-54.
49. Lee, J.W., et al., *Hypoxia-inducible factor (HIF-1)alpha: its protein stability and biological functions.* Experimental & Molecular Medicine, 2004. **36**(1): p. 1-12.
50. Marie, S.K.N. and S.M.O. Shinjo, *Metabolism and Brain Cancer.* Clinics, 2011. **66**(Suppl 1): p. 33-43.
51. Gatenby, R.A. and R.J. Gillies, *Why do cancers have high aerobic glycolysis?* Nat Rev Cancer, 2004. **4**(11): p. 891-9.
52. Hammond, E.M., et al., *The meaning, measurement and modification of hypoxia in the laboratory and the clinic.* Clin Oncol (R Coll Radiol), 2014. **26**(5): p. 277-88.
53. Horsman, M.R., et al., *The oxygen effect and fractionated radiotherapy*. Basic clinical radiobiology. 2009, London: Arnold, H. 207-9.
54. Quintiliani, M., *The Oxygen Effect in Radiation Inactivation of DNA and Enzymes.* International Journal of Radiation Biology and Related Studies in Physics, Chemistry and Medicine, 1986. **50**(4): p. 573-594.
55. Brown, J.M. and W.R. Wilson, *Exploiting tumour hypoxia in cancer treatment.* Nat Rev Cancer, 2004. **4**(6): p. 437-47.
56. Harrison, L.B., *Impact of Tumor Hypoxia and Anemia on Radiation Therapy Outcomes.* The Oncologist, 2002. **7**(6): p. 492-508.
57. Urtasun, R.C., et al., *Clinical trials with hypoxic cell sensitizers: time to retrench or time to push forward?* Int J Radiat Oncol Biol Phys, 1984. **10**(9): p. 1691-6.
58. Overgaard, J., *Clinical evaluation of nitroimidazoles as modifiers of hypoxia in solid tumors.* Oncol Res, 1994. **6**(10-11): p. 509-18.
59. Overgaard, J., *Hypoxic modification of radiotherapy in squamous cell carcinoma of the head and neck--a systematic review and meta-analysis.* Radiother Oncol, 2011. **100**(1): p. 22-32.
60. Hendrickson, K., et al., *Hypoxia imaging with [F-18] FMISO-PET in head and neck cancer: Potential for guiding intensity modulated radiation therapy in overcoming hypoxia-induced treatment resistance.* Radiotherapy and Oncology, 2011. **101**(3): p. 369-375.
61. Toma-Dasu, I., et al., *Dose prescription and treatment planning based on FMISO-PET hypoxia.* Acta Oncol., 2012. **21**(2): p. 222-30.
62. Linnik, I.V., et al., *Noninvasive tumor hypoxia measurement using magnetic resonance imaging in murine U87 glioma xenografts and in patients with glioblastoma.* Magn Reson Med, 2014. **71**(5): p. 1854-62.
63. Carreau, A., et al., *Why is the partial oxygen pressure of human tissues a crucial parameter? Small molecules and hypoxia.* J Cell Mol Med, 2011. **15**(6): p. 1239-53.

64. Bell, C., et al., *Hypoxia Imaging in Gliomas With F-Fluoromisonidazole PET: Toward Clinical Translation.* Semin Nucl Med, 2015. **45**(2): p. 136-150.
65. Postema, E.J., et al., *Initial results of hypoxia imaging using 1-alpha-D: -(5-deoxy-5-[18F]-fluoroarabinofuranosyl)-2-nitroimidazole (18F-FAZA).* Eur J Nucl Med Mol Imaging, 2009. **36**(10): p. 1565-73.
66. Price, J.M., S.P. Robinson, and D.M. Koh, *Imaging hypoxia in tumours with advanced MRI.* Q J Nucl Med Mol Imaging, 2013. **57**(3): p. 257-70.
67. Jansen, J.F., et al., *Noninvasive assessment of tumor microenvironment using dynamic contrast-enhanced magnetic resonance imaging and 18F-fluoromisonidazole positron emission tomography imaging in neck nodal metastases.* Int J Radiat Oncol Biol Phys, 2010. **77**(5): p. 1403-10.
68. Koh, D.M. and D.J. Collins, *Diffusion-weighted MRI in the body: applications and challenges in oncology.* AJR Am J Roentgenol, 2007. **188**(6): p. 1622-35.
69. Hompland, T., et al., *DW-MRI in assessment of the hypoxic fraction, interstitial fluid pressure, and metastatic propensity of melanoma xenografts.* BMC Cancer, 2014. **14**: p. 92.
70. Hino-Shishikura, A., et al., *Tumor hypoxia and microscopic diffusion capacity in brain tumors: a comparison of (62)Cu-Diacetyl-Bis (N4-Methylthiosemicarbazone) PET/CT and diffusion-weighted MR imaging.* Eur J Nucl Med Mol Imaging, 2014. **41**(7): p. 1419-27.
71. Lopci E, G.I., Chiti A, Nanni C, Cicoria G, Toschi L, Fonti C, Lodi F, Mattioli S, Fanti S., *PET radiopharmaceuticals for imaging of tumor hypoxia:a review of the evidence.* American Journal of Nuclear Medicine and Molecular Imaging, 2014. **4**(4): p. 365-384.
72. Robinson, S.P., et al., *Tumor vascular architecture and function evaluated by non-invasive susceptibility MRI methods and immunohistochemistry.* J Magn Reson Imaging, 2003. **17**(4): p. 445-54.
73. Ohno, Y., H. Sugimura K Fau - Hatabu, and H. Hatabu, *Clinical oxygen-enhanced magnetic resonance imaging of the lung.* Top Magn Reson Imaging., 2003. **14**(3): p. 237-43.
74. O'Connor, J.P., et al., *Preliminary study of oxygen-enhanced longitudinal relaxation in MRI: a potential novel biomarker of oxygenation changes in solid tumors.* Int J Radiat Oncol Biol Phys, 2009. **75**(4): p. 1209-15.
75. Young Ir Fau - Clarke, G.J., et al., *Enhancement of relaxation rate with paramagnetic contrast agents in NMR imaging.* J Comput Tomogr., 1983. **5**(6): p. 543-7.
76. Chitneni, S.K., et al., *Molecular imaging of hypoxia.* Journal of nuclear medicine, 2011. **52**(2): p. 165-8.
77. Vallabhajosula, S., *(18)F-labeled positron emission tomographic radiopharmaceuticals in oncology: an overview of radiochemistry and mechanisms of tumor localization.* Semin Nucl Med, 2007. **37**(6): p. 400-19.
78. Groves, A.M., et al., *Non-[18F]FDG PET in clinical oncology.* The Lancet Oncology, 2007. **8**(9): p. 822-830.
79. Shetty, D., J.M. Jeong, and H. Shim, *Stroma targeting nuclear imaging and radiopharmaceuticals.* Int J Mol Imaging, 2012. **2012**: p. 817682.
80. Kawai, N., et al., *Correlation between (1)(8)F-fluoromisonidazole PET and expression of HIF-1alpha and VEGF in newly diagnosed and recurrent malignant gliomas.* Eur J Nucl Med Mol Imaging, 2014. **41**(10): p. 1870-8.
81. Grönroos, T.J., et al., *Hypoxia, blood flow and metabolism in squamous-cell carcinoma of the head and neck: correlations between multiple immunohistochemical parameters and PET.* BMC cancer, 2014. **14**(1): p. 876.

82. Kawai, N., et al., *Correlation of biological aggressiveness assessed by 11C-methionine PET and hypoxic burden assessed by 18F-fluoromisonidazole PET in newly diagnosed glioblastoma.* Eur J Nucl Med Mol Imaging, 2011. **38**(3): p. 441-50.
83. Rajendran, J.G., et al., *Tumor hypoxia imaging with [F-18] fluoromisonidazole positron emission tomography in head and neck cancer.* Clin Cancer Res, 2006. **12**(18): p. 5435-41.
84. Thorwarth, D., et al., *A kinetic model for dynamic [18F]-Fmiso PET data to analyse tumour hypoxia.* Phys Med Biol, 2005. **50**(10): p. 2209-24.
85. Sorger, D., et al., *[18F]Fluoroazomycinarabinofuranoside (18FAZA) and [18F]Fluoromisonidazole (18FMISO): a comparative study of their selective uptake in hypoxic cells and PET imaging in experimental rat tumors.* Nuclear Medicine and Biology, 2003. **30**(3): p. 317-326.
86. Piert, M., et al., *Hypoxia-Specific Tumor Imaging with 18 F-Fluoroazomycin Arabinoside.* J Nucl Med, 2005. **46**: p. 106-113.
87. Busk, M., et al., *Cellular uptake of PET tracers of glucose metabolism and hypoxia and their linkage.* Eur J Nucl Med Mol Imaging, 2008. **35**(12): p. 2294-303.
88. Peeters, S.G., et al., *A Comparative Study of the Hypoxia PET Tracers [(18)F]HX4, [(18)F]FAZA, and [(18)F]FMISO in a Preclinical Tumor Model.* Int J Radiat Oncol Biol Phys, 2015. **91**(2): p. 351-9.
89. Busk, M., et al., *Can hypoxia-PET map hypoxic cell density heterogeneity accurately in an animal tumor model at a clinically obtainable image contrast?* Radiother Oncol, 2009. **92**(3): p. 429-36.
90. Lee, N.Y., et al., *Fluorine-18-labeled fluoromisonidazole positron emission and computed tomography-guided intensity-modulated radiotherapy for head and neck cancer: a feasibility study.* Int J Radiat Oncol Biol Phys, 2008. **70**(1): p. 2-13.
91. Rockne, R.C., et al., *A patient-specific computational model of hypoxia-modulated radiation resistance in glioblastoma using 18F-FMISO-PET.* Journal of The Royal Society Interface, 2014. **12**(103).
92. Beck, R., et al., *Pretreatment 18F-FAZA PET predicts success of hypoxia-directed radiochemotherapy using tirapazamine.* J Nucl Med, 2007. **48**(6): p. 973-80.
93. Wu, Y., et al., *Oxygen-enhanced magnetic resonance imaging of the brain: a rodent model.* Neuroreport, 2012. **23**(10): p. 581-4.
94. Jensen, R.L., et al., *Preoperative dynamic contrast-enhanced MRI correlates with molecular markers of hypoxia and vascularity in specific areas of intratumoral microenvironment and is predictive of patient outcome.* Neuro Oncol, 2014. **16**(2): p. 280-91.
95. Barajas RF Jr, H.J., Chang JS, Vandenberg SR, Yeh RF, Parsa AT, McDermott MW, Berger MS, Dillon WP, Cha S, *Glioblastoma multiforme regional genetic and cellular expression patterns: influence on anatomic and physiologic MR imaging.* Radiology, 2010. **254**(2): p. 564-76.
96. Jain, R., et al., *In vivo correlation of tumor blood volume and permeability with histologic and molecular angiogenic markers in gliomas.* AJNR Am J Neuroradiol, 2011. **32**(2): p. 388-94.
97. Barajas, R.F., Jr., et al., *Regional variation in histopathologic features of tumor specimens from treatment-naive glioblastoma correlates with anatomic and physiologic MR Imaging.* Neuro Oncol, 2012. **14**(7): p. 942-54.
98. Awasthi, R., et al., *Discriminant analysis to classify glioma grading using dynamic contrast-enhanced MRI and immunohistochemical markers.* Neuroradiology, 2012. **54**(3): p. 205-13.
99. Li, X., et al., *Relationship of MR-derived lactate, mobile lipids, and relative blood volume for gliomas in vivo.* AJNR Am J Neuroradiol., 2005. **26**(4): p. 760-9.

100. Jensen, R.L., *Brain tumor hypoxia: tumorigenesis, angiogenesis, imaging, pseudoprogression, and as a therapeutic target.* J Neurooncol, 2009. **92**(3): p. 317-35.
101. Swanson, K.R., et al., *Complementary but distinct roles for MRI and 18F-fluoromisonidazole PET in the assessment of human glioblastomas.* J Nucl Med, 2009. **50**(1): p. 36-44.
102. Spence, A.M., et al., *Regional hypoxia in glioblastoma multiforme quantified with [18F]fluoromisonidazole positron emission tomography before radiotherapy: correlation with time to progression and survival.* Clin Cancer Res, 2008. **14**(9): p. 2623-30.
103. Belloli, S., et al., *Characterization of biological features of a rat F98 GBM model: a PET-MRI study with [18F]FAZA and [18F]FDG.* Nucl Med Biol, 2013. **40**(6): p. 831-40.
104. Tran, L.B., et al., *Predictive value of F-FAZA PET imaging for guiding the association of radiotherapy with nimorazole: A preclinical study.* Radiotherapy & Oncology, 2015. **114**(2): p. 189-94.
105. Tran, L.B., et al., *Potential role of hypoxia imaging using (18)F-FAZA PET to guide hypoxia-driven interventions (carbogen breathing or dose escalation) in radiation therapy.* Radiotherapy & Oncology, 2014. **113**(2): p. 204-9.
106. Dence, C.S., et al., *Autoradiographic and small-animal PET comparisons between (18)F-FMISO, (18)F-FDG, (18)F-FLT and the hypoxic selective (64)Cu-ATSM in a rodent model of cancer.* Nucl Med Biol, 2008. **35**(6): p. 713-20.
107. Valable, S., et al., *Complementary information from magnetic resonance imaging and (18)F-fluoromisonidazole positron emission tomography in the assessment of the response to an antiangiogenic treatment in a rat brain tumor model.* Nucl Med Biol, 2011. **38**(6): p. 781-93.
108. Corroyer-Dulmont, A., et al., *Noninvasive assessment of hypoxia with 3-[18F]-fluoro-1-(2-nitro-1-imidazolyl)-2-propanol ([18F]-FMISO): a PET study in two experimental models of human glioma.* Biol Chem, 2013. **394**(4): p. 529-39.
109. Lo Dico, A., et al., *Validation of an engineered cell model for in vitro and in vivo HIF-1alpha evaluation by different imaging modalities.* Mol Imaging Biol, 2014. **16**(2): p. 210-23.
110. Carlier, T. and C. Bailly, *State-Of-The-Art and Recent Advances in Quantification for Therapeutic Follow-Up in Oncology Using PET.* Front Med (Lausanne), 2015. **2**: p. 18.
111. Kelada, O.J. and D.J. Carlson, *Molecular imaging of tumor hypoxia with positron emission tomography.* Radiation Research, 2014. **181**(4): p. 335-49.
112. Verwer, E.E., et al., *Pharmacokinetic analysis of [18F]FAZA in non-small cell lung cancer patients.* Eur J Nucl Med Mol Imaging, 2013. **40**(10): p. 1523-31.
113. Bruehlmeier M, R.U., Schubiger PA, Ametamey SM., *Assessment of hypoxia and perfusion in human brain tumors using PET with 18F-fluoromisonidazole and 15O-H2O.* J Nucl Med, 2004. **45**(11): p. 1851-9.
114. Gross, M.W., et al., *Calibration of misonidazole labeling by simultaneous measurement of oxygen tension and labeling density in multicellular spheroids.* Int J Cancer, 1995. **16**(6): p. 567-73.
115. Gruner, J.M., et al., *Brain perfusion CT compared with (1)(5)O-H(2)O PET in patients with primary brain tumours.* Eur J Nucl Med Mol Imaging, 2012. **39**(11): p. 1691-701.
116. Jovcevska, I., N. Kocevar, and R. Komel, *Glioma and glioblastoma - how much do we (not) know?* Mol Clin Oncol, 2013. **1**(6): p. 935-941.
117. Thompson, G., et al., *Imaging biomarkers of angiogenesis and the microvascular environment in cerebral tumours.* Br J Radiol, 2011. **84 Spec No 2**: p. S127-44.
118. Shi, K., et al., *Quantitative assessment of hypoxia kinetic models by a cross-study of dynamic 18F-FAZA and 15O-H2O in patients with head and neck tumors.* J Nucl Med, 2010. **51**(9): p. 1386-94.

119. Rijken, P.F.J.W., et al., *Spatial relationship between hypoxia and the (perfused) vascular network in a human glioma xenograft: a quantitative multi-parameter analysis1.* International Journal of Radiation Oncology*Biology*Physics, 2000. **48**(2): p. 571-582.
120. Groshar, D., et al., *Imaging tumor hypoxia and tumor perfusion.* J Nucl Med, 1993. **34**(6): p. 885-8.
121. Keunen, O., et al., *Multimodal imaging of gliomas in the context of evolving cellular and molecular therapies.* Adv Drug Deliv Rev, 2014. **76**: p. 98-115.
122. O'Connor, J.P.B., et al., *Oxygen enhanced MRI accurately identifies, quantifies, and maps hypoxia in preclinical cancer models.* Cancer Research, 2015.
123. Mehemed, T.M., et al., *Dynamic oxygen-enhanced MRI of cerebrospinal fluid.* PLoS One, 2014. **9**(6): p. e100723.
124. Leenders, K.L., et al., *Cerebral blood flow, blood volume and oxygen utilization normal values and effect of age.* Brain, 1990. **113**(1): p. 27-47.
125. Cain, J.R., et al., *Impact of gas delivery systems on imaging studies of human cerebral blood flow.* Radiol Res Pract, 2013. **2013**: p. 694803.
126. Smith, S.M., et al., *Accurate, robust, and automated longitudinal and cross-sectional brain change analysis.* Neuroimage, 2002. **17**(1): p. 479-89.
127. Fagiolo, G., A. Waldman, and J.V. Hajnal, *A simple procedure to improve FMRIb Software Library Brain Extraction Tool performance.* Br J Radiol, 2008. **81**(963): p. 250-1.
128. Popescu, V., et al., *Optimizing parameter choice for FSL-Brain Extraction Tool (BET) on 3D T1 images in multiple sclerosis.* Neuroimage, 2012. **61**(4): p. 1484-94.
129. Smith, S.M., et al., *Advances in functional and structural MR image analysis and implementation as FSL.* Neuroimage, 2004. **23 Suppl 1**: p. S208-19.
130. Heiberg, E., et al., *Design and validation of Segment--freely available software for cardiovascular image analysis.* BMC Med Imaging, 2010. **10**: p. 1.
131. Koskinen, S.M., et al., *The normal internal carotid artery: a computed tomography angiographic study.* Neuroradiology, 2014. **56**(9): p. 723-729.
132. GraphPad. *"Comparing slopes and intercepts"* [cited 2018 17 July]; Available from: https://www.graphpad.com/guides/prism/7/curve-fitting/index.htm?Reg_Comparingslopesandintercepts.htm.
133. Janusonis, S., *Comparing two small samples with an unstable, treatment-independent baseline.* J Neurosci Methods, 2009. **179**(2): p. 173-8.
134. Lumley, T., et al., *The importance of the normality assumption in large public health data sets.* Annu Rev Public Health, 2002. **23**: p. 151-69.
135. Cox, N.R., *Estimation of the Correlation between a Continuous and a Discrete Variable.* Biometrics, 1974. **30**(1): p. 171-178.
136. Zhou, H., et al., *Incorporating Oxygen-Enhanced MRI into Multi-Parametric Assessment of Human Prostate Cancer.* Diagnostics (Basel), 2017. **7**(3).
137. Little, R.A., et al., *Mapping Hypoxia in Renal Carcinoma with Oxygen-enhanced MRI: Comparison with Intrinsic Susceptibility MRI and Pathology.* Radiology, 2018: p. 171531.
138. Behrens, P.F., C.B. Ostertag, and P.C. Warnke, *Regional cerebral blood flow in peritumoral brain edema during dexamethasone treatment: a xenon-enhanced computed tomographic study.* Neurosurgery, 1998. **43**(2): p. 235-40; discussion 240-1.
139. Watson, N.A., et al., *The effect of hyperoxia on cerebral blood flow: a study in healthy volunteers using magnetic resonance phase-contrast angiography.* Eur J Anaesthesiol, 2000. **17**(3): p. 152-9.

140. Kety, S.S. and C.F. Schmidt, *The effects of altered arterial tensions of carbon dioxide and oxygen on cerebral blood flow and cerebral oxygen consumption of normal young men.* Journal of Clinical Investigation, 1948. **27**(4): p. 484-492.
141. Nakajima, S., et al., *Cerebral vasomotor responsiveness during 100% oxygen inhalation in cerebral ischemia.* Arch Neurol, 1983. **40**(5): p. 271-6.
142. Rostrup, E., et al., *Signal changes in gradient echo images of human brain induced by hypo- and hyperoxia.* NMR Biomed, 1995. **8**(1): p. 41-7.
143. Johnston, A.J., et al., *Cerebral oxygen vasoreactivity and cerebral tissue oxygen reactivity.* Br J Anaesth, 2003. **90**(6): p. 774-86.
144. Xu, F., et al., *Effect of hypoxia and hyperoxia on cerebral blood flow, blood oxygenation, and oxidative metabolism.* J Cereb Blood Flow Metab, 2012. **32**(10): p. 1909-18.
145. Duong, T.Q., C. Iadecola, and S.G. Kim, *Effect of hyperoxia, hypercapnia, and hypoxia on cerebral interstitial oxygen tension and cerebral blood flow.* Magn Reson Med, 2001. **45**(1): p. 61-70.
146. Leahy, F.A., et al., *Effect of CO2 and 100% O2 on cerebral blood flow in preterm infants.* J Appl Physiol Respir Environ Exerc Physiol, 1980. **48**(3): p. 468-72.
147. Zaharchuk, G., et al., *Noninvasive oxygen partial pressure measurement of human body fluids in vivo using magnetic resonance imaging.* Acad Radiol, 2006. **13**(8): p. 1016-24.
148. Braga, F.T., et al., *Relationship between the Concentration of Supplemental Oxygen and Signal Intensity of CSF Depicted by Fluid-Attenuated Inversion Recovery Imaging.* American Journal of Neuroradiology, 2003. **24**(9): p. 1863.
149. Bhogal, A.A., et al., *Quantitative T1 mapping under precisely controlled graded hyperoxia at 7T.* J Cereb Blood Flow Metab, 2017. **37**(4): p. 1461-1469.
150. Jeong, H.K., et al., *Reduction of Oxygen-Induced CSF Hyperintensity on FLAIR MR Images in Sedated Children: Usefulness of Magnetization-Prepared FLAIR Imaging.* AJNR Am J Neuroradiol, 2016. **37**(8): p. 1549-55.
151. Brown, M.M., J.P.H. Wade, and J. Marshall, *Fundamental importance of arterial oxygen content in the regulation of cerebral blood flow in man.* Brain, 1985. **108**(1): p. 81-93.
152. Lambertsen, C.J., et al., *Oxygen toxicity; effects in man of oxygen inhalation at 1 and 3.5 atmospheres upon blood gas transport, cerebral circulation and cerebral metabolism.* J Appl Physiol, 1953. **5**(9): p. 471-86.
153. Kennedy, C., G.D. Grave, and J.W. Jehle, *Effect of Hyperoxia on the Cerebral Ciculation of the Newborn Puppy.* Pediatric Research, 1971. **5**: p. 659.
154. Kazemi, H., et al., *Dynamics of oxygen transfer in the cerebrospinal fluid.* Respiration Physiology, 1968. **4**(1): p. 24-31.
155. Losert, C., et al., *Oxygen-enhanced MRI of the brain.* Magn Reson Med, 2002. **48**(2): p. 271-7.
156. Haddock, B., et al., *Measurement of brain oxygenation changes using dynamic T1-weighted imaging.* NeuroImage, 2013. **78**: p. 7-15.
157. Ogoh, S., et al., *The effect of oxygen on dynamic cerebral autoregulation: critical role of hypocapnia.* J Appl Physiol (1985), 2010. **108**(3): p. 538-43.
158. O'Connor, J.P., et al., *Comparison of normal tissue R1 and R*2 modulation by oxygen and carbogen.* Magn Reson Med, 2009. **61**(1): p. 75-83.
159. Featherstone, A.K., et al., *Data-driven mapping of hypoxia-related tumor heterogeneity using DCE-MRI and OE-MRI.* Magn Reson Med, 2018. **79**(4): p. 2236-2245.
160. Fan, Q., et al., *Investigation of hypoxia conditions using oxygen-enhanced magnetic resonance imaging measurements in glioma models.* Oncotarget, 2017. **8**(19): p. 31864-31875.

161. Welch, B.L., *The Generalization of `Student's' Problem when Several Different Population Variances are Involved.* Biometrika, 1947. **34**(1/2): p. 28-35.
162. Anzai, Y., et al., *Paramagnetic Effect of Supplemental Oxygen on CSF Hyperintensity on Fluid-Attenuated Inversion Recovery MR Images.* American Journal of Neuroradiology, 2004. **25**(2): p. 274.
163. Egeland, T.A., et al., *Magnetic resonance imaging of tumor necrosis.* Acta Oncol, 2011. **50**(3): p. 427-34.
164. Gaustad, J.-V., et al., *Dynamic contrast-enhanced magnetic resonance imaging of human melanoma xenografts with necrotic regions.* Journal of Magnetic Resonance Imaging, 2007. **26**(1): p. 133-143.
165. Pistollato, F., et al., *Intratumoral hypoxic gradient drives stem cells distribution and MGMT expression in glioblastoma.* Stem Cells, 2010. **28**(5): p. 851-62.
166. Bremer, C., et al., *High-dose Gd-DTPA vs. Bis-Gd-mesoporphyrin for monitoring laser-induced tissue necrosis.* Journal of Magnetic Resonance Imaging, 2005. **21**(6): p. 801-808.
167. Koh, T.S., et al., *In vivo measurement of gadolinium diffusivity by dynamic contrast-enhanced MRI: A preclinical study of human xenografts.* Magnetic Resonance in Medicine, 2013. **69**(1): p. 269-276.
168. Pellerin, M., T.E. Yankeelov, and M. Lepage, *Incorporating contrast agent diffusion into the analysis of DCE-MRI data.* Magnetic Resonance in Medicine, 2007. **58**(6): p. 1124-1134.
169. Molina, D., et al., *Tumour heterogeneity in glioblastoma assessed by MRI texture analysis: a potential marker of survival.* Br J Radiol, 2016: p. 20160242.
170. Lee, J., et al., *Texture Feature Ratios from Relative CBV Maps of Perfusion MRI Are Associated with Patient Survival in Glioblastoma.* AJNR Am J Neuroradiol, 2016. **37**(1): p. 37-43.
171. Oh, J., et al., *Survival analysis in patients with glioblastoma multiforme: predictive value of choline-to-N-acetylaspartate index, apparent diffusion coefficient, and relative cerebral blood volume.* J Magn Reson Imaging, 2004. **19**(5): p. 546-54.
172. Murakami, R., et al., *Malignant supratentorial astrocytoma treated with postoperative radiation therapy: prognostic value of pretreatment quantitative diffusion-weighted MR imaging.* Radiology, 2007. **243**(2): p. 493-9.
173. Higano, S., et al., *Malignant astrocytic tumors: clinical importance of apparent diffusion coefficient in prediction of grade and prognosis.* Radiology, 2006. **241**(3): p. 839-46.
174. Burth, S., et al., *Clinical parameters outweigh diffusion- and perfusion-derived MRI parameters in predicting survival in newly diagnosed glioblastoma.* Neuro Oncol, 2016. **18**(12): p. 1673-1679.
175. Law, M., et al., *Gliomas: predicting time to progression or survival with cerebral blood volume measurements at dynamic susceptibility-weighted contrast-enhanced perfusion MR imaging.* Radiology, 2008. **247**(2): p. 490-8.
176. Leu, K., et al., *Bidirectional Contrast agent leakage correction of dynamic susceptibility contrast (DSC)-MRI improves cerebral blood volume estimation and survival prediction in recurrent glioblastoma treated with bevacizumab.* J Magn Reson Imaging, 2016. **44**(5): p. 1229-1237.
177. Jabehdar Maralani, P., et al., *Association of dynamic susceptibility contrast enhanced MR Perfusion parameters with prognosis in elderly patients with glioblastomas.* Eur Radiol, 2015. **25**(9): p. 2738-44.
178. Nguyen, T.B., et al., *Preoperative prognostic value of dynamic contrast-enhanced MRI-derived contrast transfer coefficient and plasma volume in patients with cerebral gliomas.* AJNR Am J Neuroradiol, 2015. **36**(1): p. 63-9.

179. Ahn, S.S., et al., *Prediction of methylguanine methyltransferase promoter methylation in glioblastoma using dynamic contrast-enhanced magnetic resonance and diffusion tensor imaging.* J Neurosurg, 2014. **121**(2): p. 367-73.
180. Arevalo-Perez, J., et al., *T1-Weighted Dynamic Contrast-Enhanced MRI as a Noninvasive Biomarker of Epidermal Growth Factor Receptor vIII Status.* AJNR Am J Neuroradiol, 2015. **36**(12): p. 2256-61.
181. Paik, W., et al., *Pre-Operative Perfusion Skewness and Kurtosis Are Potential Predictors of Progression-Free Survival after Partial Resection of Newly Diagnosed Glioblastoma.* Korean J Radiol, 2016. **17**(1): p. 117-26.
182. Choi, Y.S., et al., *The Added Prognostic Value of Preoperative Dynamic Contrast-Enhanced MRI Histogram Analysis in Patients with Glioblastoma: Analysis of Overall and Progression-Free Survival.* AJNR Am J Neuroradiol, 2015. **36**(12): p. 2235-41.
183. Zhou, M., et al., *Identifying spatial imaging biomarkers of glioblastoma multiforme for survival group prediction.* J Magn Reson Imaging, 2017. **46**(1): p. 115-123.
184. Zhou, M., et al., *Radiologically defined ecological dynamics and clinical outcomes in glioblastoma multiforme: preliminary results.* Transl Oncol, 2014. **7**(1): p. 5-13.
185. Mills, S.J., et al., *Enhancing fraction in glioma and its relationship to the tumoral vascular microenvironment: A dynamic contrast-enhanced MR imaging study.* AJNR Am J Neuroradiol, 2010. **31**(4): p. 726-31.
186. Mills, S.J., et al., *Tumour enhancing fraction (EnF) in glioma: relationship to tumour grade.* Eur Radiol, 2009. **19**(6): p. 1489-98.
187. Tofts, P.S., *Modeling tracer kinetics in dynamic Gd-DTPA MR imaging.* J Magn Reson Imaging, 1997. **7**(1): p. 91-101.
188. Tofts, P.S., et al., *Estimating kinetic parameters from dynamic contrast-enhanced T(1)-weighted MRI of a diffusable tracer: standardized quantities and symbols.* J Magn Reson Imaging, 1999. **10**(3): p. 223-32.
189. Li, K.L. and A. Jackson, *New hybrid technique for accurate and reproducible quantitation of dynamic contrast-enhanced MRI data.* Magn Reson Med, 2003. **50**(6): p. 1286-95.
190. Haroon, H.A., et al., *A comparison of Ktrans measurements obtained with conventional and first pass pharmacokinetic models in human gliomas.* J Magn Reson Imaging, 2004. **19**(5): p. 527-36.
191. Li, K.L., et al., *Improved 3D quantitative mapping of blood volume and endothelial permeability in brain tumors.* J Magn Reson Imaging, 2000. **12**(2): p. 347-57.
192. Dolcetta-Capuzzo, A., et al., *Gastroenteric neuroendocrine neoplasms classification: comparison of prognostic models.* Cancer, 2013. **119**(1): p. 36-44.
193. Newson, R.B., *Comparing the predictive powers of survival models using Harrell's C or Somers' D.* Stata Journal, 2010. **10**(3): p. 339-358.
194. Li, K.L., et al., *Vascular biomarkers derived from dynamic contrast-enhanced MRI predict response of vestibular schwannoma to antiangiogenic therapy in type 2 neurofibromatosis.* Neuro Oncol, 2016. **18**(2): p. 275-82.
195. Mills, S.J., et al., *Candidate biomarkers of extravascular extracellular space: a direct comparison of apparent diffusion coefficient and dynamic contrast-enhanced MR imaging--derived measurement of the volume of the extravascular extracellular space in glioblastoma multiforme.* AJNR Am J Neuroradiol, 2010. **31**(3): p. 549-53.
196. Yankeelov, T.E., et al., *Integration of quantitative DCE-MRI and ADC mapping to monitor treatment response in human breast cancer: initial results.* Magn Reson Imaging, 2007. **25**(1): p. 1-13.
197. Ludemann, L., et al., *Quantitative measurement of leakage volume and permeability in gliomas, meningiomas and brain metastases with dynamic contrast-enhanced MRI.* Magn Reson Imaging, 2005. **23**(8): p. 833-41.

198. Zhu, X.P., et al., *Quantification of endothelial permeability, leakage space, and blood volume in brain tumors using combined T1 and T2* contrast-enhanced dynamic MR imaging.* J Magn Reson Imaging, 2000. **11**(6): p. 575-85.
199. Ludemann, L., et al., *Comparison of dynamic contrast-enhanced MRI with WHO tumor grading for gliomas.* Eur Radiol, 2001. **11**(7): p. 1231-41.
200. Armitage, P.A., et al., *Quantitative assessment of intracranial tumor response to dexamethasone using diffusion, perfusion and permeability magnetic resonance imaging.* Magn Reson Imaging, 2007. **25**(3): p. 303-10.
201. Andersen, C. and F.T. Jensen, *Differences in blood-tumour-barrier leakage of human intracranial tumours: quantitative monitoring of vasogenic oedema and its response to glucocorticoid treatment.* Acta Neurochir (Wien), 1998. **140**(9): p. 919-24.
202. Udomphorn, Y., W.M. Armstead, and M.S. Vavilala, *Cerebral Blood Flow and Autoregulation after Pediatric Traumatic Brain Injury.* Pediatric neurology, 2008. **38**(4): p. 225-234.
203. Paulson, O.B., S. Strandgaard, and L. Edvinsson, *Cerebral autoregulation.* Cerebrovasc Brain Metab Rev, 1990. **2**(2): p. 161-92.
204. Peterson, E.C., Z. Wang, and G. Britz, *Regulation of cerebral blood flow.* Int J Vasc Med, 2011. **2011**: p. 823525.
205. Sharma, D., et al., *Cerebral autoregulation and CO2 reactivity before and after elective supratentorial tumor resection.* J Neurosurg Anesthesiol, 2010. **22**(2): p. 132-7.
206. Steinback, C.D. and M.J. Poulin, *Influence of Hypoxia on Cerebral Blood Flow Regulation in Humans*, in *Hypoxia: Translation in Progress*, R.C. Roach, P.H. Hackett, and P.D. Wagner, Editors. 2016, Springer US: Boston, MA. p. 131-144.
207. Yetkin, F.Z. and D. Mendelsohn, *Hypoxia imaging in brain tumors.* Neuroimaging Clin N Am, 2002. **12**(4): p. 537-52.
208. Bergers, G. and S. Song, *The role of pericytes in blood-vessel formation and maintenance.* Neuro-Oncology, 2005. **7**(4): p. 452-464.
209. Hallac, R.R., et al., *A role for dynamic contrast-enhanced magnetic resonance imaging in predicting tumour radiation response.* British Journal Of Cancer, 2016. **114**: p. 1206.